Schweizerische Eidgenossenschaft
Confédération suisse
Confederazione Svizzera
Confederaziun svizra

Eidgenössisches Departement für
Umwelt, Verkehr, Energie und Kommunikation UVEK

Bundesamt für Energie BFE

Final report 30.09.2017

Untersuchung von Diesel- und "Dual-Fuel"-Verbrennungsprozessen unter motorrelevanten Bedingungen durch Implementierung von laserbasierten optischen Messtechniken

Investigation of Diesel and “Dual-Fuel” combustion processes at engine relevant conditions by means of the implementation of laser-based optical measurement techniques

PAUL SCHERRER INSTITUT

Date: 30. September 2017
Town: Bern

Publisher:
Swiss Federal Office of Energy SFOE
Forschungsprogram Verbrennungsbasierte Energiesysteme
CH-3003 Bern
www.bfe.admin.ch

Co-financed by:
Kompetenzzentrum für Energie und Mobilität CCEM, Paul Scherrer Institut, 5232 Villigen PSI

Agent:
Paul Scherrer Institut
Thermal processes and combustion laboratory
High temperature processes group
OVGA/105A
5232 Villigen PSI

Author:
Ales Srna, Paul Scherrer Institut, ales.srna@psi.ch
Dr. Rolf Bombach, Paul Scherrer Institut, rolf.bombach@psi.ch
Prof. Dr. Kai Herrmann, ITFE FHNW, kai.herrmann@fhnw.ch

SFOE head of domain: Carina Alles, carina.alles@bfe.admin.ch
SFOE programme manager: Stephan Renz, renz.btr@swissonline.ch
SFOE contract number: SI/501123-01 / 8100075

The author of this report bears the entire responsibility for the content and for the conclusions drawn therefrom.

Zusammenfassung

Der Diesel-Gas-Motor bietet eine attraktive Lösung zur Erfüllung künftiger Abgasvorschriften. Er kann mit einer Vielzahl von Zweistoffgemischen betrieben werden, wobei weitere Steigerungen im Wirkungsgrad zu erwarten sind. Allerdings ist ein besseres Verständnis der innermotorischen Verbrennungsvorgänge nötig, um die gewünschten Ziele zu erreichen. In diesem Projekt wurden dazu fortschrittliche Lasermessmethoden zur zweidimensionalen Erfassung verbrennungsrelevanter Parameter eingesetzt. Die Methoden umfassen verschiedene Hochgeschwindigkeits-Schnittbildtechniken (10 kHz) wie Zweifarben-Tracer-PLIF (planare laserinduzierte Fluoreszenz) zur Erfassung der Pilotbrennstoffverteilung, Formaldehyd (CH_2O)-PLIF zur Detektion der Produkte der kalten Verbrennung und OH-Radikal-PLIF zu Detektion der Flamme. Dazu kommen laserinduzierte Inkandeszenz (LII) und 2D-Absorptionsmessung (DBI) zur Russdetektion zur Anwendung. Weiterführende Verbesserungen der Methodik unter Einbezug passiver Hochgeschwindigkeits-Kinematographie erlaubten, unter Verwendung hochrepetitiver Laser, die Diesel-Gas-Verbrennung an einem Einhubtriebwerk zu erforschen. Mit den Messungen wurde ein umfangreicher Parameterraum mit Variation der Temperatur, der Methankonzentration sowie Druck und Dauer des Zündstrahls erfasst. Ein chemischer Einfluss des Methans konnte entdeckt werden: Methan inhibiert die Reaktivität der kalten Verbrennung in pilotbrennstoffarmen Mischungen und versursacht dadurch eine insgesamt verspätete Zündung. Dies führt einerseits zu einer Pilotbrennstoffverdünnung und möglicherweise damit zu Fehlzündungen, andererseits nimmt die Russtendenz ab. Im Gegensatz dazu sind bei längeren Eindüsungen wegen der resultierenden geringeren Sauerstoffverfügbarkeit mit Methan grössere Russkonzentrationen festgestellt worden. Aus den Messdaten wurden die für die Verbrennung relevanten Parameter bestimmt; die Resultate stehen nun in Form einer Datenbank für Validierung von CFD-Simulationen zur Verfügung.

Summary

The advancement of dual-fuel engines is an attractive solution for both the compliance with future emissions standards with optimized efficiency and for increasing fuel flexibility. A better understanding of the fundamental in-cylinder phenomena at engine relevant conditions is needed to achieve these goals. In the present project, in the first step, advanced laser-based optical techniques for 2-dimensional cross-cut detection of combustion relevant parameters were developed. The methodology portfolio includes high speed (10 kHz) two-color TMPD tracer-PLIF (planar laser induced fluorescence) for the detection of pilot-fuel concentration, CH_2O-PLIF and OH-PLIF for the detection of first and second stage ignition as well as laser induced incandescence (LII) for the soot detection. Measures to improve the signal and combine the methods with passive high-speed diagnostics were undertaken, to enable application of the methodology in a rapid compression machine to study dual-fuel combustion. A wide experimental matrix of dual-fuel engine-like conditions was tested including variations of the charge temperature, oxygen content and methane equivalence ratio, pilot fuel injection pressure and duration. It was proven that methane delays the pilot-fuel ignition trough a chemical interaction by inhibiting the first stage ignition in pilot-fuel lean regions. This observation explains the engine misfire of too short pilot injections. Related to this influence of methane, a complex interplay of combustion sooting propensity with methane has been revealed: For short pilot injections, lower soot quantity has been observed in dual-fuel cases due to the prolonged ignition delay and related spray lean-out. Contrary, for long injections methane inhibits soot oxidation and leads to an increased soot quantity. The experimental data has been processed to extract the relevant metrics of the dual-fuel combustion and assembled into a database for purposes of validation of CFD-simulations.

Astratto

La crescita nell'interesse nei motori dual-fuel è una soluzione attraente per entrambe le problematiche delle emissioni e la fuel-flexibility. Per perseguire questi obiettivi si necessita di una più approfondita comprensione dei fenomeni interni al cilindro a condizioni operative reali. In questo progetto, nella prima fase si sono sviluppate tecniche di diagnostica laser avanzate per sezioni bidimensionali di parametri di combustione. Le metodologie disponibili includono: due colori TMPD tracer-PLIF ad alta velocità (10kHz) per la diagnostica della concentrazione del carburante pilota, CH_2O-PLIF e OH-PLIF per la diagnostica dell'accensione del primo e secondo stadio e del Laser Induced Incandescence (LII) per la diagnostica del particolato. In una macchina a compressione rapida, per studiare il dual-fuel, sono state applicate metodologie per migliorare il segnale e accoppiare le metodologie con diagnostica a bassa frequenza. Una vasta gamma di condizioni sperimentali sono state investigate, includendo variazioni di contenuto di ossigeno e rapporto di equivalenza del metano, pressione del pilota e durata. É stato provato che il metano ritarda l'accensione del combustibile pilota inibendo l'accensione nelle zone magre del primo stadio. Questa affermazione spiega il misfiring delle iniezioni del pilota troppo brevi. Una complessa interazione della produzione di particolato con il metano è stata notata. Per iniezioni brevi del pilota una quantità di particolato minore è stata osservata in dual-fuel dovuta al prolungato ritardo di accensione e relativa diluizione dello spray. Al contrario, per iniezioni lunghe, il metano inibisce l'ossidazione del particolato da cui deriva una quantità maggiore di quest'ultimo. I dati raccolti sono stati processati per estrarre la metrica rilevante al dual-fuel combustore assemblarla in un database con l'obbiettivo di validazione di simulazioni CFD.

Contents

Zusammenfassung 3
Summary 3
Contents 5
List of abbreviations 6
1. Executive summary 7
1.1. Project goals 7
1.2. Project accomplishments 7
2. Characterization of mixture formation 9
2.1. TMPD Tracer spectral characterization 9
2.2. Two-color TMPD-PLIF fuel thermometry 10
2.3. Tracer characterization in the RCEM 15
3. Investigation of ignition and flame propagation 16
3.1. Low-temperature ignition detection via CH_2O-PLIF 17
3.2. High-temperature flame detection via OH PLIF 20
4. Detection of soot production 25
4.1. Soot-detection via LII 25
4.2. Soot detection via DBI and 1D-spectroscopy 28
5. Application in a rapid compression-expansion machine (RCEM) for dual fuel combustion 29
5.1. Adaptation of the RCEM cylinder head geometry and determination of the boundary conditions 29
5.2. Realized measurement campaigns 33
5.3. Pilot-fuel mixing characterization 35
5.4. Sensitivity of ignition delay on CH_4 concentration 38
5.5. Transition from ignition to premixed flame propagation 43
5.6. Soot detection 47
5.7. Dual-fuel flame luminosity 56
6. Generation of reference data for CFD validation 61
7. Publications and information dissemination 62
8. National and international collaboration 63
9. Conclusions and outlook 64
References: 64

List of abbreviations

BDC	Bottom Dead Center
CFD	Computational Fluid Dynamics
CH_2O	Formaldehyde
CMC	Conditional Moment Closure (combustion modeling)
CWL	Center Wavelength
DBI	Diffuse Back-Illumination
EOI	End of injection
EGR	Exhaust-gas recirculation
eSOI	electronic start of injection
ET	Energizing Time of the injector
FPS	Frames per second
FRCM	Flexible Rapid Compression Machine
FWHM	Full-Width at Half-Maximum
HTDZ	High temperature-pressure cell
HRR	Heat-release rate
(I)CCD	(Intensified) charge-coupled device
K	Absorption coefficient
KL	Absorbance factor based on natural logarithm
LII	Laser Induced Incandescence
Nd:YAG	Neodymium-doped Yttrium-aluminum garnet
OH	Hydroxyl radical
OME	Oxymethylenether (or PODE, Polyoxymethylene dimethyl ethers)
PAH	Poly-aromatic hydrocarbons
PLIF	Planar Laser Induced Fluorescence
PLII	Planar Laser Induced Incandescence
PSR	Perfectly stirred reactor
RCEM	Rapid Compression-Expansion Machine
SOI	Start of injection
SDR	Scalar Dissipation Rate
TDC	Top Dead Center
TMPD	N,N,N′,N′-tetramethyl-p-phenylenediamine

1. Executive summary

1.1. Project goals

Large Diesel engines for ship propulsion and power generation are facing increasingly stringent emissions regulations. Improved Diesel and in particular Dual-Fuel (DF) engines are considered a highly attractive solution for the compliance with future emissions standards at uncompromised efficiency and for increasing fuel flexibility. Diesel combustion is very efficient but it inherently favors the formation of soot and especially nitric oxide. Mitigating the formation of these pollutants is a major task in improving Diesel engines. This requires a better understanding of the fundamental in-cylinder phenomena during fuel injection, ignition, and combustion. There is a strong need for high fidelity measurements and application of advanced diagnostics in order to understand the physics of the injection and spray development processes. The focus of this project is on the application and further development of advanced laser-based optical techniques at demanding engine-relevant high pressure and high temperature conditions for the investigation of fuel spray (liquid/vapor mixture fraction) and combustion (ignition delay/location, flame lift-off) characteristics as well as soot detection.

Following investigations shall be performed:

- Characterization of mixture fraction formation
- Investigation of ignition and flame propagation
- Detection of soot production
- Application in a rapid compression-expansion machine (RCEM) for dual fuel combustion
- Generation of reference data for CFD validation

1.2. Project accomplishments

The advancement of dual-fuel engines is an attractive solution for both the compliance with future emissions standards with optimized efficiency and for increasing fuel flexibility. A better understanding of the fundamental in-cylinder phenomena at engine relevant conditions is needed in order to achieve these goals. In the framework of present project, in the first step, advanced laser-based optical techniques for two-dimensional cross-cut measurements of combustion relevant parameters have been developed and applied to study Diesel combustion in the HTDZ. Based on these results measures to improve signal level and suppress the noise have been undertaken. This enabled application of the developed methodology, using the high-speed laser system, to study Dual-fuel combustion in the RCEM.

In 2014 and 2015 the focus of the scientific work was to apply and further develop advance laser-based techniques to study Diesel-surrogate fuel distribution in the spray, to detect the products of the ‘cool’-flame reactivity and high-temperature combustion as well as to characterize the sooting behavior of the combustion. First, an advanced methodology for quantitative two-dimensional detection of fuel vapor concentration in a Diesel spray has been developed. The methodology is based on the two-color Planar Laser Induced Fluorescence (PLIF) of the TMPD tracer substance. Tracer has been rigorously characterized under engine relevant temperatures and pressures in the RCEM. A proof-of-concept of the methodology has been performed by application of the method to measure fuel concentration and temperature under engine relevant conditions in the HTDZ.

Proof of feasibility of OH PLIF and CH2O PLIF for detection of high temperature ignition and ‘cool’-flame reactivity, respectively, has been accomplished at the HTDZ. The aim of the investigations was to study the limits of applicability of both methods regarding the required laser energy and permissible pressure level. Additional feasibility study regarding the applicability of high speed PLIF imaging has been done. Environmental conditions up to 60 bar and 900 K have been probed and good image

quality could be obtained. Regarding the application of high-speed laser-based imaging under these conditions, also at low laser energies the LIF signal can be distinguished from the background luminosity. Based on the gained experience measures have been undertaken to improve the signal-to-noise ratio of the images. Strategies to combine the active laser-based diagnostics with passive Schlieren, Mie-scattering and OH* chemiluminescence have been devised.

In 2016 and 2017, the developed experimental methodology was applied to study Dual-fuel combustion in the RCEM of ETH Zürich. Five measurement campaigns could be realized with the measurement matrices involving a wide variation of charge temperature and oxygen content, pilot fuel variation and variation of pilot fuel injection duration and injection pressure. We were able to successfully apply high-speed TMPD tracer PLIF to study pilot spray fuel mixing and high-speed CH2O PLIF to study low temperature ignition stage and transition from the pilot ignition to premixed flame propagation. With additional measures undertaken to improve the signal level of the high-speed PLIF methodology the image quality was more than sufficient for the PLIF signal to be distinguished from the flame luminosity and to achieve good image quality. Overall, results of very high fidelity could be acquired. To gather further information, all PLIF acquisitions were combined with simultaneous Schlieren and OH chemiluminescence imaging methods.

The sooting behavior of the dual-fuel combustion has been investigated with passive DBI imaging combined with 1D spectroscopy of flame and soot luminosity. The optical thickness of soot and the soot temperature under different conditions has been determined. An additional study of the spectral footprint of the dual-fuel combustion has been performed to identify the species contributing to the flame luminosity of the dual-fuel combustion.

The investigations helped to improve the understanding of chemical interaction of methane with the ignition of the pilot fuel. Methane scavenging of the OH radical during the ‘cool’-flame ignition stage has been identified to be responsible for the increased ignition delay of pilot fuel in methane atmosphere. Furthermore the sooting behavior of the dual-fuel combustion has been characterized and different influences evaluated. A processing methodology has been developed to extract the relevant combustion metrics out of the raw image and trace data. The information of interest has been defined in cooperation with the CRFD group of LAV ETHZ. All acquired data has been processed accordingly and assembled into a database that will serve for purposes of validation of CRFD simulations and 0D-models of dual-fuel combustion.

2. Characterization of mixture formation

An advancedmethodology for quantitative determination of fuel vapor concentration in Diesel spray as well as detection of the liquid phase has been developed. The methodology is based on the PLIF of TMPD tracer mixed in small quantity into a non-fluorescing Diesel surrogate fuel. Standard application of the method with temperature correction via adiabatic mixing assumption has been developed and extended to a two-color tracer-PLIF thermometry method for direct measurement of fuel-vapor temperature. TMPD has been identified as the optimal tracer for application under Diesel- and dual-fuel relevant conditions based on an extensive literature study. Among state-of-the-art tracer substances for application of tracer PLIF for Diesel spray, TMPD has advantages of good co-evaporation with Diesel surrogate fuels, good fluorescent yield at elevated temperatures and it can be excited by the 3rd harmonic of a Nd:YAG laser. The disadvantages of the tracer are its slightly corrosive behavior on sealing materials and unpleasant smell. It is also rapidly oxidized in the presence of oxygen; therefore it is only appropriate for non-reactive conditions.

2.1. TMPD Tracer spectral characterization

A prerequisite for quantitative tracer-PLIF measurements of fuel vapor is a reliable characterization of the selected tracer substance (characterization of fluorescent yield and spectrum dependence on ambient temperature and pressure). Several authors attempted to characterize TMPD ([1-10]), however a comparison of the previous TMPD-characterization studies showed different results among different authors. For this reason a spectral characterization of the TMPD fluorescence spectrum and fluorescent yield has been performed under elevated temperatures in a specially developed flow cell setup (Figure 1).

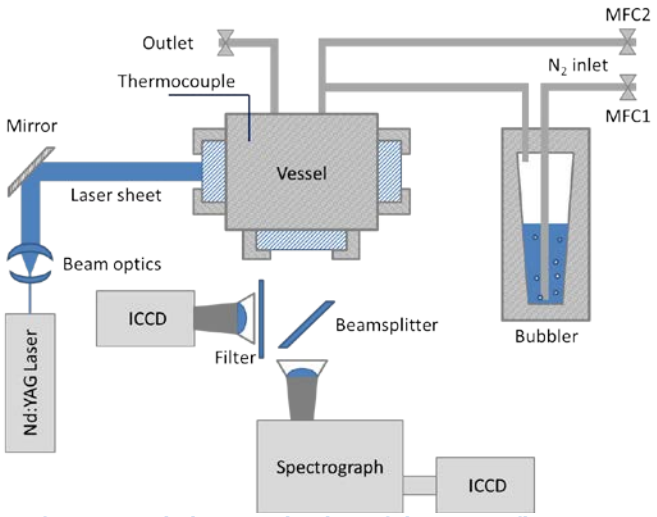

Figure 1: Flow cell setup for spectral characterization of the TMPD fluorescence spectrum and yield.

The setup consisted of an electrically heated (300 K – 800 K) flow cell with a volume of 0.6 dm^3 with a constant flow of pre-heated nitrogen containing a known concentration of TMPD. The tracer was primarily seeded into nitrogen in a heated bubbler device with a constant flow and afterwards diluted with pure nitrogen in order to keep volumetric tracer number concentration constant independent of the flow cell temperature. The dilution gas flow and flow thru the bubbler were precisely controlled with calibrated MFCs (mass flow controllers). The seeded tracer was excited with the 3rd harmonic of the radiation of a Nd:YAG laser attenuated down to 1 mJ energy per pulse. The fluorescent light was collected with an UV objective onto the spectrograph slit and its spectrum recorded using an ICCD camera. Correction for the fluctuation of laser power was applied by measuring the laser pulse energy of each pulse using a fast photodiode and a SRS boxcar integrator. A second ICCD equipped with UV objective and bandpass filter was used to record the laser pulse profile for each pulse.

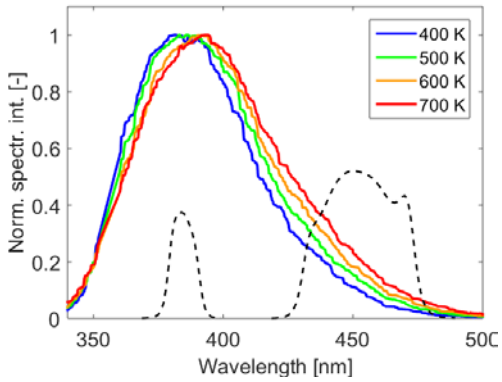

Figure 2: Temperature dependence of TMPD fluorescence spectrum. Black lines are the transmission curves of filters used for two-color TMPD LIF.

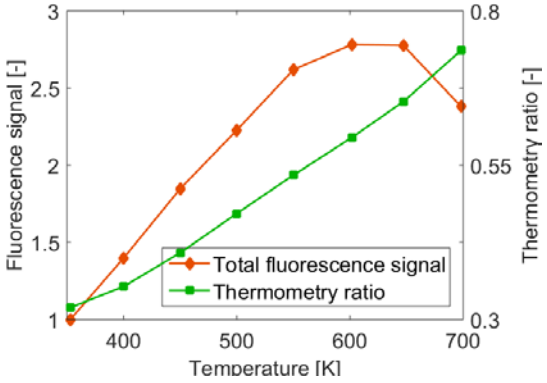

Figure 3: Temperature dependence of the total fluorescent yield of TMPD upon excitation with 355nm (red). Expected ratio of the fluorescece signal through filters for the two-color TMPD LIF thermometry (green).

The measured fluorescence spectrum of the TMPD is shown in Figure 2 and the total fluorescence signal in Figure 3. The attractiveness of TMPD as a tracer under engine relevant conditions is mostly because of its high fluorescent signal at elevated temperatures, increasing by a factor of 2.7 from 350 K to 600 K and remaining high up to 700 K and beyond (Figure 3). When using TMPD PLIF images to determine the fuel concentration, also the varying fluorescence yield has to be accounted for. This is challenging for applications in Diesel sprays, where the temperature of the fuel vapour is dependent on the local fuel concentration due to the evaporative cooling of the Diesel spray. The correction for the fluorescence yield dependence on temperature is usually performed iteratively using an adiabatic mixing assumption. Recently, a two-color tracer-PLIF thermometry approach for direct measurement of temperature using toluene as fluorescent tracer has been proposed [11-16]. Spectral characterization of TMPD revealed its potential for application of two-color approach to directly apply temperature correction due to a significant spectral shift of TMPD fluorescence spectrum with temperature. This potential has been further investigated by application of the two-color TMPD tracer-LIF methodology at the HDTZ facility (Section 2.2) and comparison of the results of single-color and two-color approaches.

2.2. Two-color TMPD-PLIF fuel thermometry

The developed methodology uses two-color detection of the TMPD-PLIF signal to measure fuel temperature based on the shift of the TMPD fluorescence spectrum with temperature (Figure 2). The two-dimensional temperature field is determined based on the ratio of the fluorescence signal through two spectrally separated bandpass filters (transmission curve plotted in Figure 2). Knowing the temperature field and therefore the fluorescence signal, it is possible to directly calculate the fuel concentration. The expected signal ratio for TMPD fluorescence changes from 0.35 at 350 K to 0.75 at 700 K (Figure 3) using the presently available filters, which is sufficient to determine the local fuel vapour temperature. This sensitivity is similar to the sensitivity of other tracers proposed for the two-color PLIF applications and could be further improved by selection of filters with larger spectral separation.

A proof-of-concept of two-color TMPD LIF thermometry has been accomplished by application of the method to measure fuel vapor temperature and concentration in a Diesel spray in the HTDZ facility. The experimental setup is shown in Figure 4. A frequency tripled Nd:YAG laser beam with a pulse energy of ca. 3 mJ (purposely low energy to be comparable to the output of high-speed lasers) was formed into a laser sheet with a width of 30 mm and subsequently mirrored into the HTDZ frontally onto the spray plume. The LIF signal was detected by two ICCD cameras, equipped with different bandpass filters. The image was split to both cameras using a 50% reflectivity beamsplitter mirror. A

third camera (CCD) imaged the Mie scattering of the laser sheet in order to detect the liquid phase of the spray.

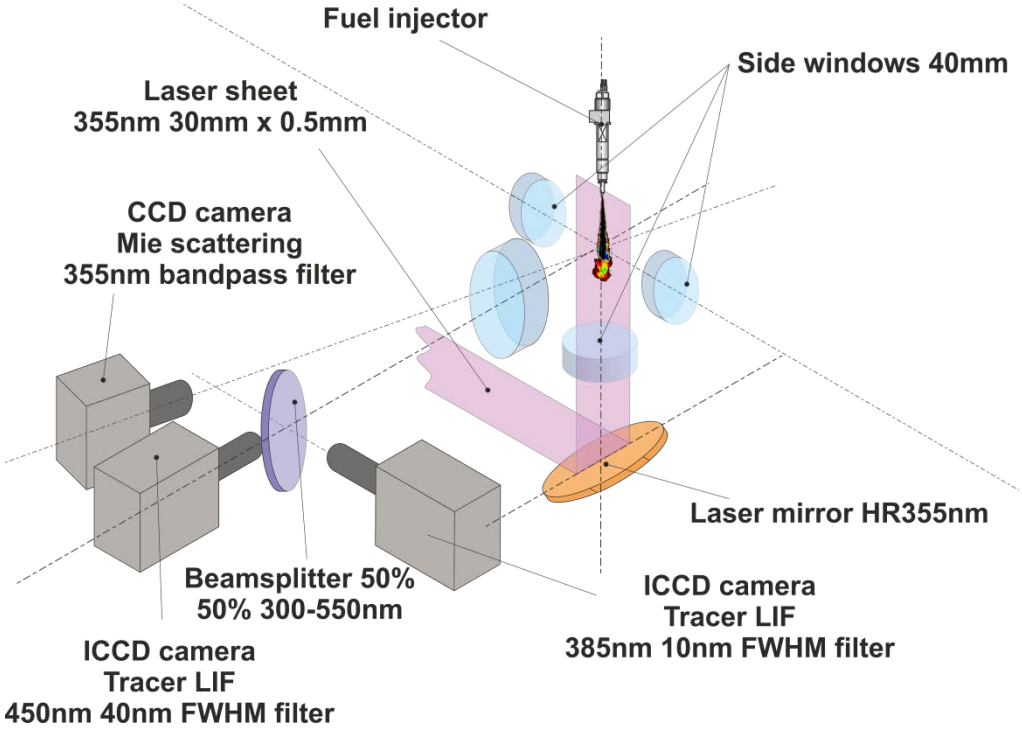

Figure 4: Two-color TMPD LIF setup as applied at the HDTZ facility.

A common difficulty when applying tracer LIF to Diesel sprays is a very strong fluorescence of the liquid fuel phase, where tracer density is up to 100 times higher than in the vaporized part of the spray. In case of longer fuel injections the liquid and vapor phase always co-exist limiting the useful dynamic range of the camera needed to distinguish the vapor phase intensity. For this reason a second dopant (1-MN, 10% addition) has been added to the dodecane doped with TMPD. Excited TMPD molecules form an excited complex with 1MN in the liquid phase. The fluorescence of this excited complex is spectrally shifted towards longer wavelengths, which effectively decreases the fluorescence intensity of the liquid phase, observed through the used filters, to a similar level as the intensity of the vapor phase fluorescence. Neither is the excited complex stable at higher temperatures nor is it formed in substantial amounts in the gas phase due the low number density. Therefore addition of 1MN does not influence the fluorescence of the TMPD in the vapor phase.

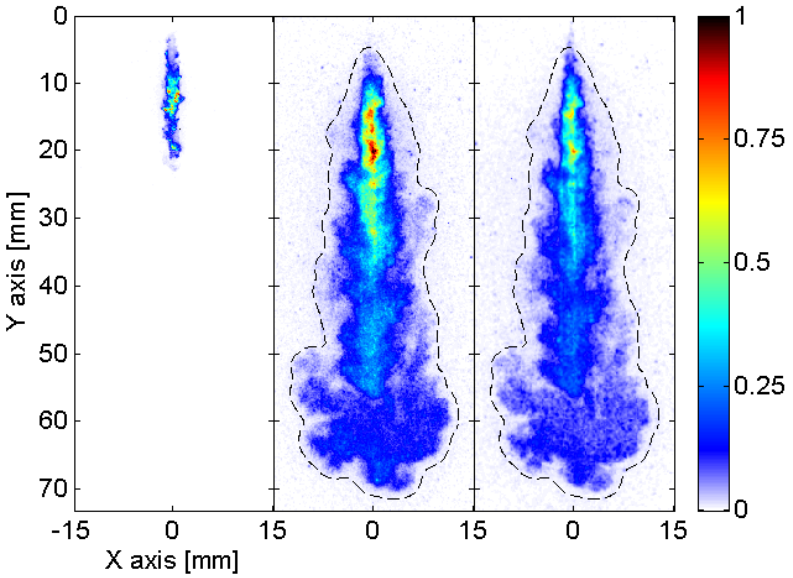

Figure 5: Single shot TMPD LIF images: Mie scattering (left, liquid phase), LIF at 385 nm (middle, filter 385 nm FWHM 10 nm) and LIF at 450nm (right, filter 450 nm FWHM 40 nm). Environmental conditions were 720 K and 50 bar. Fuel injection pressure was 1000 bar; the image was acquired 3 ms after eSOI.

Figure 5 shows an example of single shot images from all three cameras used for the two-color TMPD LIF. The Mie scattering image provides information about the regions with a presence of the liquid fuel. This gives information on the liquid length of the spray. The PLIF images show the typical distribution of vapor phase fuel concentration distributions of Diesel sprays l, with a fuel dense region close to the nozzle exit and a dilute region near the spray tip. Additional structures of the spray are discernible in the images. Image overlapping and spatial filtering routines have been developed in order to calculate the temperature field and to eliminate the ICCD camera photoelectron noise (Figure 6). First, both images are carefully scaled and shifted so that they overlap with subpixel accuracy, followed by spatial filtering using a Gaussian filter core. The ratio of both images is calculated and scaled into the fuel vapor temperature field based on a single point calibration and the TMPD characterization data (Figure 6, left). Finally, based on the LIF images and calculated temperature field, the fuel vapor concentration is determined (, right). The methodology does not allow to measure accurately the temperature in liquid phase due to the formation of an excited complex and consequent bias of the fluorescence ratio. The liquid regions can be removed from the images based on the information from simultaneously acquired Mie-scattering images.

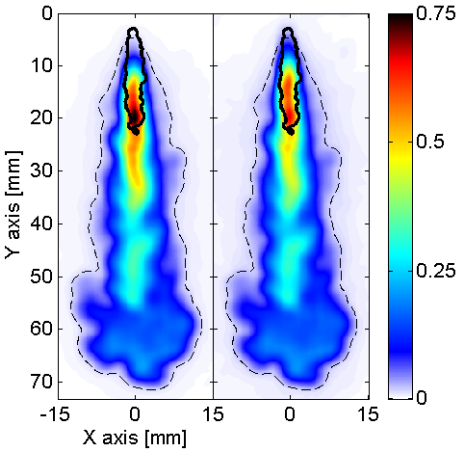

Figure 6: Spatially filtered LIF images through at 385 nm (left) and at 450 nm (right). A Gaussian filter with a core size of 20 pixel has been applied.

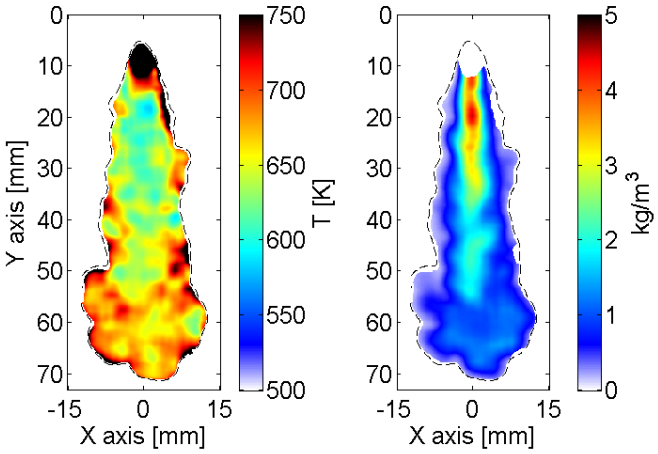

Figure 7: Single shot vapor temperature field calculated based on the two-color TMPD LIF image ratio (left). Single shot fuel vapor concentration (right).

A scrutiny of the precision of the two-color approach has been performed in order to estimate the amplitude of the random error and identify possible systematic errors due to the camera or fluorescence non-linearity. The used approach followed the procedure proposed by Tea et. al. [17]. Both ICCD cameras have been equipped with equivalent filters and a set of spray PLIF images has been acquired. Ideally, both images should be identical and the deviation from unity can be used to estimate the amplitude of error.

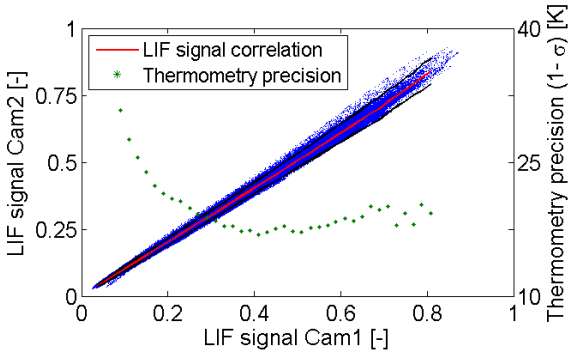

Figure 8: Correlation of the LIF signal intensity from both ICCD cameras (blue scatter plot, red mean value, black 1σ deviation) and the estimated precision of temperature measurement (green).

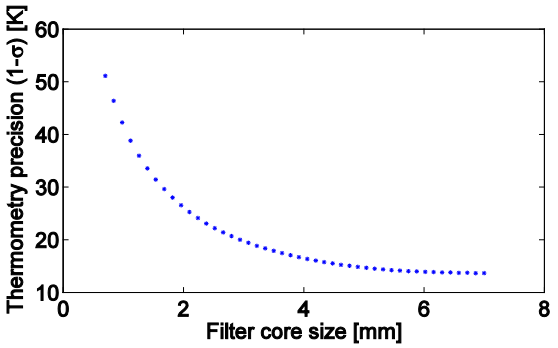

Figure 9: Dependency of the thermometry precision on the spatial filter core size.

Figure 8 shows the pixel-wise correlation of PLIF signal of both cameras (filtered images). It was found out that the precision of the thermometry strongly depends on the precise overlap of both images. Special computer routines were developed in order to achieve a sub-pixel precision of the overlap in order to improve the precision. Based on the 1σ deviation of the LIF signal correlation, precision of the thermometry was estimated to be at a level of 15-20 K in regions with LIF signal exceeding 30% of the camera dynamic range. In regions with lower LIF signal the precision diverges. This limits the usable dynamic range of LIF signal to approximately 1:10, where the precision of thermometry ranges from 15-40 K. At this temperature error the estimated precision of the measured TMPD vapor concentration is better than 10%. No systematic error due to the camera non-linearity or due to fluorescence saturation could be detected.

The origin of the error in precision is mostly due to the photoelectron noise of the ICCD camera, which can be reduced by means of spatial filtering at a drawback of reduced spatial resolution. The effect of spatial filter core size on the level of thermometry precision is shown in Figure 9. Using filter cores of larger size, the estimated precision improves, but at the expense of decreasing spatial resolution. The precision is on the other hand fairly poor for filters with a small filter core. For further investigations a pixel core size of 3 mm (corresponds to 20 pixels) was used as an optimum value.

Furthermore, a comparison of the single-color-detection approach assuming adiabatic mixing with the proposed two-color approach has been made. The single shot correlation of temperature over the whole spray (except the liquid phase) for a series of acquisitions is presented in Figure 11. Temperatures detected with both methods correlate well. However, the noise of the two-color approach increases to high values in the fuel-lean hot regions, thus strongly limiting the dynamic range of the two-color approach. This is also visible in Figure 12, which compares the average temperature field as predicted by both methods. Both methods predict similar temperature profile across the spray, whereas the two-color method shows high standard deviations in the fuel-lean regions. The reason is low signal intensity in the corresponding region (high attribution to noise) as well as lack of averaging (a spray is not always present in that region; a smaller number of repetitions contributes to the mean image). At the top of the image close to the nozzle the two-color approach detects biased temperatures due to formation of exciplex, as described in Section 2.2. Those regions have to be removed in the processing.

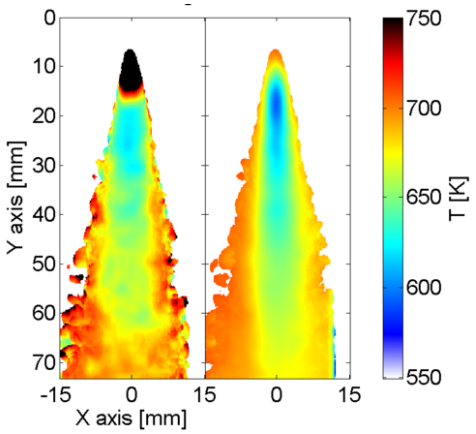

Figure 10: Comparison of averaged temperature field (10 shots) calculated using the two-color approach (left) and single-color adiabatic mixing assumption approach (right)

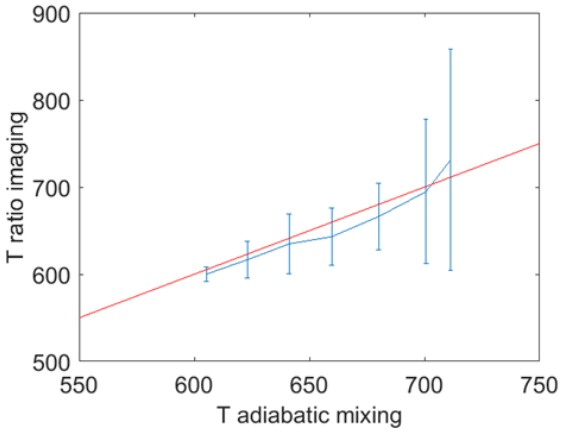

Figure 11: Two-color LIF temperature correlation to the adiabatic mixing temperature calculation for a fuel jet.

The precision of the methodology can be further improved by using filter sets with higher spectral separation and better transmission or by increase of the laser pulse energy. In case of Diesel fuel injection, the benefit of the methodology is moderate and required laser pulse energies are relatively high therefore making the extension to high-speed recording difficult. We believe the two-color methodology to have a high potential for measurements in environments with high thermal stratification (where the adiabatic mixing assumption does not apply) like optical engines or in case of fuel-water emulsions (large temperature range, adiabatic mixing does also not apply). Especially for small pilot-fuel injections like for dual-fuel applications the range of fuel temperature across the spray is small and the advantages of the methodology do not justify the increased experimental effort. Therefore, the single-color methodology has been further developed and applied at the RCEM as reported in Section 5.3.

2.3. Tracer characterization in the RCEM

The TMPD fluorescence characterization described in Section 2.1 has been performed under atmospheric pressure and was limited by the maximal temperature of the flow cell (800 K). In order to probe the TMPD fluorescence behaviour under the engine relevant range of pressures and to extend the limitation of the flow cell regarding the temperature an additional characterization campaign has been performed in the RCEM. A homogeneous mixture of TMPD in nitrogen has been created in the RCEM after inlet valve closure by injecting n-heptane doped with 2% of TMPD using a water-cooled Siemens VDO hollow-cone gasoline injector (i.e. the setup used in previous projects to study HCCI combustion).

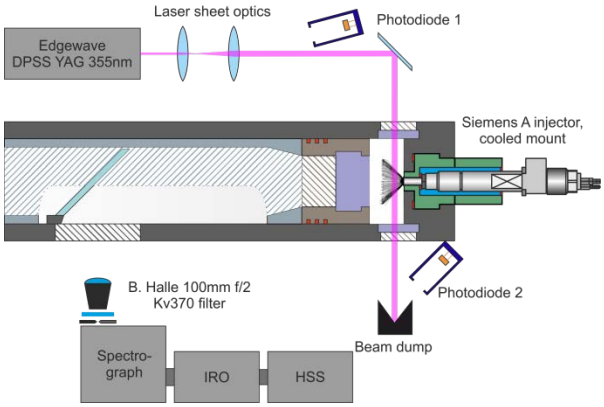

Figure 12: Optical setup applied for the TMPD fluorescence spectrum characterization at the RCEM

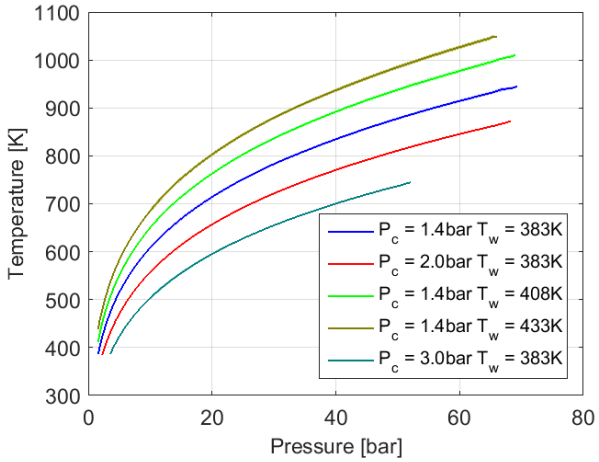

Figure 13: The pressure-temperature curves for a sweep in BDC conditions in the RCEM.

The optical setup (Figure 12) consisted of a high-speed Nd:YAG laser used for TMPD excitation (laser sheet dimensions 20 mm x 3 mm) and a high-speed intensified camera coupled to an imaging spectrograph. Fluorescence emission was collected and projected onto the spectrograph slit using an UV-objective equipped with a long-pass filter to supress the scattered laser light. Laser pulse intensity and the intensity of the transmitted laser light were measured with fast photodiodes coupled to the SRS gated integrators. High repetition rate of the laser (10 kHz) allowed acquiring a sufficient number of spectra over the ten compression stroke repetitions. In the next step each spectrum has been assigned into pressure and temperature bins in the cycle and correspondingly averaged over all repetitions. In the final stage the averaged spectra were corrected for the spectral sensitivity of the acquisition setup (intensifier quantum efficiency, spectrograph grating, mirrors in the optical path) based on the equipment manufacturer data and transmission spectra measured using a UV-VIS spectrophotometer.

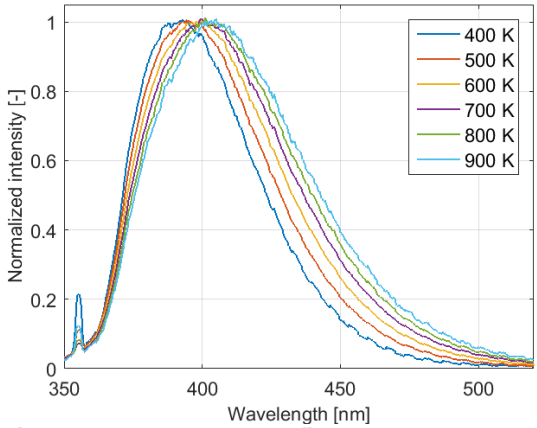

Figure 14 TMPD-LIF fluorescence spectra acquired using the high-speed laser in the RCEM.

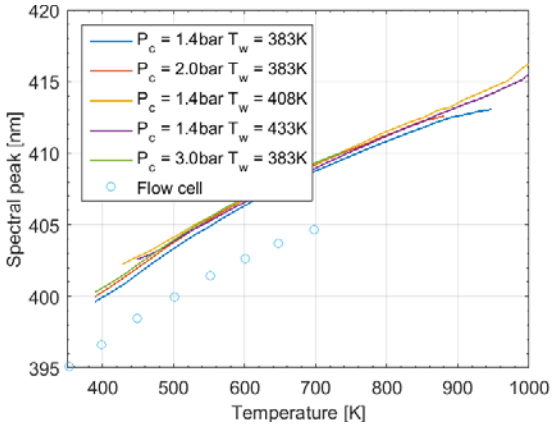

Figure 15: Shift of the center of weight of the emission spectrum with temperature for different operating points in the RCEM and in the flow cell.

Using the RCEM to provide engine-relevant conditions for the tracer characterization enabled us to extend the temperature range of the TMPD characterization to 900 K (Figure 14) and beyond. The sensitivity of the LIF spectra on temperature has been confirmed and the data was found to be of high fidelity. In Figure 15 the correlation of the centre-of-weight of the spectrum on temperature for a range of different BDC conditions has been plotted and compared to the spectra acquired in the flow cell. The investigations confirmed negligible sensitivity of the spectra on pressure (different BDC conditions results in difference of pressure at the same temperature in the compression cycle). This is important for applications of the methodology to engine relevant conditions where pressure might rapidly change during the same cycle. The comparison of the spectra acquired in the RCEM and flow cell show ca. 5 nm shifted centre-of-weight of the flow cell spectra and equal sensitivity to temperature. This can be explained by the different equipment used in different experiments and by the self-absorption of fluorescence by the tracer due to the relatively high seeding density used in the RCEM.

3. Investigation of ignition and flame propagation

Diesel fuel ignition under the engine relevant conditions is a two-stage process. In the first stage, the fuel breaks into smaller molecules in a slightly exothermic process resulting in an increase of temperature (100-200 K) and in high concentrations of intermediate products (CH_2O, H_2O_2, C_2H_4,…). Among those, CH_2O is the most appropriate marker for the onset of low-temperature chemistry since it is produced in significant amounts and can be directly excited in a simple excitation scheme with the 3rd harmonic of a Nd:YAG laser. A second stage of high-temperature combustion follows after the 'cool'-flame ignition, in which CH_2O and other intermediate species are consequently oxidized, therefore the disappearance of the CH_2O signal indicates ignition. During the high-temperature ignition intermediate radicals like CH, H, and OH are present for a short time. The OH radical is the selected tracer for the low-temperature chemistry, however, it is also abundantly present in the burnt high-temperature zone due to its thermal equilibrium with water. Detection possibilities for OH radicals include imaging of OH* chemiluminescence and active OH-PLIF techniques. OH* chemiluminescence is straightforward to image, however, the results have to be interpreted with caution since OH* is the source term of the OH radical and therefore does not reflect the actual OH concentration. OH-PLIF images indicate more closely the concentration of the OH radical, however, application requires a complex excitation scheme with use of a narrowband tunable dye lasers. While the deduction of OH concentration fields out of PLIF images in lean combustion environments is straightforward, the process needs more elaborateness in rich mixtures.

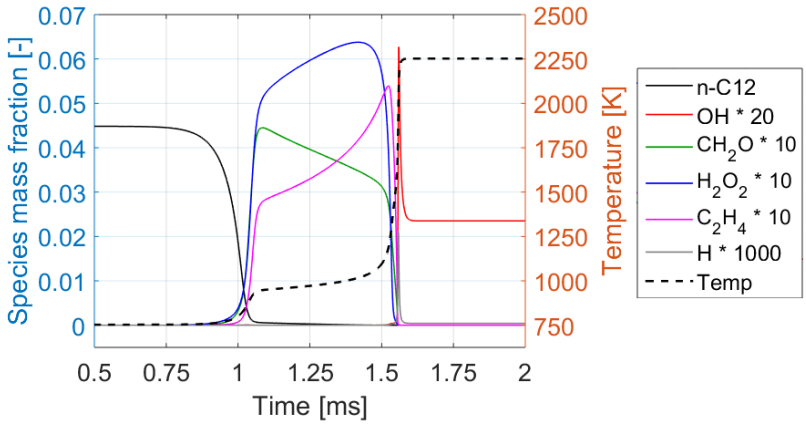

Figure 16: Evolution of temperature and selected species mass fractions during an auto-ignition combustion process calculated using a PSR simulation with a detailed chemical kinetics mechanism (LLNL). Conditions: 750 K 30 bar, $\lambda_{dodecane}$ = 1.5.

Especially for application to dual-fuel combustion, it is very important to be able to detect both the low-temperature combustion and the high-temperature ignition in order to assess the influence of methane radical scavenging on the different stages of auto-ignition.

With the aim to extend the methodology to high-speed applications at the RCEM facility, this study focussed on assessing the limitations of the image quality at low laser pulse energy and the limitations in regard to optical access and interference from other species (PAH and soot). Limitations imposed by the pressure and temperature through collisional quenching of the fluorescing species have been assessed as well. Based on the gained experience, improvements of the experimental setup have been made and the methodology has been extended to high-speed applications.

3.1. Low-temperature ignition detection via CH_2O-PLIF

The experimental setup for the detection of CH_2O-PLIF with simultaneous imaging of OH* and Mie-scattering of the liquid phase is sketched in Figure 17. CH_2O was excited using the 3rd harmonic of a Nd:YAG laser at 355 nm. This excitation scheme was preferred to an excitation with a dye laser since according to the literature it yields a higher signal [18]. The disadvantage of this approach is the relatively weak absorption and lack of possibility of on- and off-line imaging to distinguish the PAH interference from CH_2O signal [19]. A laser sheet with a width of 30 mm was directed frontally on the spray plume. The PLIF signal was detected around 450 nm using an ICCD camera. Simultaneously, OH* chemiluminescence was detected using a second ICCD to provide information about the spray zones that have undergone high temperature combustion already. Additionally, to detect possible interference from the liquid fuel fluorescence, regions with presence of liquid fuel were detected by a CDD detecting the Mie scattering of the droplets. A CCD camera detected the Mie scattering of fuel droplets to indicate regions with present liquid fuel.

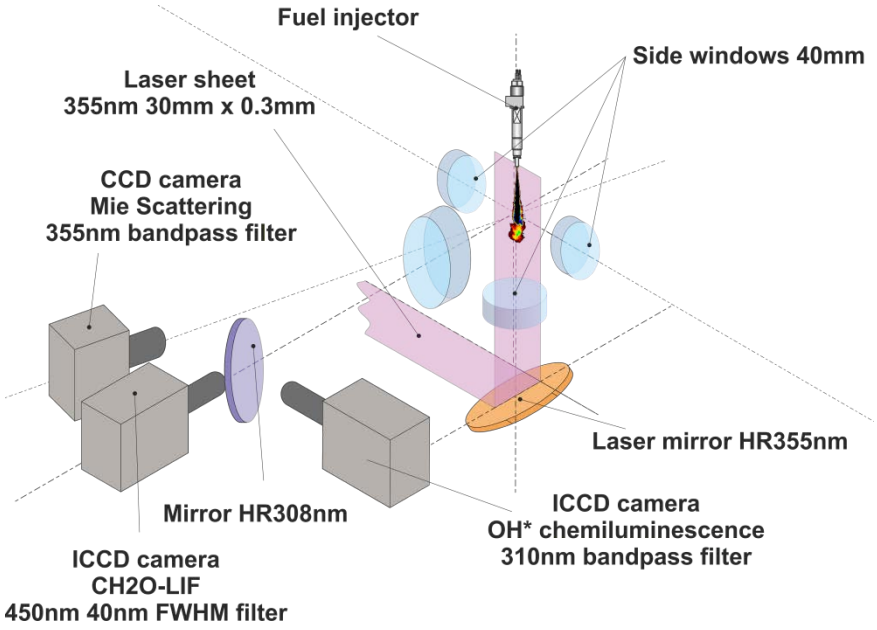

Figure 17: CH_2O LIF setup at the HTDZ.

Single shot CH_2O LIF images with the laser firing at times close to ignition are presented in Figure 18. At the temperature of 750 K the initial CH_2O LIF signal appears at laser timings around 0.4 ms before high temperature ignition. After the first occurrence, the CH_2O concentration builds up quickly until high temperature ignition, when CH_2O it is rapidly consumed. A small amount of CH_2O can be detected also in a fully developed flame above the liftoff, where the rich premixed combustion takes place. The OH* chemiluminescence signals correspond well with the regions where CH_2O signal disappears. Some overlap occurs due to the line-of-sight nature of OH* imaging. No CH_2O is detected in the liquid region. No significant interference from other species was observed at 750 K.
At higher temperatures (Figure 18 below), the first CH_2O signals occurred 0.3-0.4 ms before ignition, similarly as in the 750 K case. The extent of the CH_2O cloud is respectively limited due to the short ignition delay. After ignition, CH_2O is rapidly consumed and already 0.1-0.2 ms after ignition a strong different LIF signal is detected, which is generally attributed to polyaromatic hydrocarbons (PAH). PAH are the soot precursors and they absorb and emit in the same spectral range as CH_2O. This interference is always present in sooting Diesel sprays and can represent a difficulty due to an overexposure of the image intensifier. For dual-fuel investigations, where CH_2O is of largest interest, the amount of soot and PAH is moderate and therefore we do not expect difficulties with this interference. Additionally, CH_2O and PAH in Diesel and dual-fuel combustion usually appear spatially separated. In low sooting environment this can be of an advantage since the PLIF has a significantly lower detection limit than the common soot detection methods. This enables detection of very small amounts of soot.

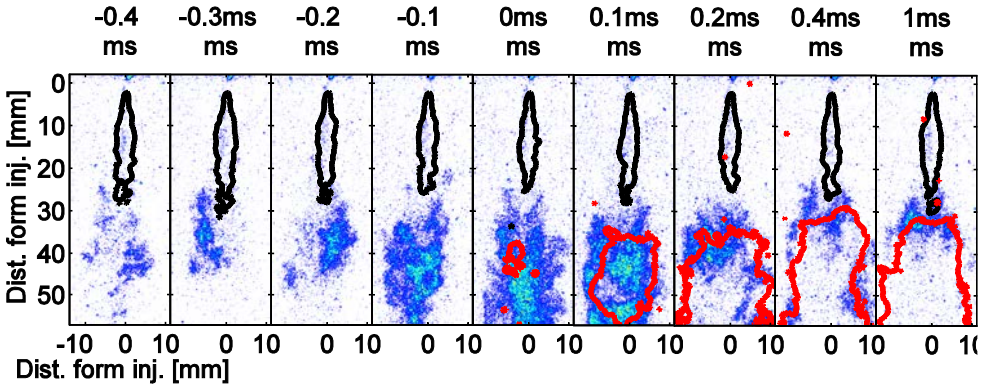

(a) T = 750 K, p = 35 bar

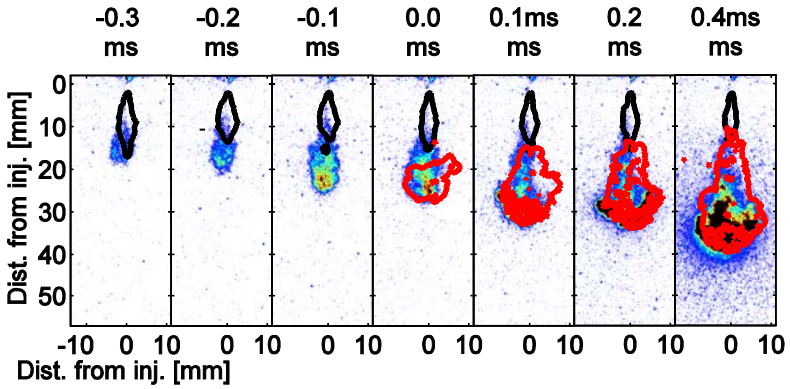

(b) T = 900 K, p = 35 bar

Figure 18: Sequences of single shoot CH_2O LIF images taken at various times around high temperature ignition time. Overlaid are the contour of the liquid spray (black, Mie scattering) and zones with high temperature combustion (red, OH* chemiluminescence). The upper series was taken at a temperature of 750 K, the lower series at 900 K.

All presented investigations were performed with a low laser pulse energy matching the pulse energy of the high speed laser system. This was done in order to study the feasibility of high-speed CH_2O LIF imaging. We investigated signal levels, which we can expect from the high-speed laser system. As seen in Figure 18, the expected image quality is sufficient to identify the most reactive regions and to image the distribution of CH_2O in the spray before ignition. The high speed laser system enables frame rates of up to 10 kFPS. Since CH_2O is an intermediate species in the auto-ignition process and only present for a short period of time, an additional analysis was performed to investigate whether 10 kFPS is a sufficient frame rate to temporally resolve the CH_2O formation. Figure 19 presents the total CH_2O LIF and total OH* chemiluminescence signal at different times around ignition. The time span from the first CH_2O LIF signal until steady state is approximately 0.6 ms at 750 K. At 900 K the apparent CH_2O signal starts rising rapidly 0.2 ms after ignition due to appearance of PAH. In both cases several images can be acquired from the first CH_2O appearance until its consumption. This corroborates feasibility performing time resolved CH_2O imaging using the high speed laser system at 10 kFPS.

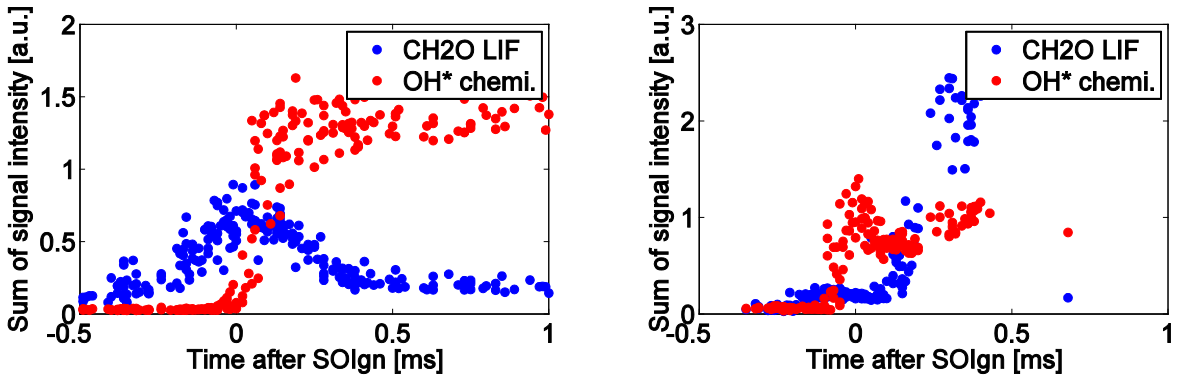

(a) T=750 K, p=35 bar (b) T=900 K, p=35 bar

Figure 19: Total CH_2O LIF and OH signal intensity at different times around high-temperature ignition at 750 K (left) and 900 K (right) environment temperature.

Overall, the image quality in the original setup was sufficient for high-speed applications but not excellent. Further improvements towards improvement of the imaging setup have been undertaken with selection and purchase of an improved image filter. Based on a literature study a filter with 80 nm FWHM and a central wavelength of 440 nm has been identified as optimal to yield highest signal and best CH_2O/PAH signal ratio. Overall, an improvement of the signal level of 400% - 500% over the conventional filter has been achieved.

3.2. High-temperature flame detection via OH PLIF

The state of the art detection of the high temperature combustion is commonly done by the OH* chemiluminescence imaging. The method is simple to apply, even in a time resolved manner, but it only provides line of sight information. Additionally, OH* chemiluminescence signal is not proportional to the actual OH concentration since the signal originates from the chemically produced OH* species. Laser induced fluorescence of the OH radical itself (OH LIF) provides two-dimensional cut information and can be potentially scaled to yield the actual OH concentration. In order to excite OH a tunable dye laser is necessary due to the narrow absorption lines of the OH radical. Application of the method under engine relevant conditions is also challenging due to the collisional quenching of the excited OH. Additionally, the concentration of OH in fuel rich zones is very low under the high pressure conditions.

OH LIF has been applied to detect the OH radical distribution in the Diesel flame in the HTDZ. A state of the art Nd:YAG laser coupled to a tunable narrow band dye laser has been used, which yielded pulse energy of up to 24 mJ in the wavelength range of 282-285 nm. A laser sheet with a height of 30 mm was formed by a combination of three cylindrical lenses and was subsequently mirrored onto the flame through a side window of the HTDZ. A plane in the region from 22 mm – 52 mm from the injector nozzle was illuminated by the laser sheet. The LIF signal was recorded using an ICCD camera. Simultaneously, OH* chemiluminescence was recorded using the double-frame functionality of the employed ICCD in order to image the whole burning extent of the flame.

First, the OH excitation line which yields the highest signal was identified. The tested excitation lines were selected based on the input from the literature and the LIFBASE LIF simulation software [20]. Finally, the line A-X(1,0) Q1(6) has been selected since it yielded the highest signal level while preserving a low temperature dependence when tested in the HTDZ.

Single shot OH LIF images were obtained at three different environment temperatures (750 K, 800 K, 860 K) for a Diesel fuel injection and for a small pilot injection. Figure 20 shows the ignition sequence (single shot images at various times after ignition) of a Diesel spray at a temperature of 750 K and

50 bar environment pressure. Using full laser energy, high quality images could be obtained also at the high pressure of 50 bar. After the ignition, premixed combustion occurs very fast and 0.2 ms after ignition the first indication of the diffusion flame with a low OH concentration in the fuel-rich center of the spray plume can be seen. The diffusion flame then slowly stabilizes and the flame front reaches its final shape.

Comparison of the OH LIF and OH* chemiluminescence images shows a significant difference of the signal distribution. This is partially due to the line-of-sight nature of the OH* chemiluminescence images. Another reason is that the chemiluminescence signal originates from the chemically produced OH*, which does not necessarily correspond to the actual OH concentration but rather to its production rate. For this reason a very strong chemiluminescence signal is detected at the flame liftoff, where the actual OH concentration is very low due to the fuel rich conditions. This demonstrates the advantage of OH LIF over the chemiluminescence imaging.

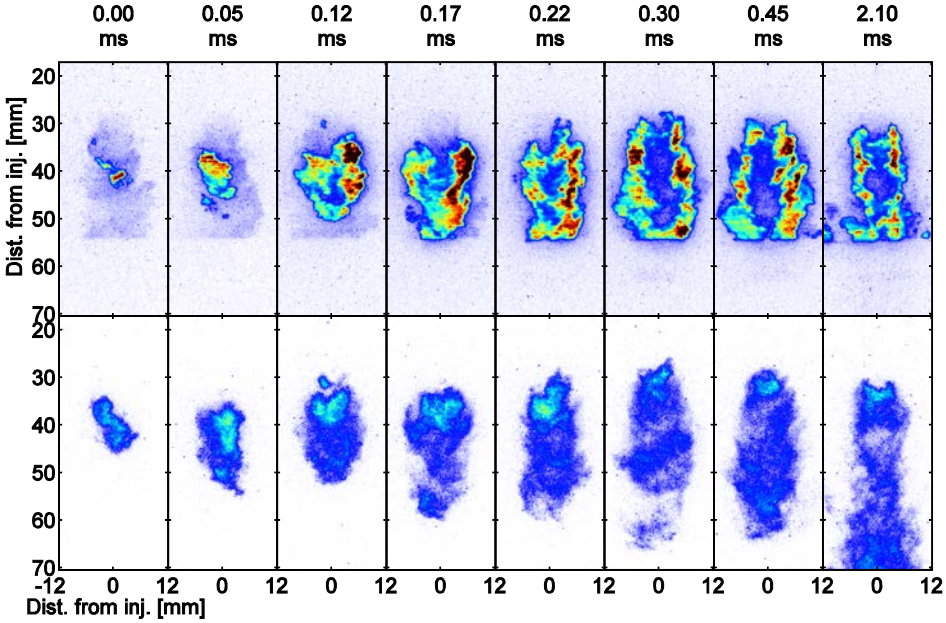

Figure 20: Series of single shot OH LIF (above) and simultaneously acquired OH* chemiluminescence (below) images at different times after high temperature ignition at conditions of 750 K and 50 bar.

Figure 21 shows a series of single shot OH LIF and chemiluminescence images at a temperature of 860 K and 50 bar pressure. At this temperature, the Diesel flame is already moderately sooting. After ignition, the premixed flame spreads rapidly and the first soot cloud can be detected already 0.23 ms after ignition. As the soot cloud becomes thicker, laser light is absorbed in the cloud and only the OH signal on one side of the soot cloud is visible. Additionally, also PAH can be excited by the laser sheet, therefore it is not possible to tell whether all signals originate from OH.

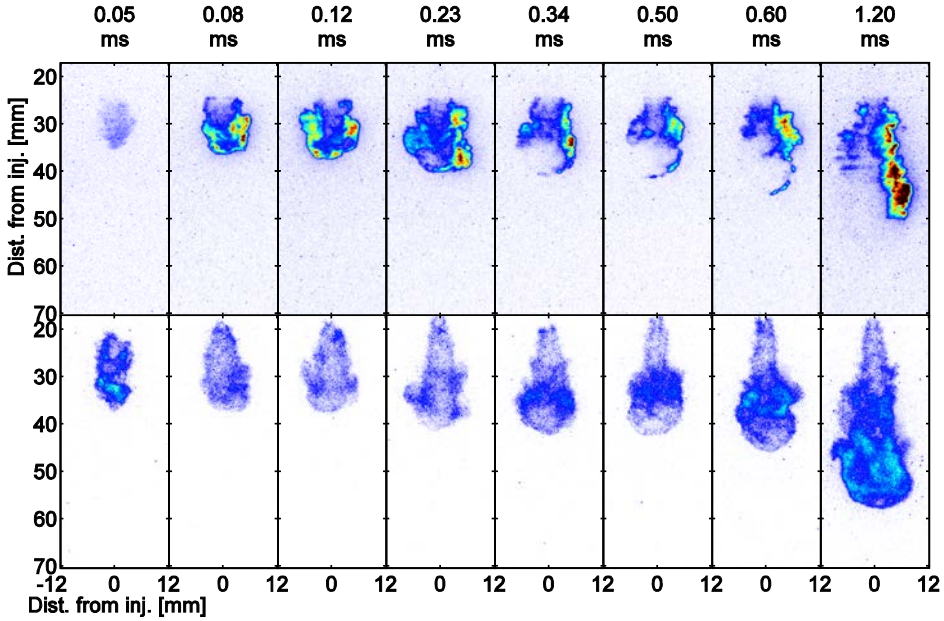

Figure 21: Series of single shot OH LIF (above) and simultaneously acquired OH* chemiluminescence (below) images acquired at different times after high temperature ignition at conditions of 860 K and 50 bar.

To investigate the interference from PAH in the OH LIF images, a series of experiments has been performed, where the dye laser has been tuned to an off-resonance wavelength in order not to excite OH radicals. PAH, which are expected to contribute most of the interference have a broadband absorption spectra, are therefore still excited. By comparison of the averaged images with OH on-resonance and off-resonance excitation (Figure 22) it is possible to estimate what part of the signal originates from the OH fluorescence.

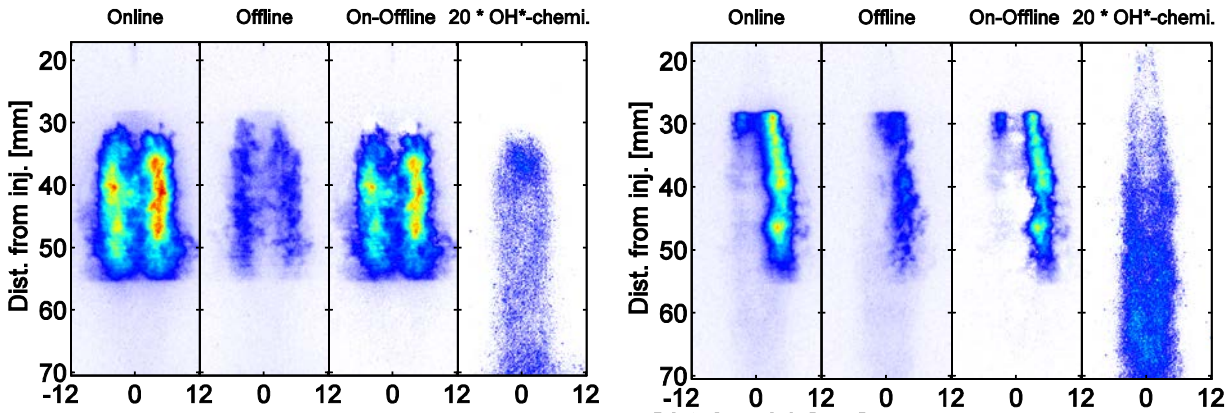

(a) T=750 K p=50 bar (b) T=860 K p=50 bar

Figure 22: Average OH on-resonance (1st columns) and off-resonance (2nd columns) LIF images. The images in the 3rd column are on-resonance images with subtracted off-resonance signal. The 4th columns show OH chemiluminescence images with the intensity multiplied by 20. The left series was recorded at 750 K, the right series at 860 K air temperature.

At 750 K under non sooting conditions, the off-resonance image is significantly weaker than the on-resonance image. Since conditions are non-sooting, no PAH are formed. The signal off the off-resonance image might actually also originate from the OH radical due to the collisional broadening of OH lines under elevated pressures. Therefore no flame structural difference between the on-

resonance images and on-resonance images with subtracted off-resonance signal can be observed. The situation is different at 860K, where significant interference from PAH can be expected. The off-resonance signal level is approximately at one third of the level off the on-resonance image. Online images with subtracted off-resonance signal show that in the center of the flame no signals originate from OH. Additionally, due to the constrained optical access of the HTDZ, under high temperature conditions the flame structure around the liftoff cannot be assessed by OH LIF since that area cannot be illuminated by the laser sheet.

In order to assess the feasibility of high-speed OH LIF imaging, the pulse energy of the dye laser was decreased to 1.5 mJ, which corresponds to the pulse energy of the high-speed dye laser at 283 nm. Figure 23 compares the image quality of OH LIF at full laser pulse energy and with the decreased energy by comparing five single shot images. The camera gain was increased for images with decreased laser pulse energy in order to achieve best possible image representation. Overall, the image quality at decreased laser pulse energy is noticeably worse than when full laser energy was used, but the structures of the flame front can still be distinguished. This means the high-speed OH LIF recording of the flame front is feasible, but at reduced image quality.

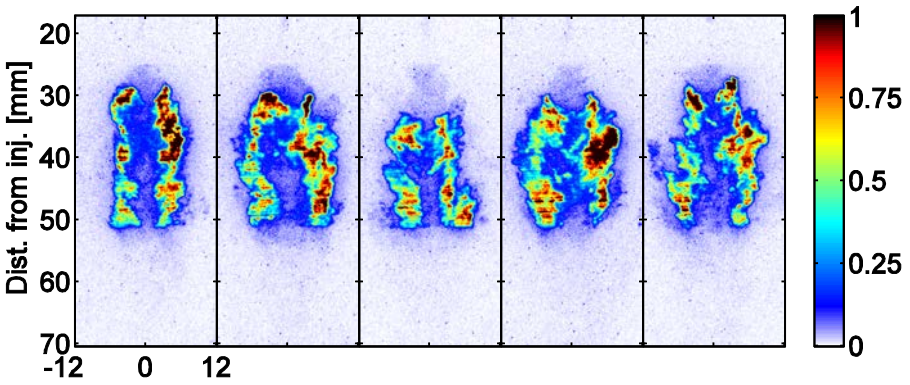

(a) Full laser pulse energy (24 mJ)

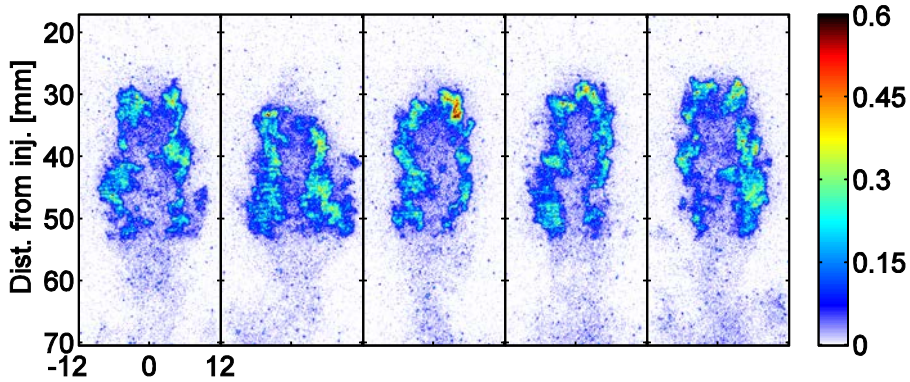

(b) Decreased laser pulse energy (1.5mJ)

Figure 23: Comparison of five randomly selected single shot OH LIF images (conditions 750 K 50 bar) at full laser pulse energy (above) and at decreased laser energy (below).

Further development of the methodology has been realized (design and ordering of advanced UV filters, advancement in timing and triggering systems, commissioning and testing of the high-speed dye laser) in order to further improve the signal ratio, resulting in successful application of the high-speed OH PLIF methodology to study Diesel combustion at the HTDZ test rig. Figure 24 shows an example of a high-speed OH-PLIF recording of Diesel combustion with subtracted background OH* chemiluminescence signal. Following ignition, it is possible to trace both the outer and inner OH PLIF

contour. The outer contour determines the flame extent while the inner contour enables to trace the stoichiometric mixture fraction (OH concentration is very low in fuel-rich regions). Approximately 0.5 ms after ignition, the inner contour collapses since mixing proceeds and the fuel-rich region ceases to exist. After this occurs, the OH PLIF contour marks hot burnt regions. Overall, an acceptable signal quality has been achieved to distinguish the flame regions from the background and to extract the flame characteristics from the images. The developed methodology will be applied at the RCEM to study dual-fuel combustion.

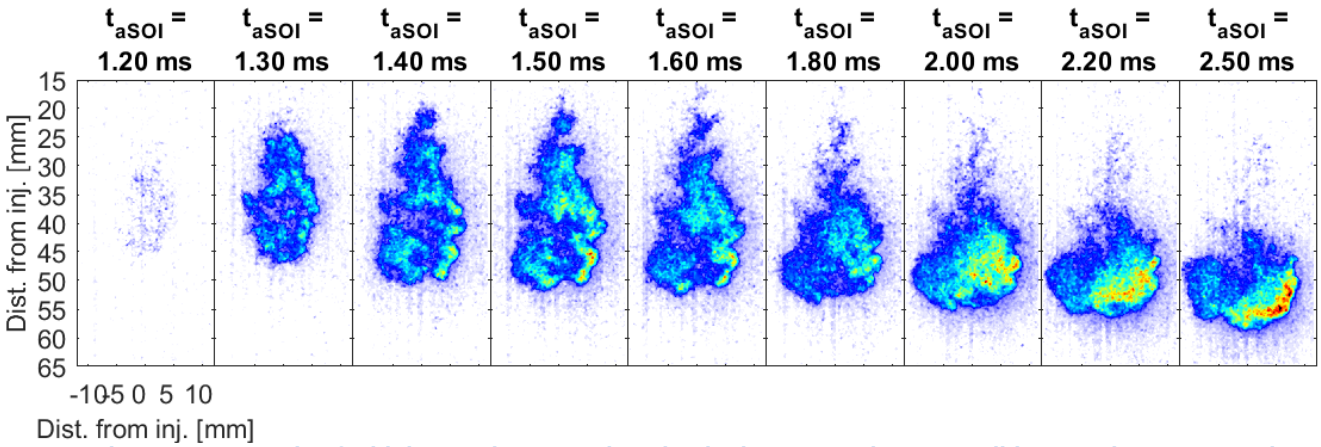

Figure 24: Example of a high-speed OH PLIF imaging in the HTDZ. Charge conditions: 40 bar 850K. Fuel injection: 600 bar 0.5ms energizing time.

4. Detection of soot production

The state of the art methodologies for quantitative 2D in-cylinder measurements of soot concentration includes Laser Induced Incandescence (LII), two-color pyrometry and diffuse back-illumination absorption technique (DBI). Among them, LII is the only technique working with the laser-cut principle being therefore able to provide information on soot distribution within the soot cloud. two-color pyrometry and DBI are line-of-sight techniques. The quantification potential of two-color pyrometry is limited since the outer layers of the soot cloud shade the inner regions and therefore over-proportionally influence the detected soot temperature. This might lead to false quantification in soot clouds with large gradients of soot temperature. The DBI technique allows very straightforward and unambiguous quantification and has therefore been adopted as the standard soot detection technique of the ECN workshop community. In the present work, the LII and DBI techniques were considered for application to the dual-fuel combustion research.

4.1. Soot-detection via LII

The LII technique is very attractive for being the only method available to provide sectional images containing high-fidelity information on soot inside of the soot cloud. The principle of LII is based on the heating of soot particles up to the carbon sublimation temperature by a high energetic laser pulse. The heated soot emits bright black body radiation which is acquired by an ICCD camera using very short gating. The difficulty of applying LII at engine relevant pressure is mostly due to a very fast cooling of the particles, resulting in a relatively low signal and therewith with a low signal to background ratio. The LII signal is proportional to the soot absorption KL value if the laser fluence is above a certain threshold which is wavelength specific [21]. If this condition is fulfilled, a single point calibration at a known soot concentration is sufficient to determine the complete two-dimensional soot distribution. Furthermore, LII signal absorption in soot clouds between the laser sheet and the camera has to be accounted for.

LII has been applied to measure soot concentration in the HTDZ facility (setup in Figure 25). A Nd:YAG laser at 1064 nm, providing pulse energies of around 180 mJ, has been used. A laser sheet with a height of 30 mm has been formed using two cylindrical lenses and focused to a thickness of 0.3 mm using an additional spherical lens. Two configurations have been tested; a configuration with the laser sheet impinging frontally on the spray and a configuration with the laser sheet impacting sideways. The LII signal has been detected using an ICCD camera at wavelengths around 450 nm. Temporal separation between the laser pulse and the camera gate as well as the duration of the camera exposure has been varied in order to achieving optimal settings. Simultaneously, OH chemiluminescence has been acquired in order to provide additional information on the flame liftoff length in order to correlate this value to the amount of soot.

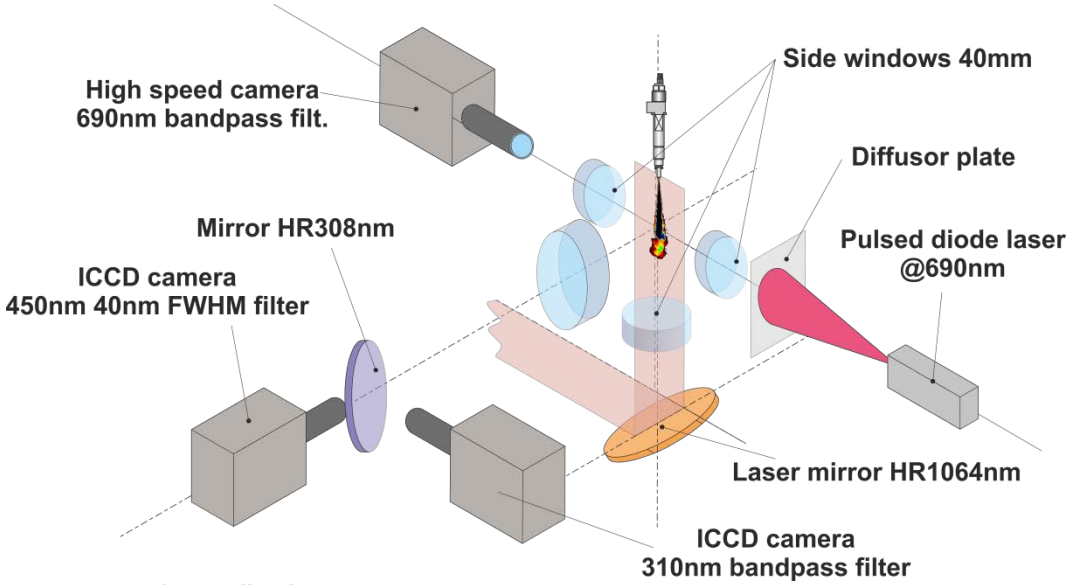

Figure 25: LII setup for application at HTDZ.

The LII method requires a single point calibration with a known soot concentration verified by light absorption or alternative methods. Initial tests measuring light attenuation using a He-Ne laser beam failed due to strong deflection of the laser beam by density gradients originating from high temperature gradients. Therefore the DBI technique was used as a light-attenuation technique based on diffuse illumination. The advantage of the DBI technique is that it is insensitive to beam-deflection due to density gradients. DBI provides two dimensional line of sight KL distributions of the soot cloud. This enables scaling the LII images into soot KL values, which are proportional to the soot concentration.

LII has been applied to a range of sooting conditions to estimate the limitations of the technique. Different sooting behavior of the Diesel spray has been achieved by a variation of environment pressure and temperature and by variation of the injection pressure. Soot KL values from 0 (non-sooting conditions) up to KL above 3 have been achieved. Figure 26 shows single shot images at moderate sooting conditions (above) and at heavily sooting conditions (below).

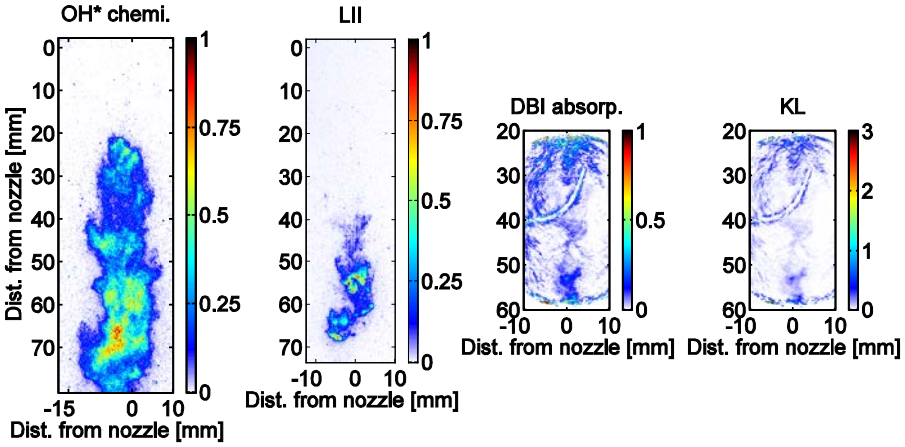

(a) Moderately sooting conditions: p=51 bar T=800 K

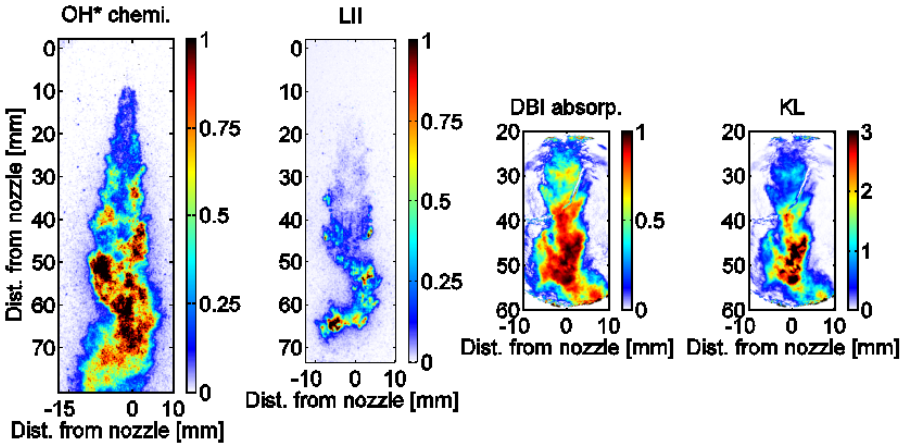

(b) Highly sooting conditions: p=60 bar T=900 K

Figure 26: Single shot images from the LII setup (OH* chemiluminescence, LII, DBI light absorption and calculated KL factor) for low sooting conditions (a) and highly sooting conditions (b). Injection pressure 1000 bar, image taken 6 ms after start of injection.

LII performs well for low sooting conditions, with low absorption of the laser beam, as visible on Figure 26a. Correlation between the DBI and LII image is good and all soot regions appear on both of LII and DBI images. The stripes in the LII image originate from imperfections in the laser beam profile and could be eliminated by expending the laser beam using a micro-lens array instead of a simple cylindrical lens. Quantification under low sooting conditions, where laser sheet absorption as well as LII signal attenuation remains relatively low, is well possible. Under highly sooting conditions (Figure 26b), the laser can only penetrate through the lower part of the soot cloud. Towards the upper part of the soot cloud the laser fluence drops below the necessary threshold and the LII signal is weak, although the DBI image shows considerable soot absorption far upstream of the LII signal. Based on the principle of LII, quantification is only possible for the regions, where the laser fluence exceeds the soot sublimation threshold. This was apparently not the case in Figure 26b. For very highly sooting conditions even the DBI does not yield reliable results since the transmitted light drops to a very low level in comparison to the photoelectron noise of the camera.

To assess the upper limit for the soot detection with the LII method, a configuration with the laser sheet directed to the side of the soot cloud was used. In this way the DBI camera was looking along

the direction of the laser sheet. The LII images were calibrated by using the DBI images and corrected for the signal absorption based on the averaged DBI image under the assumption of axial symmetry. By using this calibration, averaged DBI and the averaged calibrated LII image should be equivalent if the soot amount does not exceed the calibration limitation of the LII imaging.

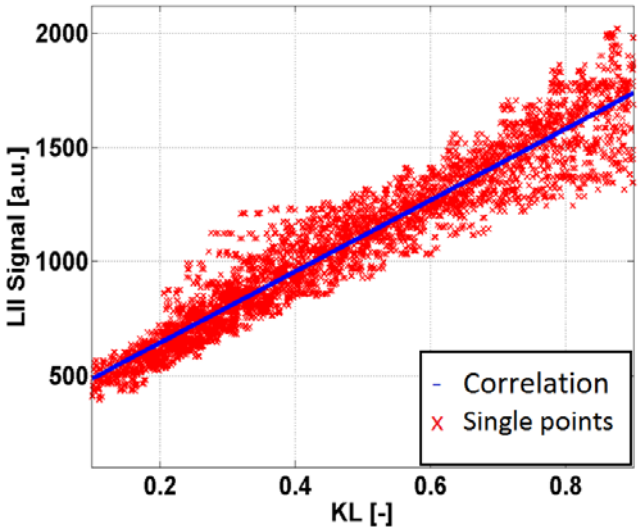

Figure 27: Correlation of the LII signal with the KL value obtained from the DBI imaging.

Figure 27 shows a pixel by pixel comparison of the detected soot KL distribution obtained by DBI with the LII measurements based on the calibration approach described above. Up to a KL value of 0.8 the LII results can be reliably quantified while beyond this soot optical thickness the LII methodology only provides qualitative information. A KL value of 0.8 corresponds to moderately sooting conditions.

4.2. Soot detection via DBI and 1D-spectroscopy

The line-of-sight DBI technique is fairly straightforward to implement and has been successfully applied at the HTDZ as a calibration tool for the LII imaging, as described in the section 4.1. Quantification of DBI is straightforward; however, the technique still suffers from some sensitivity to gradients of the refractive index along the beam path. This cross-sensitivity results in a false absorption signal in the DBI images in the regions with no soot but strong temperature gradients (visible in Figure 26). It is challenging to separate this interference from the actual soot absorption, which can be problematic under low sooting conditions like in dual-fuel engine applications.

Recently, an improved illumination strategy using an engineered diffusor optic at a close distance to the combustion chamber window has been proposed [22]. Engineered diffusors provide perfectly diffuse illumination contrary to simpler approaches using ground glass plates as diffusing objects. A significant suppression of the unwanted interference has been achieved. Based on those recommendations, a new DBI setup has been designed for use at the RCEM.

Neither LII nor DBI techniques can provide information on the temperature of the soot cloud. The two-color pyrometry technique is able to provide this information; however, it suffers from relatively high noise due to the temperature calculation using only two channels. A setup for measuring the soot temperature has been devised, employing 1D spectroscopy of the flame emission. Therefore the soot temperature along the spray axis of cross the spray axis could be measured using a wide spectral range of wavelengths (300 nm – 610 nm). This setup applied in parallel to DBI imaging provides information on the soot quantity as well as the soot temperature. For further description please refer to Sections 5.6 and 5.7.

5. Application in a rapid compression-expansion machine (RCEM) for dual fuel combustion

The experimental methodology developed within this project (Sections 1-3) has been extended to enable high-speed data acquisition and was subsequently applied to study the dual-fuel combustion at the RCEM facility of ETH Zürich. The active laser-based diagnostics were complemented by simultaneous passive high-speed acquisition of OH* chemiluminescence and Schlieren imaging. This section contains a description of the experimental setup and geometry, the experimental measurement matrix, the optical diagnostic setup and a synthesis of the most important findings.

5.1. Adaptation of the RCEM cylinder head geometry and determination of the boundary conditions

The dual-fuel experiments were scheduled to take place at the newly developed FRCM (flexible rapid compression machine) of ETHZ. Due to severe difficulties and various challenges in the development of the new FRCM (framework of CCEM Project 901: Flex-Fi-Dual), experimental investigations of the dual-fuel combustion could not take place as scheduled in the project (commissioning of FRMC delayed to 2017). However, in order to be able to fulfil the project tasks all experimental dual-fuel investigations will be performed at the existing Rapid-Compression-Expansion Machine (RCEM) at ETH Zürich.

Compared to the new FRCM, the existing RCEM has some disadvantages, namely: smaller cylinder bore, low turbulence, less flexible optical access and a free-floating piston.

In the first stage, various measures have been undertaken in order to mitigate these disadvantages to a best possible extent. The existing RCEM combustion chamber geometry, previously used for dual-fuel tests by Schlatter et. al.[23-25], has been adapted in order to provide necessary optical access along two axes (Figure 36). The newly constructed cylinder head offers a side window for laser illumination (Ø36 mm) and coaxial windows in the cylinder head and in the piston for visualization purposes (Ø52 mm each). A problem of a small cylinder bore has been overcome by the side injector mount, which enables an unobstructed spray path of 84 mm. A single-hole coaxial injector is mounted from the cylinder periphery in a specially designed holder. The coaxial single-hole injectors with a nozzle diameter of 100 µm, acquired within a preceding CCEM Project #703: NOx-reduction, were employed. The section of the combustion chamber with optical access along the piston axis extends from 16 mm to 68 mm from the injector orifice. In this configuration the existing setup offers sufficient optical access to perform the planned experiments.

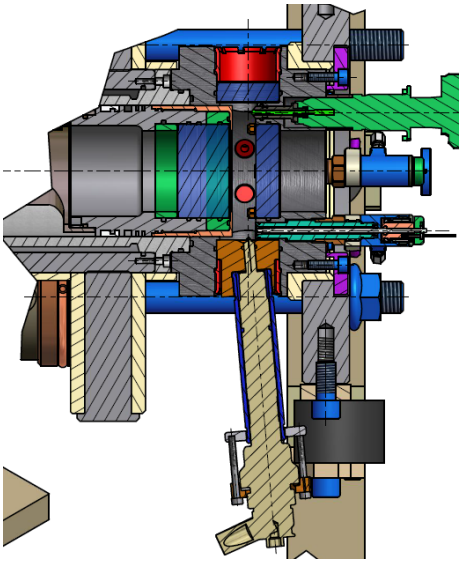

Figure 28: RCEM cylinder head geometry developed for dual-fuel combustion studies.

The RCEM charge temperature distribution prior to compression has been investigated by Schlatter et.al using five thermocouples at different radial and axial distances from the cylinder head. The highest detected standard deviation of the volume averaged temperature distribution in the cylinder was 2.67 K, which indicates excellent homogeneity of the temperature field. The newly designed setup features the same distribution of heaters along the cylinder liner and a very similar heater arrangement in the cylinder head. Same settings of the heating system as used by Schlatter were therefore used in the present project without repeated characterization of the temperature field.
For the preparation of a homogeneous methane-air mixture a hollow-cone Siemens-VDO A-Nozzle injector has been employed (hatched green part in Figure 28). Methane is injected directly into the combustion chamber with an injection pressure of 60 bar at a time approximately 3.5 s – 5.0 s before the rapid compression event. The long time available and the high injection pressure should ensure a homogeneous mixture of methane at the time of compression. This assumption has been verified using a specially designed test setup (Figure 29). The setup reproduced the cylinder head geometry of the RCEM with the piston in the BDC and provided optical access along the whole length of the cylinder by using a fused silica cylinder with an inner diameter of 84 mm. The covers were machined out of aluminum and anodized to suppress the scattering of the laser sheet. The first cover houses inlet and outlet ports for gas exchange, the injector being mounted at the same position as in the RCEM. The second cover holds a sapphire window for the purpose of laser illumination. Both covers are electrically heated and the quartz cylinder heating has been realized by heated gas circulation inside and outside of the cylinder.

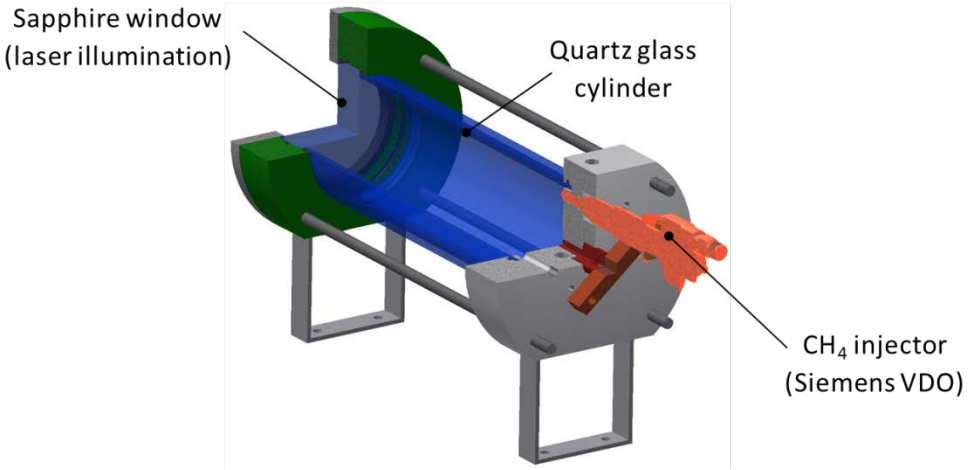

Figure 29: Geometry of the test setup of characterization of methane distribution in the RCEM.

The setup ensured equivalent charge conditions as in the RCEM prior to compression (pressure, temperature). Methane has been doped with a 0.11% molar concentration of anisole ($C_6H_5OCH_3$) using a heated bubbler system, similar as used for tracer characterization in Section 2.1. The very low concentration of the dopant has been used in order to insure same flow characteristics through the injector as with pure methane. The dopant in the methane has been excited using the 4th harmonic of a flashlamp-pumped Nd:YAG laser (266 nm) with laser sheet dimensions of 84 mm x 1 mm and a pulse energy of approximately 18 mJ and 10 Hz repetition rate. The LIF signal of the dopant has been collected with an ICCD camera using a 45 mm f/1.8 UV imaging lens and a bandpass filter around 285 nm - 340 nm (Schott DUG11). Laser synchronization with the camera and the gas injector has been achieved using a combination of pulse and delay generators. A time up to 5 s after injection has been recorded and resolved with 50 images in this time. This does not allow to temporally resolve the jet evolution during the injection itself (injection duration is 30 ms). However, the jet mixing is expected to be a rather slow process and therefore the 10 Hz temporal resolution suffices to trace gas plume evolution at a later time instance. High pulse energy of the flashlamp-pumped laser ensures high image quality.

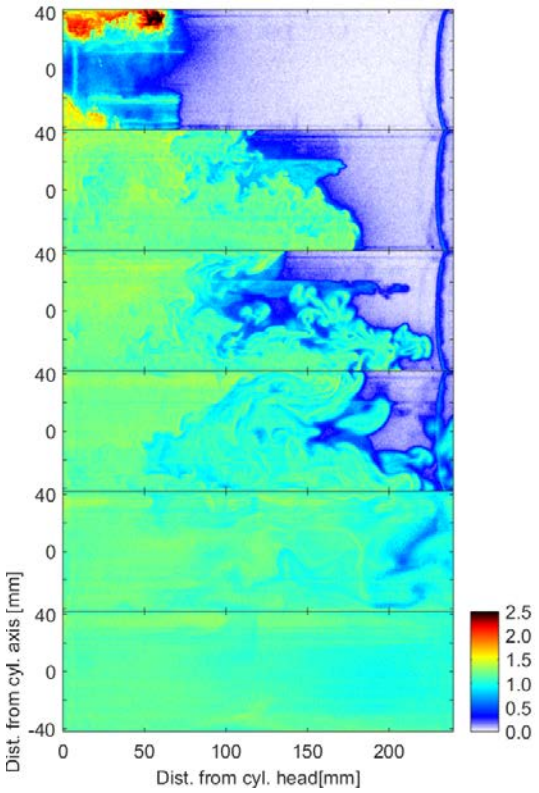

Figure 30: Single shot mixing evolution for 6 times after SOI (5 ms, 100 ms, 200 ms, 500 ms, 1500 ms, 4000 ms) normalized to the homogeneous concentration signal.

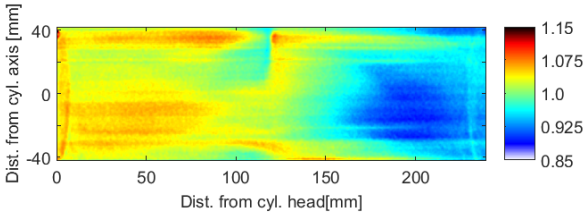

Figure 31: Average (80 repetitions) distribution of methane 4 s after injection, normalized with a fully homogeneous concentration.

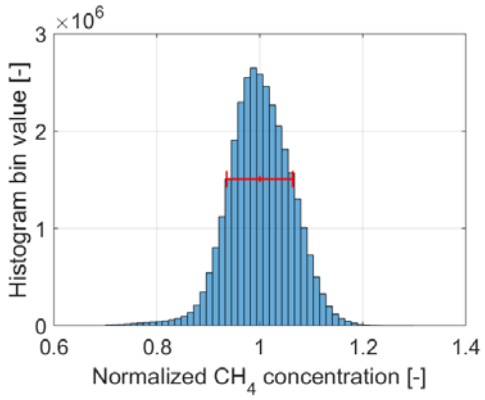

Figure 32: Histogram of detected methane concentrations at a time 4 s after SOI, normalized to fully homogeneous concentration. Red line indicated the standard deviation of the histogram (σ = 0.068)

The developed experimental setup and the selected tracer allowed for high-quality images of the methane mixing process from the SOI up to late in the mixing process (5 s after SOI). Figure 30 shows single shot evolution of methane concentration field for six time instanced after the injection ranging from 5 ms to 4 s after SOI. During the injection and shortly afterwards the high momentum of the injected gas provides rapid penetration of the gas plume, however, the momentum quickly dissipates after EOI and the gas plume needs up to 0.5 s to reach the opposite end of the glass cylinder. The asymmetric injector mount locations (37.5 mm from the cylinder axis, same geometry as the RCEM) results in deformation of the axially-symmetrical hollow cone injector's plume, resulting in asymmetric penetration and distribution of the gas plume shortly after injection. The remaining large vortices provide further mixing after EOI; and by the time of 4 s after SOI high homogeneity of the tracer concentration is achieved. The slow progress of the mixing process confirms the selected operation strategy of the RCEM with the methane injection way in advance of the compression cycle.

The extent of the remaining inhomogeneity has been investigated by calculating the mean concentration field at a time of 4 s after SOI (Figure 31) and by plotting the histogram of the deviations of single shots from the homogeneous tracer concentration (Figure 32). The mean tracer concentration field shows some extent of repeatable inhomogeneity with larger gas concentration in the left half of the cylinder (the side of the gas injector). The range of this inhomogeneity is less than 10% from the homogeneous concentration. Single shot images reveal a higher range of inhomogeneities with a standard deviation of the distribution of $\sigma = 0.068$. This means that the inhomogeneity does not exceed 15% in 95% of the cylinder volume. In the actual RCEM, due to additional mixing during the rapid compression (wall-shedding vortex [26]), the inhomogeneity will be lower than in the glass cylinder setup.

This overall inhomogeneity of the methane distribution in the RCEM might be higher than in dual-fuel engines with port fuel injection but is smaller than in typical engines with direct fuel injection [27]. The

inhomogeneity might influence the laminar flame speed in different parts of the cylinder and therefore exhibit some influence on the heat release rate during the premixed flame propagation. The flexibility of the RCEM machine allows however for a very large variation of the premixed equivalence ratio. By investigating a large range of the premixed equivalence ratio the influence of the inhomogeneity will be small comparing to the experimental variations of the equivalence ratio itself. The influence of the inhomogeneity on the ignition delay is not expected to contribute significantly, which has been confirmed by the very small variability of the ignition delay observed during the experiments (Figure 37).

5.2. Realized measurement campaigns

Five measurement campaigns were realized at the RCEM of ETH Zürich, with overall over 3800 cycles acquired. Table 1 gives an overview of the dual-fuel measurement campaigns realized within the project.

Table 1: Overview of dual-fuel measurement campaigns at the RCEM

Measurement campaign	Aim of investigation	Variations	Experimental diagnostics
Campaign 1	Exploratory measurement campaign. First test of the new dual-fuel combustion chamber geometry and feasibility study.	Charge temperature, methane equivalence ratio, pilot injection pressure and duration, EGR, fuel (72 points, 720 cycles)	Simultaneous Schlieren and OH* chemiluminescence imaging Pressure sensing for HRR analysis
Campaign 2	Pilot fuel mixture formation under non-reactive conditions	Charge temperature, pilot injection pressure and duration, laser sheet position (52 points, 520 cycles)	High-speed TMPD tracer PLIF with simultaneous Schlieren and Mie scattering imaging
Campaign 3	Low-temperature combustion stage, high temperature ignition and transition to flame propagation, soot precursors	Charge temperature, methane equivalence ratio, pilot injection pressure and duration, EGR (80 points, 800 cycles)	High speed CH_2O PLIF with simultaneous Schlieren and OH* chemiluminescence imaging Pressure sensing for HRR analysis
Campaign 4	Spray penetration, high temperature ignition and transition to flame propagation. Focus on points with very short and very long ignition delay. Investigations with alternative fuel (OME)	Charge temperature, methane equivalence ratio, pilot injection pressure and duration, EGR, fuel (128 points, 1280 cycles)	Simultaneous Schlieren and OH* chemiluminescence imaging Pressure sensing for HRR analysis
Campaign 5	Spectral emission of dual fuel combustion. Investigation of sooting propensity of combustion.	Charge temperature, methane equivalence ratio, pilot injection pressure and duration, EGR, fuel (60 points, 600 cycles)	High-speed 1D spectrographic acquisition of flame luminosity combined with DBI for soot absorption measurements, Pressure sensing for HRR analysis

The Campaign 1 has been realized in order to test the newly developed RCEM dual-fuel setup and geometry. The main aim of the investigations was to determine the range of conditions of interest.. The limitations of the hardware were tested as well to determine the range of conditions accessible by the machine.. The target was to perform investigations under a broad range of engine relevant conditions. The limitations were the ignition location (the ignition location has to be within the window area) and safe operation of the test rig. For brevity no results are presented in this report since the results largely overlap with the results of Campaign 3; nevertheless, the data acquired in this measurement campaign has been processed and is included in the CFD validation database.

The measurement Campaign 3 is the main experimental campaign investigating all stages of dual-fuel combustion (cool flame onset, high temperature ignition and transition to the premixed flame propagation). An extensive measurement matrix with wide variation of the experimental parameters has been investigated. The matrix of variations of Campaign 3 is shown in Table 2 with bold values representing the standard cases. The main scientific results are presented in Sections 5.4 and 5.5. The pilot injection under non-reactive conditions has been investigated in Campaign 2 in order to provide information on the pilot-fuel mixing boundary conditions. The same conditions were used as in the Campaign 3. Results of the measurement Campaign 2 are presented in Section 0.

Table 2: Matrix of variations in Campaign 3.

Variation	Variation values
Temperature at SOI	770K, **810K**, 850K
Pilot injection (inj. pressure, energizing time)	600bar 300µs ET **600bar 400µs ET** 600bar 500µs ET 1000bar 300µs ET
Methane air to fuel ratio λ	∞, 3.0, **2.1, 1.9, 1.7**, 1.5
Oxygen content (EGR)	**21%,** 18%, 15%

Measurement Campaign 4 was realized in order to complement the measurement matrix of Campaign 3 with further points of interest identified in previous results. Two sets of points were acquired with different goals: A set of points with very short injection duration and high EGR rate to reach spray lean-out conditions. The second set includes points with the same ignition delay but different background methane (achieved by adapting the temperature accordingly with the methane concentration). The goal was to observe the influence of methane at otherwise equivalent mixture fraction evolution of dodecane. Measurements were processed with the same routines as points of Campaign 3; the results were added to the experimental database.

Finally, the measurement Campaign 5 focused on characterization of the sooting behaviour of the dual-fuel combustion with simultaneous acquisition of spectrally resolved natural luminosity of the dual-fuel flame. The goal of the measurement campaign was two-fold: First, the extent of the light emission around 310 nm (OH* acquisition of Campaigns 1, 3, 4) originating from OH* radical luminosity was determined and possible interferences were quantified (results described in Section 5.7). Secondly, the amount of soot and the soot temperature were determined based on the DBI imaging and the spectroscopic acquisitions (results in Section 5.6).

5.3. Pilot-fuel mixing characterization

Evolution of the mixture fraction distribution of the pilot spray is expected to influence strongly the ignition timing and the ignition location as well as the HRR during the pilot fuel combustion. In order to characterize the distribution of the pilot fuel, a setup for acquisition of high-speed TMPD tracer PLIF with simultaneous high-speed Mie-scattering and Schlieren imaging has been realized (sketch in Figure 33). TMPD tracer PLIF provides quantitative information on the pilot fuel vapor distribution. Since in the regions with presence of liquid fuel the tracer-PLIF quantification fails, Mie-scattering imaging of the liquid phase was performed simultaneously. Additional Schlieren imaging provided information on the extent of the fuel jet and helps separating the PLIF signal from the possible background luminosity.

For the purposes of tracer PLIF acquisition the Diesel surrogate fuel (n-dodecane) has been doped with a low concentration of a fluorescent tracer (TMPD, 1.5 g/l). The tracer has been excited with a laser beam of a high-speed 3rd harmonic Nd:YAG laser (wavelength 355 nm), formed into a laser sheet using a combination of a cylindrical and a spherical lens. A mirror directed the sheet frontally onto the fuel spray. The TMPD PLIF signal was detected using an intensified high speed camera. Simultaneously, Mie scattered laser light was detected using a second high speed camera. Parallel Schlieren imaging has been detected with a third high-speed camera in combination with Schlieren optics illuminated by a. Cavilux laser diode emitting around 690 nm. The light output of the Cavilux diode has been focused onto a diffusor plate (omitted in the Figure) which was closely coupled to a pinhole with a diameter of 1 mm. The light passing through the pinhole was collimated using an achromatic lens and directed through the combustion chamber of the RCEM. On the camera side the light beam was focused onto a Schlieren cutoff (an iris orifice, 3 mm in diameter) collected with an imaging lens on the camera chip. Spectral separation of the Schlieren light source and the detection wavelength of TMPD PLIF (NUV/violet) enabled simultaneous detection along the same axis by use of two dichroic mirrors reflecting the short wavelengths to the corresponding cameras and transmitting the Schlieren light beam.

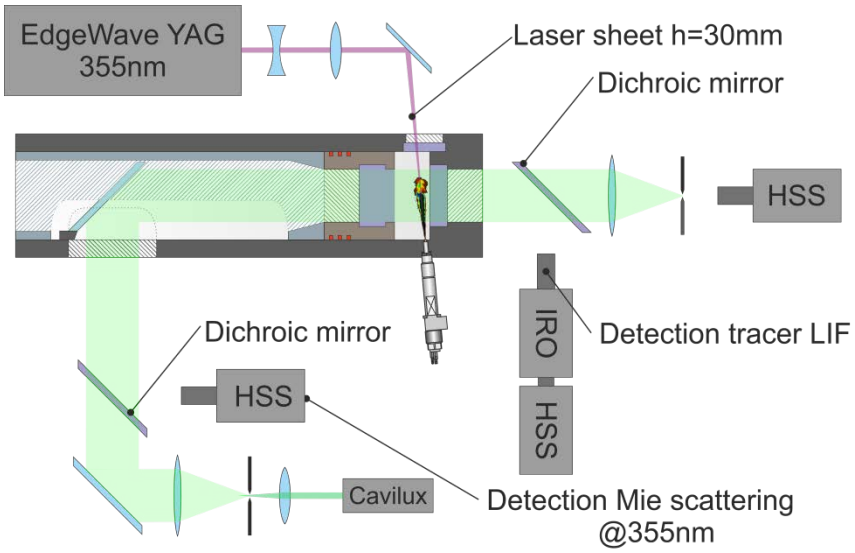

Figure 33: Optical setup for simultaneous high speed TMPD tracer PLIF, Schlieren, and Mie scattering imaging at RCEM

The main goal of investigations in Campaign 2 was to provide quantitative measurements of fuel concentration fields during the complete pilot spray evolution event. A careful calibration procedure has been devised to reach the highest possible level of quantification. Before each experiment a

correction of the laser sheet profile and the vignetting of the camera lens has been performed by acquisition of tracer LIF images of homogeneously seeded tracer vapor in the RCEM. The tracer was seeded using a bubbler system. The seeding tracer concentration has been kept constant throughout the experimental campaign in order to provide a relative reference between the different intensifier gain and lens aperture settings used in the different experiments.

The relative LIF signal has been calibrated into the absolute fuel concentration by the known injected mass of the fuel. In axially-symmetric configurations this is possible with an average PLIF image if the injector axis lies within the laser sheet plane [9, 28]. This simplification is not applicable in the RCEM since spray might not be axial-symmetric due to the piston motion during the injection. A series of experiments with the laser sheet positioned in parallel to the cylinder head at seven distances (1.5 mm to 13 mm) from the cylinder head were carried out. This range of laser sheet positions encloses the complete spray up to a time approximately 3 ms after injection. Since the total injected mass is constant and known, averaged acquisitions of this series are used for the absolute quantification of the measurements. Figure 34 shows a comparison of the total injected fuel mass with measurements by tracer PLIF for different pilot injections. Overall, a good agreement of measurements after the end of injection has been achieved. Immediately after end of injection, the measured value overshoots the injected mass by up to 30%. Partially, this has been attributed to the contribution of scattered light and reflection on the window surfaces, which is significant due to the low clearance between piston and cylinder head around TDC. Another reason for this discrepancy is probably an error in the assumed fluorescence yield of the tracer (assumed from [10]) under very high temperature conditions. Based on this test, the estimated precision of the quantification of tracer LIF is at the moment around 20%. This is sufficient to characterize the fuel mixing for different pilot injections and to support the analysis of the reactive experiments by providing the information of the most-reactive regions of the pilot fuel jet.

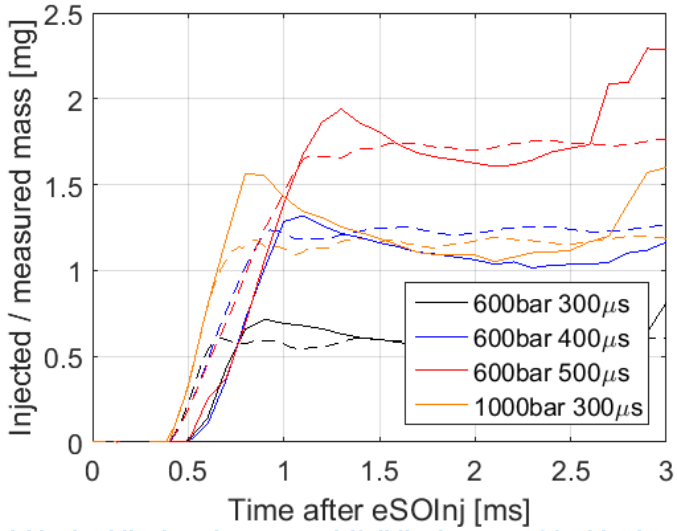

Figure 34: Total injected (dashed line) and measured (full line) mass of fuel in the pilot spray for different pilot spray injection pressures and injector energizing times.

Following the series of experiments at different laser sheet positions, a series of tracer LIF experiments with a parametric variation of temperature and pilot injection (pressure, energizing time) has been performed. A single laser sheet position was used with the laser sheet directed onto the nozzle exit inclined 3.5° away from the cylinder wall. The reason for not selecting a laser sheet position aligned with the injector axis (5° inclined) was to compensate for the ongoing compression during the injection event (start of injection 4 ms before TDC). The ongoing compression will constrict

the spray and push the most reactive spray zones closer to the cylinder head. The precise position of the laser sheet has been determined in a series of experiments in Campaign 1, where tomographic detection of the ignition location (x, y, and z distance from the injector, through main and side window) has been performed under different conditions. The selected inclination of 3.5° corresponds to a fit through the ignition locations, so that the laser sheet captures most of the ignition events.

In Figure 35 an example of high-speed tracer LIF acquisition is shown combined with a simultaneously acquired Schlieren sequence. The image demonstrates the difference between the line of sight Schlieren and cross-sectional methodology of tracer-PLIF. Schlieren imaging is very sensitive to gradients and therefore delivers strong signals even in regions with very low concentration. From Schlieren imaging no information about local fuel concentration is available. In this respect tracer PLIF is clearly superior. Furthermore, information about size and dynamics of the internal vortex structure can be extracted. The disadvantage of tracer PLIF in Diesel and ‘dual-fuel’ applications is the very large dynamic range of the camera needed to fully resolve the complete process, as also demonstrated in Figure 35. The liquid phase of the spray gives rise to very bright regions, while due to compression related temperature increase (ca. 100 K in 2 ms) and fuel mixing process very low signal is detected in the late times after injection.

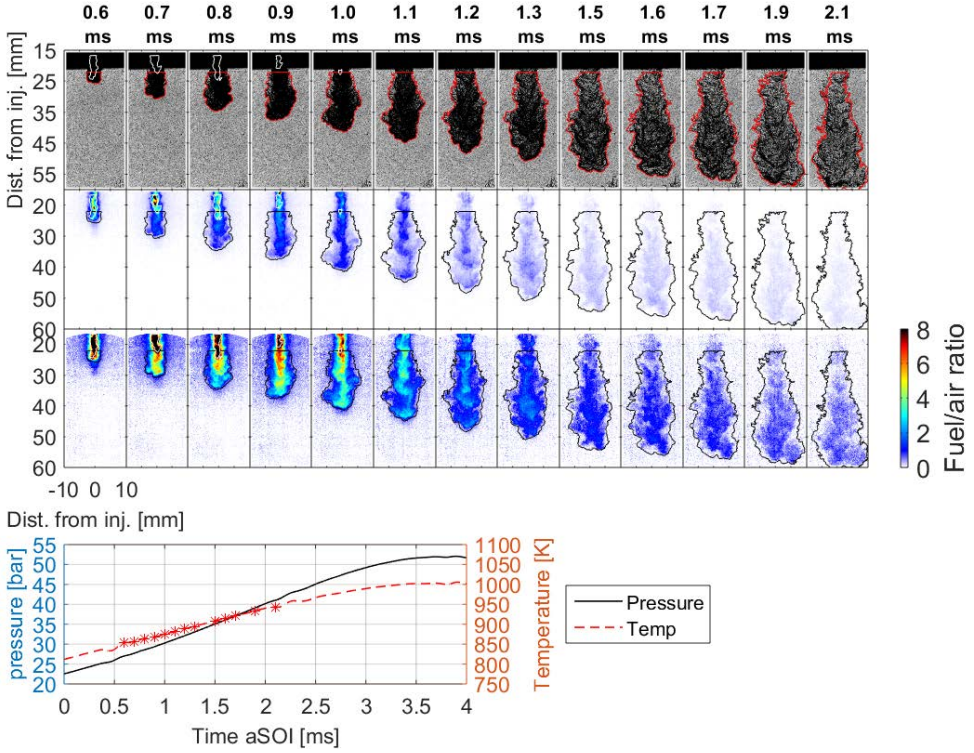

Figure 35: Example of a single high-speed acquisition of tracer-PLIF at different times after start of injection. In the top row Schlieren images are presented, the middle row shows raw tracer-PLIF images and the bottom row fuel/air ratio (quantified tracer PLIF). The overlapped contours are based on simultaneous Schlieren (red, black) and Mie scattering imaging (white). The diagram shows the pressure and temperature curve during the injection event, with stars marking the times at which images were captured..

To mitigate the problem of low tracer LIF signal intensity late after the end of injection a second set of experiments was performed, where the camera exposure started 1.2 ms after start of injection and therefore not acquiring in the period when high density liquid regions are present. This enables increasing the signal-to-noise ratio in late stages of spray event by opening the camera lens aperture

and increasing the intensifier gain. The disadvantage of this approach is that the initial stage of spray formation (1.1 ms) is not acquired. Figure 36 presents an example of image series using late camera triggering. Improvement of signal-to-noise ratio is large and using this approach it is possible to trace pilot fuel spray beyond 2.5 ms after start of injection. Furthermore, images in Figure 36 demonstrate that in the late stages of spray large structures develop, which are not anymore governed by the turbulence of injection. This would not be possible to observe without application of laser based diagnostics.

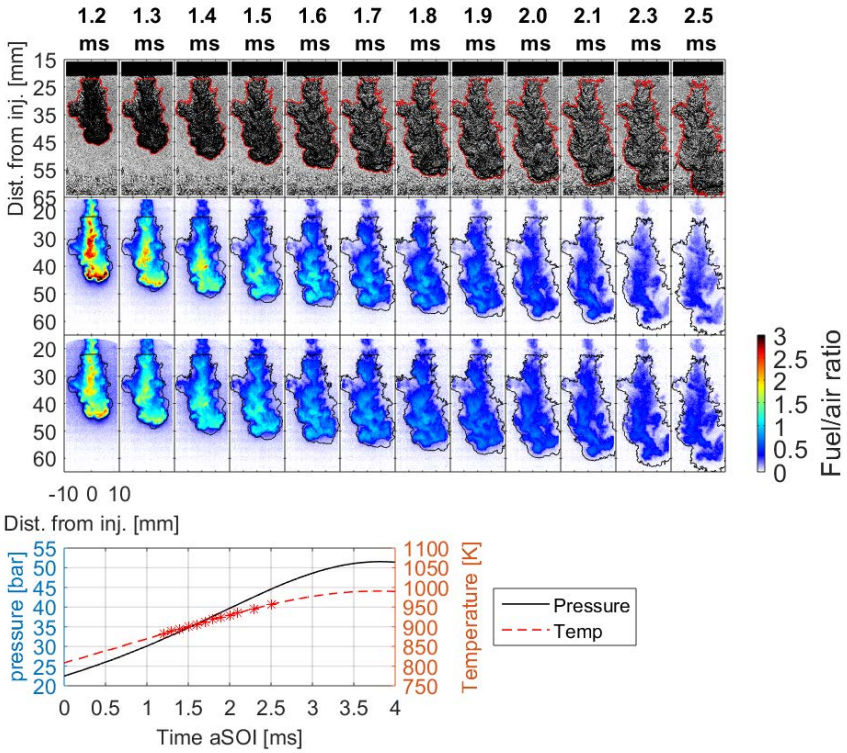

Figure 36: Example of a single high-speed data acquisition series at different times after start of injection. The camera exposure started 1.2 ms after SOI. The middle row shows raw tracer PLIF images and the bottom row fuel/air ratio (quantified tracer PLIF). The overlapped contours are based on the simultaneously recorded Schlieren signal (red, black) depicted in the first row. The diagram at the bottom shows the pressure and temperature curve during the injection event, with stars marking the times at which images are plotted.

The information from the campaign 2 has been used to assist the interpretation of the reactive experiments of campaigns 3, 4 and 5.

5.4. Sensitivity of ignition delay on CH_4 concentration

The reactive dual-fuel tests have been recorded with an optical setup including simultaneous high-speed CH_2O-PLIF imaging, Schlieren imaging, and OH* chemiluminescence imaging together with cylinder pressure sensing for calculations of HRR (heat release rate). CH_2O-PLIF imaging has been selected instead of the initially proposed OH-PLIF since the exploratory measurement campaign 1 indicated a large sensitivity of the methane concentration on the low-T ignition. It is only possible to identify this influence by the detection of CH_2O. Instead of OH-PLIF the CH_2O imaging has been complemented by OH* chemiluminescence to provide information on the high-T combustion.

The experimental setup was very similar to the setup used for tracer-LIF imaging (Figure 33) and is therefore not sketched again here. The same Schlieren configuration with dichroic mirrors used for separating the short wavelength light has been applied. The difference is that instead of the Mie scattering camera an OH* chemiluminescence camera system was used (i.e. a high speed camera with image intensifier and bandpass filter at 310 nm). For CH_2O-PLIF imaging the same laser sheet configuration as for tracer-LIF has been used. On the detection side a high-speed intensified camera, equipped with a visible light photographic lens and a bandpass filter, transmitting between 400 nm and 480 nm, has been used.

Dual-fuel combustion typically consists of three combustion stages: Pilot fuel ignition, transition stage and premixed combustion stage. In this section the main results and understanding of the methane interaction with the pilot fuel ignition are described. Section 5.5 describes the scientific results and understanding regarding the transition and premixed flame propagation stages.

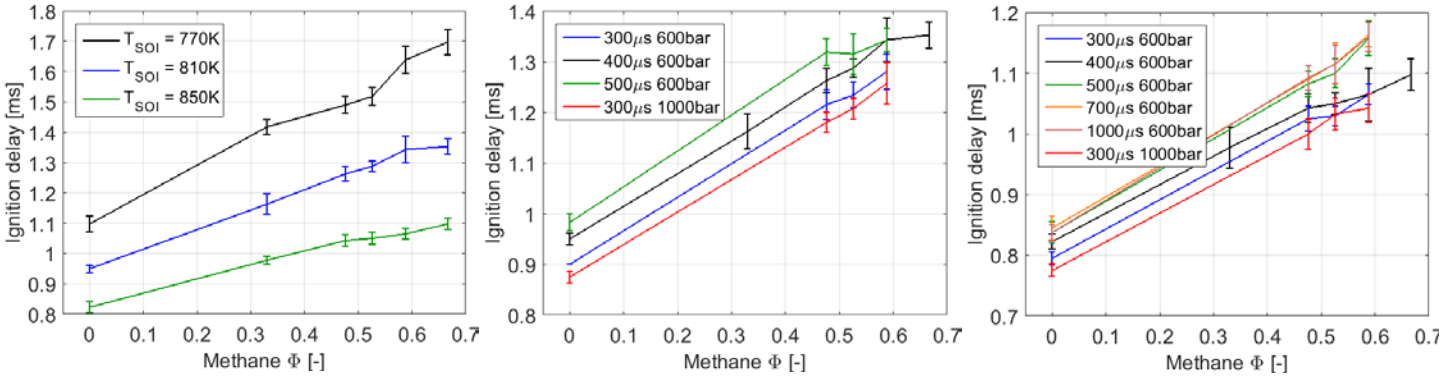

Figure 37: Ignition delay dependence on methane equivalence ratio. Temperature variation ((a), pilot injector pressure 600bar; 0.4 ms energizing time); pilot injection p and ET variation ((b) T=810K, (c) T=850K).

Considerably longer ignition delays compared to pure Diesel operation are a general characteristic of dual-fuel combustion. This phenomenon has been observed before for Diesel fuel and n-heptane [23, 25, 29]; it has been reproduced here also for n-dodecane Diesel surrogate fuel (Figure 37). The sensitivity of ignition delay depends on temperature with increasing sensitivity at lower temperatures due to lower reactivity (Figure 37a). A similar effect has been observed when reactivity has been decreased by means of EGR. In addition, it has been observed that different pilot injection strategies consistently show different ignition delays (Figure 37b and 8c)). Pilot injection strategies featuring small injection amounts or high injection pressures (600 bar 300 µs and 1000 bar 300 µs pressure and energizing time, respectively) show up to 0.1 ms shorter ignition delay than longer injections. This effect has been attributed to an earlier occurrence of highly reactive mixture fractions due to the so-called entrainment wave which evolves after end of injection [30]. The effect is present both under high temperature and medium temperature conditions while low temperature conditions do not show this effect.

Though the retardation effect of methane on Diesel ignition has been observed before, little is known on the exact mechanism of the methane interaction. Some authors [25] suggested that the influence of methane originates mostly due to the high thermal capacity of methane and lower oxygen availability due to the mixing of the less reactive methane into the air. Based on the CH_2O-PLIF imaging, we investigated which stage of ignition is influenced by the presence of methane and to what extent does methane participate in the low temperature ignition process. Figure 38 shows in the left the

comparison of the high-temperature (solid line) and low temperature (dashed line) ignition delays under different conditions. The most interesting finding is that under the investigated conditions the low temperature ignition delay precedes the high temperature ignition by 400-500 µs, independently of conditions. This indicates that from the first appearance of CH_2O, the ignition process proceeds similarly regardless of the methane and temperature conditions. Based on this feature it was concluded that methane mostly influences the low-temperature ignition stage of the dodecane fuel.

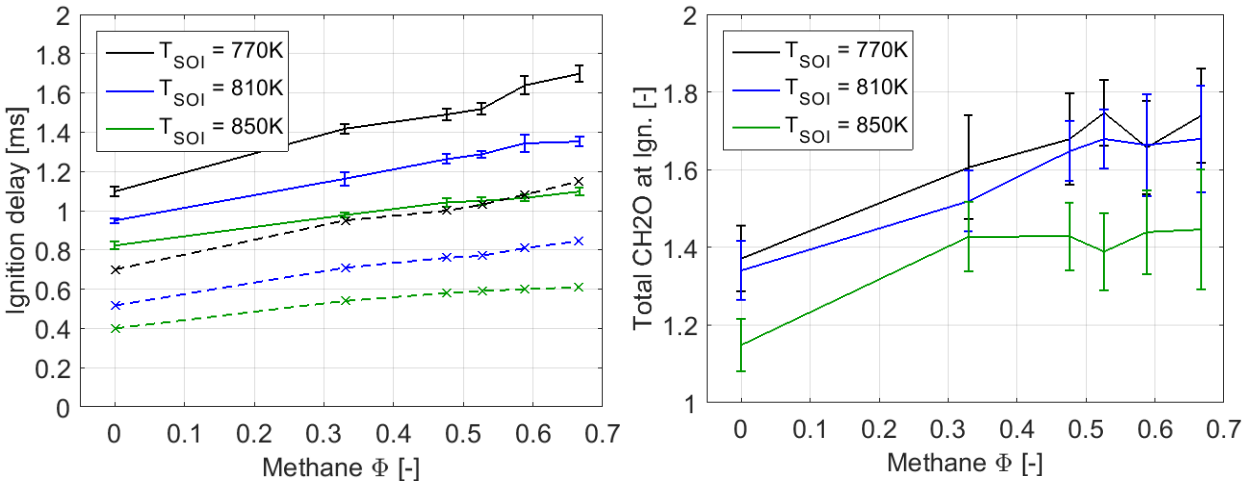

Figure 38: (a) Ignition delay dependence on methane equivalence ratio (solid line) and low-temperature ignition delay dependence on temperature (dashed line). (b) Dependence of total detected CH_2O signal before high-temperature ignition on temperature and methane equivalence ratio.

The participation of methane in the low temperature combustion process was investigated by comparison of the maximal total CH_2O signal before ignition (Figure 38 right). Independent of temperature, the amount of CH_2O signal increases for approximately 20% when changing from Diesel operation to $\lambda_{CH4} = 1.7$. When comparing the influence of temperature, 770 K and 810 K cases show very similar values of peak CH_2O signal while the 850 K case shows approximately 15% lower peak values. Regardless of the CH_2O-PLIF signal not being quantitative, this result does indicate that presence of methane promotes higher CH_2O concentrations in the auto-ignition sequence. These measurements do not, however, allow concluding whether this is due to part of methane being converted to CH_2O or whether methane promotes fuel decomposition over the CH_2O path.

In order to gain further understanding of the chemical interaction of methane in the ignition process, 0D chemical simulations have been performed. Constant pressure batch reaction code included in the reactor network package of Cantera [31] software has been used. A gas mixture with the specified equivalence ratios of dodecane and methane has been initiated in the numerical reactor model. The code calculated the evolution of species concentration and temperature in time. Based on this, the low-T ignition has been defined as the time of peak production of CH_2O and high-T ignition as the time of peak HRR. Simulations have been performed for a range of initial conditions (variation of temperature, pressure, dodecane- and methane equivalence ratio). The chemical mechanism used for the majority of the simulations was the LLNL n-alkanes detailed chemical mechanism [32] containing approximately 7200 species. For some computationally expensive calculations simpler skeletal mechanisms containing 254 [33] and 106 [34] species have been used. The performance of the skeletal mechanisms under the investigated conditions has been validated by comparison to the detailed chemical mechanism. The change of the mixture temperature due to the adiabatic mixing of

the cold evaporated fuel with the hot air has been accounted for by adapting the initial temperature of the gas mixture in the reactor accordingly.

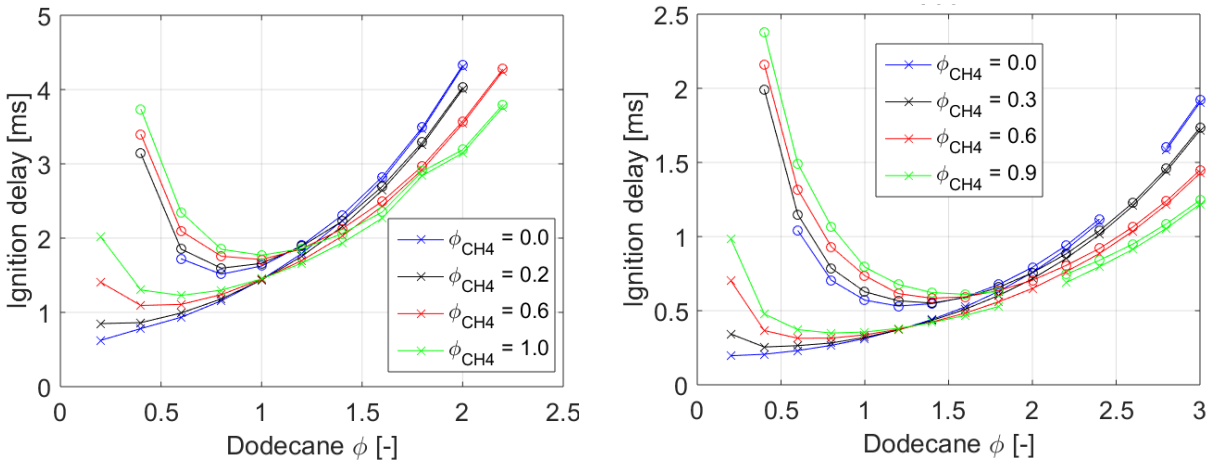

(a) 800 K (b) 900 K

Figure 39: Low-T (crosses) and high-T ignition delay (circles) dependence on the methane and dodecane equivalence ratio for air charge temperature of 800 K (a) and 900 K (b).

The simulation results for two temperatures at a charge pressure of 30 bar are presented in Figure 39. Simulations predict a significantly increased low-T ignition delay of lean dodecane mixtures in the presence of methane. Consequently also the high-T ignition delay increases for the lean pilot fuel mixtures. The retardation is higher at lower temperature conditions. A reverse influence of methane has been predicted under dodecane fuel-rich conditions where only small temporal separation of the low- and high-T ignition is predicted. The influence of methane increases with increasing methane concentration. The strong retardation effect of methane on pilot-fuel lean mixtures explains the misfire phenomena for too short pilot injections. Fuel rich mixtures in short injections cease to exist earlier in the cycle than in the case of longer fuel injections resulting and an over-proportional increase of the ignition delay due to the methane presence. This leads to misfire or poor combustion timing.

With regard to the methane influence on the spray ignition delay, the simulations predict a shift of the most reactive mixture fraction to higher pilot-fuel mixture fraction and a small increase of the ignition delay at the most reactive mixture. This prediction is in line with the experimental observations. Experiments, however, show higher sensitivity of the overall ignition delay on methane than predicted. In order to understand the complete influence of methane, the turbulence-chemistry interaction has to be taken into account. Recently, Dahms et. al. [35] presented a concept explaining the influence of turbulence-chemistry interaction on Diesel spray ignition by a so called turbulent ‘cool-flame’ wave. They performed Lagrangian flamelet simulations including the terms for turbulence-chemistry interaction for a range of scalar dissipation rates. Their simulations showed a shift of the most reactive mixture towards higher mixture fraction and a decrease of the ignition delay with increasing scalar dissipation rate. This has been explained by the diffusion of low-T combustion products from the fuel-lean spray regions towards the regions with fuel rich conditions and therefore considerably accelerating the ignition of fuel-richer mixtures. This turbulent propagation of the low-T combustion from the fuel lean conditions to the fuel-rich conditions has been named ‘turbulent cool-flame wave’.

The ignition behavior of the dodecane spray can also be explained by the turbulent cool-flame wave which is expected to proceed differently owing to the influence of methane. We have performed 0D-CMC simulations at different scalar dissipation rates for a variation of scalar dissipation rates. The

simulation code has been provided by LAV ETHZ and features the turbulence-chemistry interaction similar to the models used by Dahms et. al.[35]. Figure 40 demonstrates the influence of the scalar dissipation rate on the evolution of the turbulent cool-flame wave based on the evolution of the CH_2O mass fraction. In cases without turbulent-chemistry interaction (SDR = 0), the 0D-CMC model becomes basically a set of non-interacting batch reactors with different dodecane equivalence ratios. The calculations show very steep gradients of CH_2O concentrations between the regions that have undergone low-T chemistry and slow spreading of CH_2O. In the presence of a SDR the first CH_2O appears at similar dodecane equivalence ratios and it diffuses towards dodecane richer regions and accelerates low-T reactivity in the dodecane-richer regions. The overall CH_2O concentration decreases and a much lower gradient of the CH_2O concentration has been predicted in comparison to the case with SDR = 0.

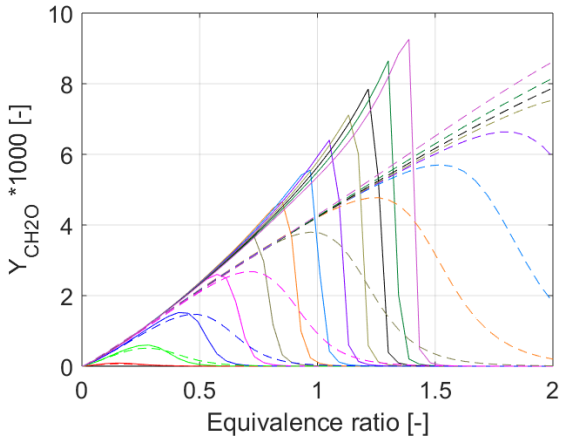

Figure 40: Evolution of CH_2O mass fraction in a dodecane-only case, calculated by using the 0D-CMC code with scalar dissipation rate SDR = 0 (full line) and SDR = 5 (dashed line). Conditions 850 K and 30 bar. Same color indicates same time instant; the lines are separated by 50 µs.

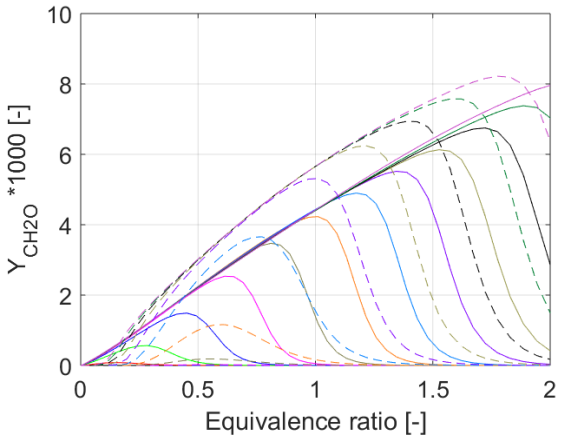

Figure 41: Evolution of CH_2O mass fraction in a dodecane only case (full line) and dual-fuel case (Φ_{CH4} = 0.5, dashed line). Conditions: T = 850K, p = 30 bar, SDR = 5. Same color indicates same time instant; the lines are separated by 50 µs.

In dual-fuel cases the batch reactor simulations predict highest influence of methane on increasing the low-T ignition delay in the dodecane-lean mixtures and therefore the first low-T reactivity occurs delayed and at higher dodecane concentrations. A similar influence of methane has been calculated by the 0D-CMC code with SDR = 5 (Figure 41). In the absence of methane the formation of CH_2O starts in the leanest dodecane mixtures and diffuses towards the fuel-rich mixtures. Methane inhibits low-T reactivity in the dodecane-lean mixtures. Therefore the first CH_2O is formed at Φ_{C12} = 0.6 delayed for 150-200 µs comparing to a dodecane only case. Afterwards the low-T combustion products diffuse in the mixture fraction space towards dodecane lean and rich mixtures in a form of a double cool-flame wave. Peak CH_2O concentrations are higher in dual-fuel cases resulting in faster spreading of the low-T reactivity.

Figure 42 shows the influence the SDR on the high-T ignition delay of dodecane and dual-fuel cases. Increasing SDR shifts the ignition location towards fuel richer conditions. The curve of ignition delay is very flat around the most reactive dodecane concentration due to the transport of radical and especially due to the diffusion of hot high-T reaction products from the already ignited zones. The methane influence trend reversal for dodecane rich conditions is not present in the presence of turbulence-chemistry interaction. An increase of the ignition delay with addition of methane is predicted for the whole range of dodecane mixture fractions. The methane influence on the retardation of ignition increases for higher SDR. Based on this simulation results, it can be concluded that the mechanism of the experimentally observed methane interaction with dodecane auto-ignition acts

through delaying the onset of the cool-flame wave in the dodecane-lean mixture fractions. The delayed cool-flame wave results in a later onset of reactivity in the dodecane-rich regions and therefore results in an increase of the overall fuel jet ignition delay.

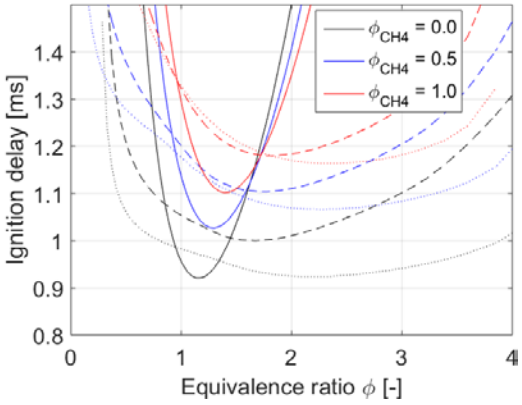

Figure 42: Influence of methane and dodecane equivalence ratio on the high-T ignition delay predicted by the 0D-CMC code for a variation of the SDR: SDR = 0 (full line), SDR = 5 (dashed line), SDR = 15 (dotted line). Line color indicates the concentration of CH_4.

A sensitivity analysis of the reaction rates on the methane concentration has been performed in order to understand the chemical mechanism of the methane interaction. It was identified that presence of methane results in significantly decreased concentrations of OH, H, HO_2,and other reactive radicals throughout the ignition process. On the other hand, concentrations of CH_3, CH_2, and O radicals increase. The reaction $CH_4 + OH \leftrightarrow CH_3 + H_2O$ was identified to be solely responsible for the retarded low-T reactivity in the fuel-lean mixtures. Up to 90% of the OH radical produced before the low-T reactivity is consumed by this reaction which produces the less reactive CH_3 radical and water. Methane reactions with other radicals show significantly lower sensitivity and do not strongly influence the ignition process.

5.5. Transition from ignition to premixed flame propagation

The influence of methane on the dual-fuel combustion ignition delay has been reported in the section above. Following the high temperature ignition, the volume of the pilot spray undergoes fast ignition resulting in rapid consumption of the pilot fuel. This flame kernel transits to a premixed flame, which is initially strongly non-adiabatic due to the presence of fuel-rich pilot-fuel regions. An example of ‘dual-fuel’ combustion acquisition is presented in Figure 43.

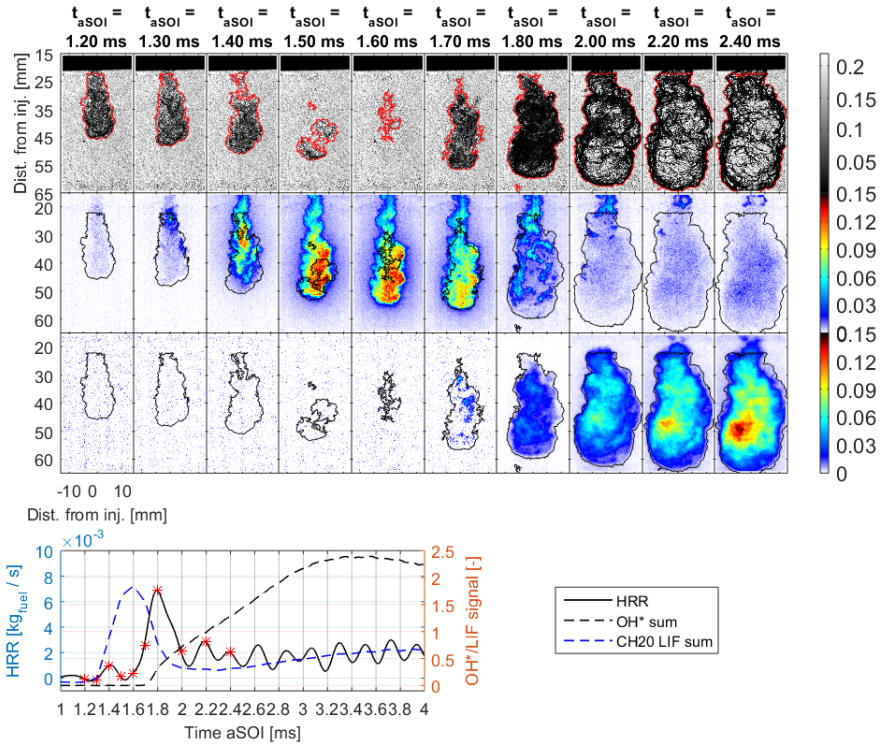

Figure 43: Example of a Dual-fuel combustion event. Conditions: Temperature at SOI = 810 K. Injection pressure was 600 bar, injector energizing time 0.4 ms. Methane: λ=1.7. The upper row shows Schlieren images, middle row high-speed CH_2O-PLIF images, bottom row OH* chemiluminescence. Overlapped contours are spray edges based on Schlieren images. The diagram at the bottom shows HRR, total OH* chemiluminescence signal, and total CH2O-PLIF signal. Stars indicate times when images were recorded.

The main stages of dual-fuel combustion can be seen in Figure 43. The auto-ignition extends over two stages. First, the low-temperature reactions take place, which can be detected by appearance of signals in the CH_2O-PLIF images. CH_2O, a product of low temperature combustion, is rapidly consumed in the high-temperature ignition stage of the auto-ignition. As visible from the CH_2O-PLIF images, first signals appear at the spray edges high upstream of the spray tip, approximately 0.5 ms before high temperature ignition. Low temperature combustion proceeds through the spray, and the CH_2O signal peaks right before the high temperature ignition. Low temperature ignition is also visible on the Schlieren images where the Schlieren signal softens due to the small amount of heat released in the process. However, this cannot be precisely detected without help of CH_2O-PLIF images. Following ignition, CH_2O is rapidly consumed and a transition to premixed flame propagation occurs. Interesting is the image at 1.8 ms after SOI, showing CH_2O in torn-up zones over the spray contour. This indicates less reactive zones in the spray plume, which take longer to auto-ignite and can therefore indicate the degree of homogeneity within the spray plume. Following consumption of CH_2O, the OH* chemiluminescence signal rises strongly and the premixed flame propagation initiates. Premixed flames cannot be traced by means of CH_2O-PLIF because of the very low CH_2O concentration in a lean premixed flame. However, Schlieren and OH* images are able to trace the flame contour.

The heat release rate curve shows three stages (Figure 43, bottom diagram): During the low-temperature combustion, only a low heat release is detected, followed by a peak of the heat release rate during the high-temperature reactions consuming the mixture of methane and pilot fuel. The first two phases overlap with high accuracy with the appearance and disappearance of the CH_2O signal, respectively. Following disappearance of CH_2O, a moderate heat release is detected, corresponding to premixed flame propagation.

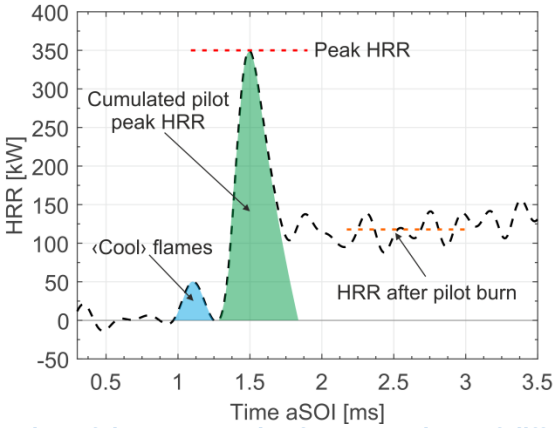

Figure 44: Graphic representation of the HRR metrics for comparison of different combustion variations. Black dashed curve shows typical HRR curve, red dashed lines demonstrate the detection of peak HRR and HRR after pilot burn. The green are represent the cumulated HRR during the pilot burning.

The HRR curve of dual-fuel combustion shows a characteristic shape for all variations investigated (bottom diagram in Figure 43). Based on this shape, following metrics have been defined to be able to compare combustion under different conditions (graphic representation Figure 44):

- Peak heat release rate:
  - Defines the highest pressure rise rate during the combustion event
- Amount of energy released in the pilot burn peak phase:
  - Defines how much of the entrained methane is burnt in the pilot burn phase. For further processing the value is normalized by the energy of the pilot fuel.
- HRR after pilot fuel is burned:
  - Defines the speed of combustion during the premixed flame propagation. Depends on the laminar flame speed and flame area initiated by the pilot fuel.

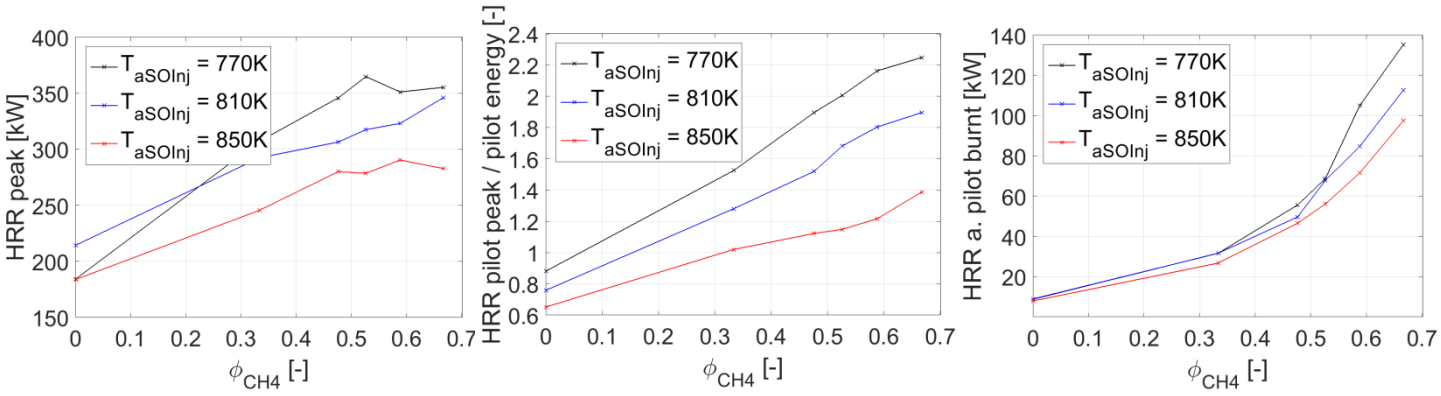

(a) Peak heat release rate (b) Energy released in the pilot combustion peak (c) HRR after pilot fuel burnt

Figure 45: Dual-fuel combustion metrics dependence on charge temperature and methane equivalence ratio.

The dependence of the dual-fuel HRR metrics on charge temperature and methane concentration is shown in Figure 46. The peak heat release rate tends to decrease with temperature and increases with methane concentration. The increase of peak HRR with decreasing temperature is explained by the longer ignition delay resulting in higher homogeneity of the pilot spray plume and less fuel-rich zones. The influence of methane concentration is explained by simultaneous combustion of pilot fuel and methane entrained in the pilot spray. Under conditions with longer ignition delay (decreased temperature), the entrainment can progress further and more of the entrained methane can be burnt,

as shown in the middle plot. The amount of burnt methane is proportional to the peak heat release rate, indicating that the duration of the pilot-fuel combustion remains roughly constant under the selected conditions. After the pilot fuel has been burnt, the heat release rate strongly increases with increasing methane concentration through an increasing laminar flame speed. The dependency on temperature has a secondary effect with the HRR after the pilot burn slightly increasing with decreasing temperature. The explanation is that the flame area initiated by the pilot spray increases due to the longer ignition delay under cold conditions.

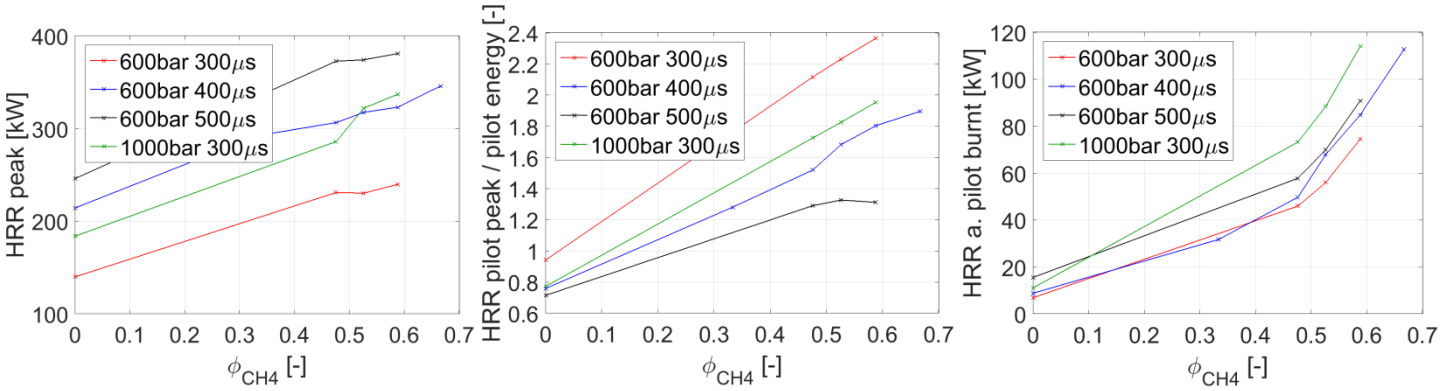

(a) Peak heat release rate (b) Energy released in the pilot combustion peak (c) HRR after pilot fuel burnt

Figure 46: Dual-fuel combustion metrics dependence on pilot injection strategy and methane equivalence ratio.

A comparison of the combustion metrics for different pilot injections and variation of methane equivalence ratio (Figure 46) shows that the amount of pilot fuel most strongly influences the peak heat release rate. The peak HRR increases with an increasing pilot fuel mass. This trend is expected to stabilize when the injection duration is comparable or longer than the ignition delay, which was not the case in the present study. On the other hand, the short injections and the high pressure injections are more efficient at burning the entrained methane as visible by comparison of the amount of energy released during the pilot HRR burning. The shortest injections release up to double of the heat carried by the pilot fuel indicating lean pilot fuel concentration at the time of ignition. The long pilot injections create mostly fuel rich conditions at the time of ignition and therefore do not permit complete combustion of the entrained methane. After the pilot fuel is burnt, the HRR depends on the turbulence introduced through the injection and on the flame area. Therefore, high pressure and long injections result in higher HRR.

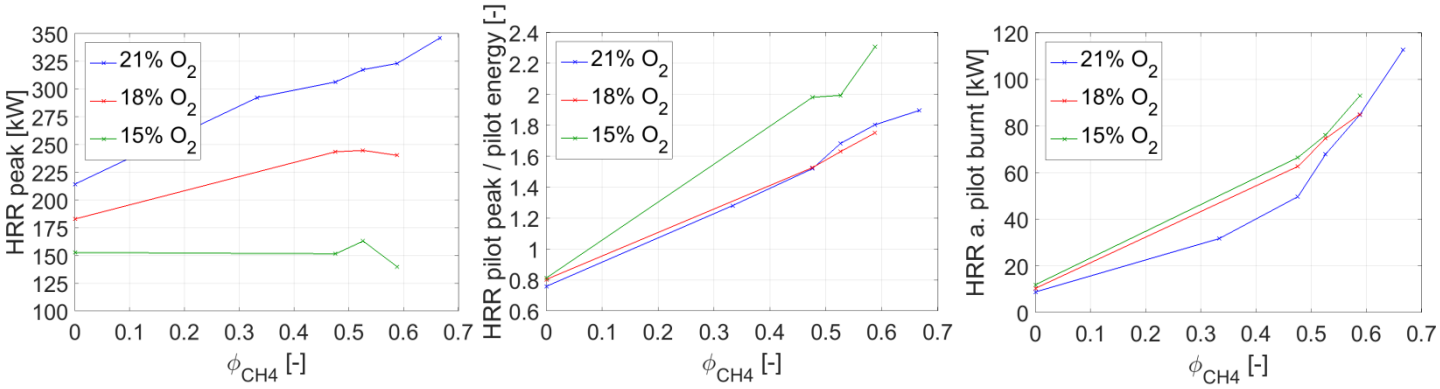

(a) Peak heat release rate (b) Energy released in the pilot combustion peak (c) HRR after pilot fuel burnt

Figure 47: Dual-fuel combustion metrics dependence on charge oxygen concentration and methane equivalence ratio.

In cases of reduced oxygen content, reactivity is additionally decreased (Figure 47), resulting in a considerable increase of the ignition delay. The peak HRR decreases with reduced oxygen content, and the addition of methane has a smaller influence on the peak HRR. The amount of heat released in the pilot burn event (b) does not change with addition of methane for 18% oxygen case and increases for 15% oxygen case when compared to the 21% O_2 case. Three influences contribute to this behavior: Decrease of reactivity through the decreased adiabatic flame temperature, leaning of the spray through the increased ignition delay and shift of the stoichiometric mixture fraction. The decrease of the peak HRR is explained by slower spreading of the flame trough the pilot fuel volume due to the lower adiabatic flame temperature and leaning of the spray. This results in the longer duration of the pilot fuel combustion and lower peak heat release rate. The amount of methane which can be burnt during the pilot fuel combustion is dependent of the local equivalence ratio at ignition. In the 18% O_2 case the decreased oxygen availability balances the leaning of the spray resulting in a similar level of methane burned during the pilot HRR as in the 21% O_2 case. In the 15% O_2 case the effect of spray leaning prevails over the decreased oxygen content leading to an increased amount of methane burnt during the peak HRR. The premixed combustion phase depends on both the flame area initiated through pilot flame kernel and on the laminar flame speed. With introduction of EGR the laminar flame speed decreases which is in EGR cases counterbalanced by the higher surface of the flame kernel due to the increased ignition delay. Therefore the EGR has a small influence of the HRR in the premixed flame phase.

With the wide measurement matrix of Campaign 3 many interesting trends have been observed along with the optical data that can aid the interpretation of the results. The processed data has been included in the database. Due to the wide measurement matrix, this data is especially useful for validation of the fast phenomenological 0D models used for control systems of dual-fuel engines

5.6. Soot detection

Soot and PAH (poly-aromatic hydrocarbons) as soot precursors fluoresce strongly upon excitation at 355 nm. This is commonly regarded as interference in the signal; however, it can be also used as a detection method for PAH. In combination with Schlieren imaging, CH_2O PLIF can be a good indicator of the PAH themselves.

The CH_2O-PLIF data has been complemented by DBI (diffuse back illumination) imaging and 1D spectral acquisition of soot luminosity in the Campaign 5. The experimental methodology selection has been based on the evaluation of the CH_2O PLIF data which show that around 50% of the conditions investigated in the Campaign 3 did not produce any soot. The rest of the conditions produced only low to moderate amounts of soot owing to the short pilot injections. Cyclic variability of soot formation, especially for low sooting conditions, is very high. Since the LII (laser induced incandescence), described in Section 4.1, is less appropriate for conditions with large cyclic variation (no axial symmetry, laser sheet might completely miss the soot cloud), a line of sight DBI technique has been used as for quantitative measurements of the soot amount. The results of this technique can be precisely quantified [36] and it has been adapted as a standard method for soot detection in the Engine Combustion Network.

In dual-fuel conditions the equivalence ratio distribution strongly changes due to the presence of methane. Therefore it is probable that soot will be formed and oxidized at different mixture fractions compared to pure Diesel operation. Therefore the information about soot temperature is a valuable input to understand the soot formation in dual-fuel combustion. This information has been provided by the 1D spectral acquisition of the soot luminosity acquired in parallel with the DBI imaging.

The experimental setup for simultaneous DBI and 1D-spectroscopy at the RCEM facility is sketched in Figure 48. The DBI setup closely resembles the recently proposed improved DBI setup of Westlye et. al.[22]. The diffuse back illumination was provided by directing the collimated output of the Cavilux laser diode on an engineered diffusor (RPC Photonics, 10° scattering cone angle) insuring homogeneous diffuse illumination across the whole RCEM window. On the detection side, the light from the RCEM combustion chamber was split using a dichroic mirror (50% reflection in the range of 300 nm – 550 nm and high transmission at other wavelengths). The Cavilux light emission at 690 nm was partially transmitted through the dichroic mirror and detected with a high speed camera equipped with a visible light photographic lens and a bandpass filter to block the soot luminosity (Sigma 105 mm f/2.8 lens, filter CWL 690 nm FWHM 10 nm). A part of the short wavelength band of the flame and soot light emission was reflected by the dichroic beamsplitter towards the spectrograph and projected on the spectrograph slit using an UV objective lens. An imaging spectrograph was used in order to enable 1D resolution along the slit. The spectrally separated light was detected with an intensified high-speed camera system. The wavelength range between 250 nm and 610 nm was acquired with a resolution of approximately 2-3 nm. The estimated detection limit of the DBI setup (based on the level of interference through Schlieren and camera noise) was KL = 0.04.

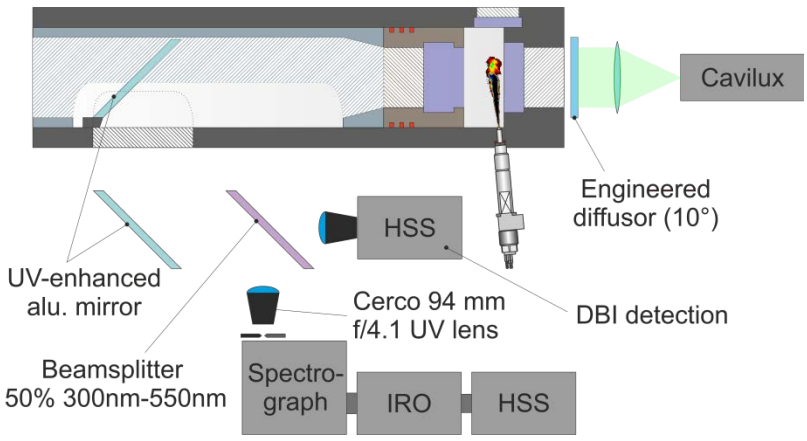

Figure 48: Experimental setup for simultaneous DBI and 1D-spectroscopic imaging at the RCEM.

The DBI image processing followed the methodology proposed by the Engine Combustion Network [37]. In order to remove the interference of the soot luminosity on the absorption detection, the camera

frame rate was set at twice the pulse rate of the Cavilux diffuse back-illumination. Therefore every second image was not illuminated by the light source and did therefore record only the soot black-body luminosity. An average of the preceding and following image was subtracted from each illuminated image. The image was normalized by the bright-field image (obtained from the five images of the series acquired before the SOI). Finally the KL factor was calculated based on the light absorption.

A comparison of all three soot detection methods is presented in Figure 49 for an averaged acquisition at the time instant of 1.3 ms after SOI. The 355 nm-PLIF image originates from the CH_2O-PLIF acquisition of Campaign 3. Spectroscopy and DBI were performed simultaneously in the Campaign 5. The 355 nm-PLIF images show consistent signals at the spray tip at a time instant of 0.5 ms after ignition. Commonly this is attributed to PAH, which can be excited with a wide range of UV and visible wavelengths. PAH are precursors of soot. The 355 nm-PLIF images agree qualitatively with the DBI images. The absolute scale of DBI, however, shows a very low absorption (KL-factor below 0.08). This is at the limit of detection of the DBI method, resulting in low signal-to-noise ratio because of Schlieren effects and camera noise. This demonstrates the very high sensitivity of the 355 nm-PLIF method on PAH what is advantageous for the detection of low soot levels, where DBI fails owing to its detection limits. Unfortunately, the 355 nm-PLIF methodology cannot be quantified to yield information about the absolute amount of soot.

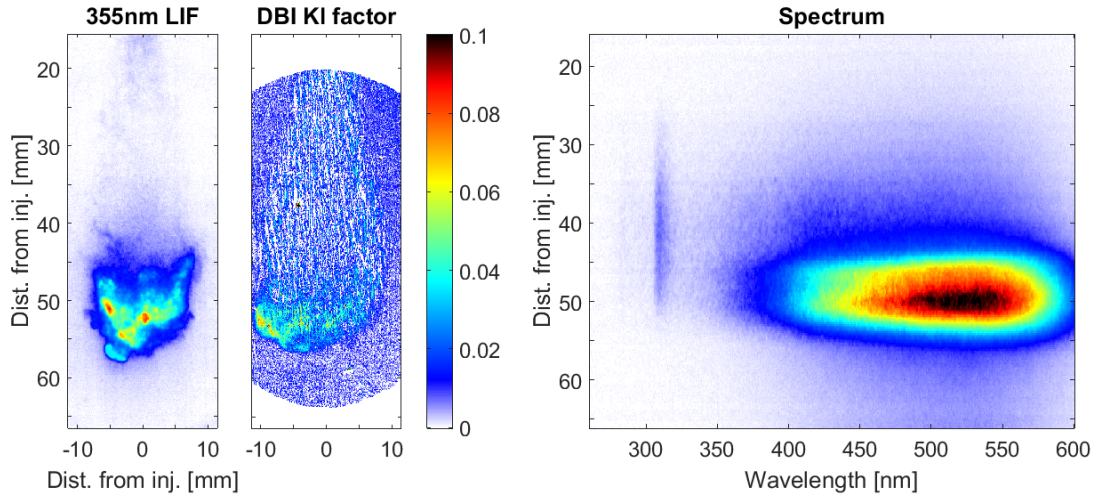

Figure 49: Comparison of three methods for soot detection: 355 nm-PLIF (left), DBI (middle) and 1D-spectroscopy (right). Conditions: T_{SOI} = 850 K, Φ_{CH4} = 0, pilot ET = 400 µs, P_{inj} = 600 bar. The images have been averaged over 10 repetitions at the time instant of 1.3 ms aSOI.

The 1-D spectroscopy spectrally resolves the flame emission and soot luminosity in one dimension along the fuel-injector axis. Soot is a gray body emitting at temperatures close the flame temperature. Most of the luminosity is expected in the NIR and visible wavelengths. Under hot conditions the soot luminosity can extend also towards the near UV region and, for example, cause interference with OH* acquisition. The spectrum in Figure 49 shows OH* chemiluminescence emission at around 310 nm. At longer wavelengths a bright cloud emitting from 350 nm up to 600 nm and beyond is visible attributed to thermal soot radiation. This emission is spectrally well separated from the OH* signal. Spatially the spectral region of soot luminosity is well aligned with the soot regions detected by the DBI and 355 nm-PLIF imaging methods.

The spectroscopic images were further processed to yield information about the soot temperature. The spectrum acquired by the setup depends on the quantum efficiency of the intensifier photocathode, vignetting effects of the relay optics coupling of the camera and intensifier, UV-lens transmission, grating and mirror efficiency of the spectrograph, and reflectivity of the beam-splitter dichroic mirror used to separate the DBI illumination light from the natural luminosity (Figure 50). Manufacturer data has been assumed for the quantum efficiency of all components except the beam-splitter optics. The spectral dependence of the beam-splitter reflectivity has been measured using a spectrograph and a broadband light source. The UV-lens manufacturer data for transmission at 400 nm has been used. The lens transmission at longer wavelengths has been estimated relative to the transmission at 400 nm using a setup with a spectrograph and a broadband light source in a similar fashion as the transmission of the beam-splitter has been determined. The efficiency of all elements has been multiplied together and used to correct the raw emission spectra detected by the camera.

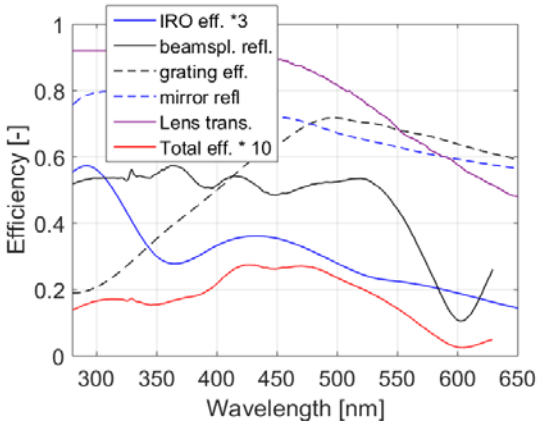

Figure 50: Optical and quantum efficiency of the most relevant elements in the 1D-spectroscopy optical pathway.

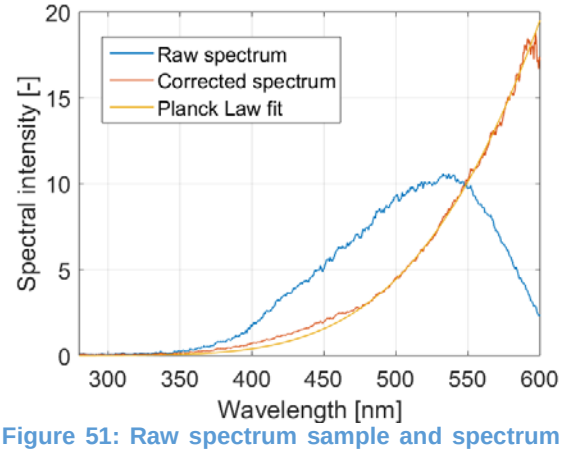

Figure 51: Raw spectrum sample and spectrum corrected for the system spectral efficiency compared to the Planck black-body emission spectrum with fitted temperature of 2830 K.

The correction approach of the raw emission spectra is demonstrated in Figure 51. The raw spectra are obtained by averaging over 10 repetitions of the experiment and over 10 pixels along the injector axis (resulting in 2 mm resolution along the injector axis). The raw spectra are corrected for the system efficiency by division of the raw spectra by the spectrally dependent system sensitivity. After the correction, the spectrum closely resembles a black-body radiation as long as soot radiation is the dominant source of luminosity. In order to estimate the soot temperature, a Planck-law curve is fitted to the corrected spectrum in the wavelength range of 470 nm – 585 nm. In this spectral range the contribution of interference through fluorescing species is expected to be smallest in the available spectral range. The result of the fitting procedure is a value for an apparent soot temperature at the spatial location of the spectrum. Figure 51 demonstrates the resulting Planck-law curve fit resulting in an estimated temperature of soot of T = 2180 K. The 95% confidence interval of the fitted temperature value is around +/-25 K. However, the absolute accuracy of this approach is questionable since the system has not been calibrated with a light source with a known emission spectrum. The system performance might deviate from the manufacturer data due to the component aging and manufacturing deviations. The aim of this study was, however, to observe the trends of soot temperature when changing from Diesel to dual-fuel operation. This can be captured well with the present experimental setup.

Due to the line-of-sight nature of the 1D-spectroscopy approach, the interpretation of the soot-temperature measurements has to be done with caution. The outer layers of the soot cloud usually have a higher temperature and shade the inner soot layers. Additionally the T^4 dependence of the black body luminosity biases the apparent temperature towards the temperature of the hottest soot parts along the line of sight. In order to study the extent of the influence of the outer soot layers on the detected soot temperature, Figure 52 shows the correlation of the apparent soot temperature and KL-value of a optical soot thickness at the same location along the injector axis for a variation of methane equivalence ratio. The soot temperature at locations with considerable soot optical thickness ranges between 2050 K and 2400 K. Higher soot temperatures were only detected at locations with very small amounts of soot, which is expected since the soot is expected to oxidize at close to stoichiometric conditions (stoichiometric flame temperature). However, the points detected in the dual-fuel case (Φ_{CH4} = 0.66) with a KL-value range of 0 – 0.2 and temperatures above 2500 K are not physical and indicate false detection. The detected light absorption might also be due to condensation of water on the windows giving false indication of soot. The detected black-body temperature might be due to water thermal radiation in the same wavelength range (further explained in Section 5.7).

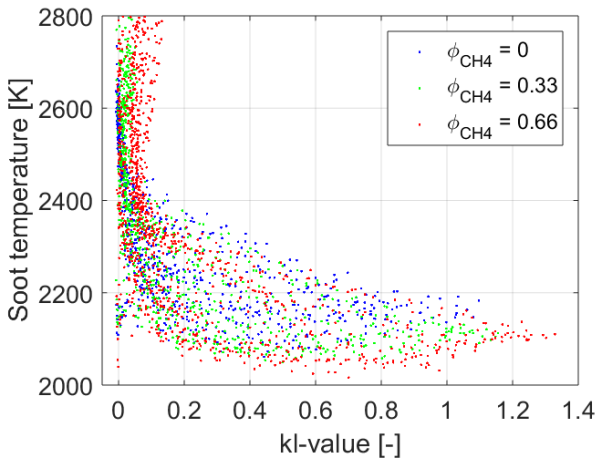

Figure 52: Correlation of the KL-value and apparent soot temperature for three different background equivalence ratios. Conditions: T_{SOI} = 850K, ET = 700µs

In the range of soot temperatures between 2000 K and 2400 K a considerable scatter along the temperature and KL-value axis has been detected. This is an indication that the detected apparent soot temperature does not only depend on the soot temperature of the outer layers of the soot cloud, which is expected to have approximately stoichiometric adiabatic flame temperature but also on the inner regions of soot which considerably contribute to the apparent soot temperature.

All spectra acquired in the measurement Campaign 5 were processed accordingly to the above described procedure together with the DBI acquisitions and pressure traces in order to yield HRR information. Since most of the points of measurement Campaign 3 produced negligible amount of soot (the case in Figure 49 is one of the most sooting case of Campaign 3), additional measurement points with longer injection duration (ET = 700 µs) have been included in the measurement matrix of Campaign 5 in order to study influence of methane on the sooting behavior of dual-fuel combustion. All spectroscopy measurements have been processed accordingly to the procedure described above and included in the experimental database along with the DBI measurements and HRR analysis based on the pressure traces. Main scientific results of the study are summarized below.

The analysis of the methane influence on the sooting behavior of dodecane spray has been assessed based on a comparison of cases with same ignition delay (simultaneous variation of methane concentration and temperature keeping the ignition delay constant) and comparison of cases with

methane variation (same temperature, variation of methane). The influence of methane at constant ignition delay offers a comparison of methane influence while keeping the pilot fuel distribution at the time of ignition unchanged. Figure 53 shows the evolution of average soot optical density for three cases with different background methane equivalence ratio (Φ_{CH4} = 0, 0.33, 0.66) and approximately the same ignition delay (T_{SOI} = 770 K, 810 K and 850 K, ignition delay in the range of 1.1 ms – 2 ms) for a longer injection with energizing time ET = 700 µs. Addition of methane shifts the stoichiometric equivalence ratio toward fuel jet boundary and reduces the temperature and oxygen availability in the core of the spray. This results in a significantly increased soot formation under dual-fuel operating conditions. The total amount of soot increases by a factor of 12 from Diesel case (770 K) to a dual-fuel case (850 K Φ_{CH4} = 0.66). Conditions more favorable for soot production result also in the earlier start of soot formation. A wider and longer shape of the dual-fuel soot cloud indicates that presence of methane widens the band of pilot-fuel equivalence ratio favorable for soot production. The location where the first soot starts to form is shifted further downstream of the injection in the dual-fuel cases as the ignition location also shifts downstream as presented in the Section 5.4. In Diesel cases the soot formation finishes soon after the first soot is formed and the soot cloud is transported further downstream where it oxidizes slowly. In the dual-fuel case the soot is formed also upstream of the location of the first soot production. An elongated soot cloud is formed reaching up to a distance of 35 mm from the injector. By the time of 1.8 ms aSOI the soot cloud reaches the edge of the RCEM window and a part of the soot cloud is not visible anymore. Therefore the present setup does not allow for observation of soot oxidation at the spray tip. It is visible, however, that the optical density of the soot does not decrease up to 2 ms after SOI in both cases with the presence of methane. This confirms the expectation of significantly reduced soot oxidation due to the lower availability of oxygen outside of the Diesel fuel jet.

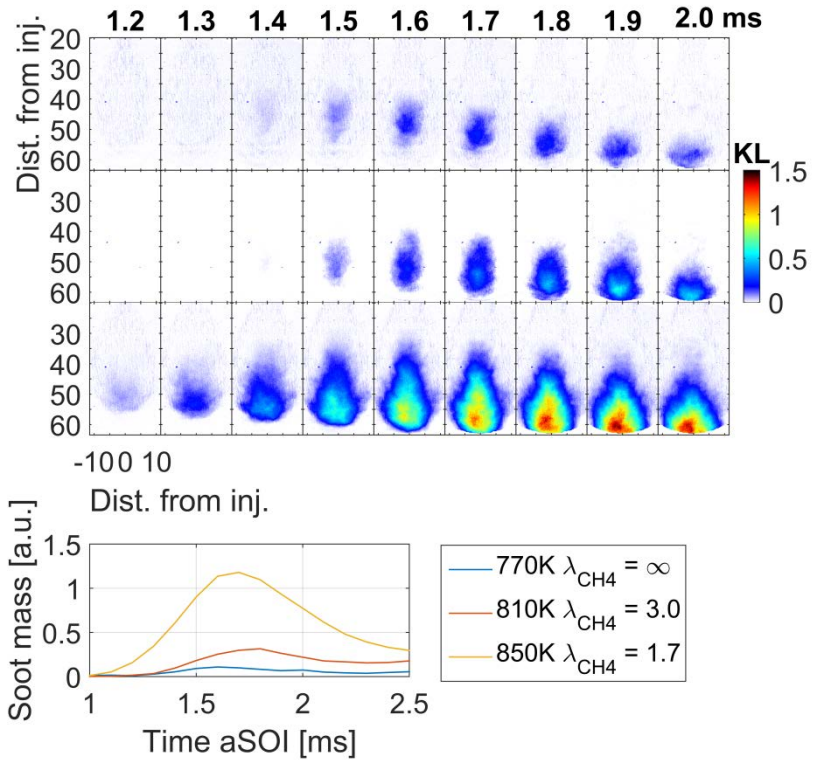

Figure 53: Evolution of soot cloud optical thickness for three cases with approximately the same ignition delay: 770K Φ_{CH4} = 0 (upper row), 810K Φ_{CH4} = 0.33 (middle row), 850K Φ_{CH4} = 0.66 (lower row). Pilot injection: ET = 700 µs, P_{inj} = 600 bar. The diagram at the bottom shows the evolution of the total soot mass in arbitrary units, extracted from the DBI images.

The evolution of the apparent soot temperature along the injector axis for the three cases with constant ignition delay is presented in Figure 54. For all cases the temperature range is between 2050 K and 2800 K. The regions with the highest soot density appear to have the lowest apparent temperature. As the soot cloud is transported away through spray convection it leans out and the apparent soot temperature slowly increases. Highest soot temperatures were detected in the wake of the soot cloud. This can be partially contributed to the soot oxidation due to the entrainment wave [30]. After the end of injection, however, this measurement is biased through the light emission of other species in the same spectral range. The region of soot oxidation at the spray tip remains invisible as it leaves the visible domain before the onset of soot oxidation.. Comparison of the three cases with same ignition delay indicates a colder soot-dense cloud in the dual-fuel case while the oxidation of soot in the cloud wake appears to take place at higher temperatures. A possible explanation is the higher adiabatic flame temperature due to the higher temperature of the unburnt mixture in the dual-fuel cases. Further analysis and comparison with CFD simulation is needed to fully understand the observed phenomena.

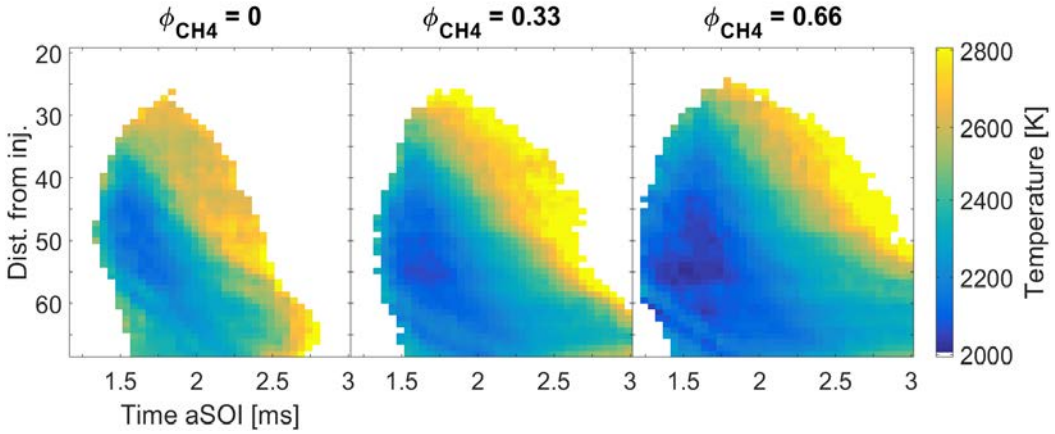

Figure 54: Evolution of the apparent line-of-sight soot temperature along the injector axis for three cases with approximately the same ignition delay.

A comparison of the soot KL-value distributions for a variation of background methane equivalence ratio at the same charge temperature is shown in Figure 55. Due to the methane influence on the ignition delay of the pilot fuel, both the pilot fuel equivalence ratio at the time of ignition and the availability of oxygen in the pilot-fuel plume change with this variation. The formation of soot is delayed trough addition of methane due to the decreased ignition delay and the highest soot concentrations were found later in the cycle. Overall, the addition of methane moderately increases the highest soot optical thickness. Similarly as in the case of methane variation at the constant ignition delay the first soot is formed at larger axial distance from the injector with the addition of methane. In the present configuration this is mostly due to the delayed ignition since the first soot appears to be formed at the spray tip. In all cases the soot formation shifts further to the injector nozzle as the injection proceeds, resulting in an elongated soot cloud. The closest distance between soot cloud and injector increases with the addition of methane. Since the injection ends at 1.2 ms aSOI, this was attributed to leaning of the jet wave through the entrainment wave. The soot oxidation at the jet wake proceeds in dual-fuel cases significantly slower than in the Diesel case due to the lower oxygen availability in the burnt premixed mixture. While the axial profile of the soot cloud strongly changes with the addition of methane the radial profile and width of the soot distribution close to the spray tip does not change considerably. This indicates that methane mostly influences the soot oxidation trough the lower availability of oxygen. The soot production seems to be mostly influenced by the local equivalence ratio of the Diesel surrogate fuel and less by the availability of oxygen. This has been attributed to the absence of C-C bonds in methane what renders it much less prone to sooting combustion. Further investigations by means of PSR reactor simulations by 3D-CFD simulations are necessary to fully explain this phenomenon.

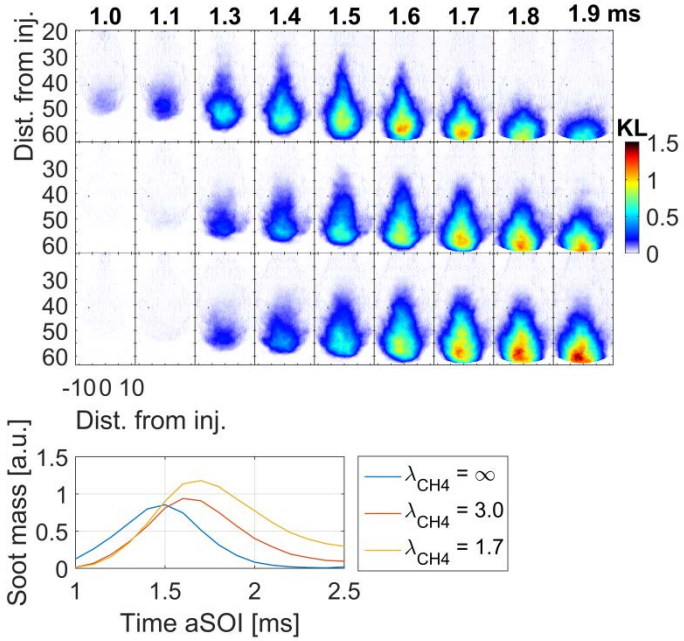

Figure 55: Evolution of soot cloud optical thickness for variation of the background methane equivalence ratio (T_{SOI} = 850K): Φ_{CH4} = 0 (upper row), Φ_{CH4} = 0.33 (middle row), Φ_{CH4} = 0.66 (lower row). Pilot injection: ET = 700 µs, P_{inj} = 600 bar. Bottom diagram shows the evolution of the total soot mass in arbitrary units, extracted from the DBI images.

The apparent soot temperature evolution for the variation of the background methane equivalence ratio is presented in Figure 56. A significantly lower temperature of the dense soot cloud has been measured in the dual-fuel case. This is a result of the large part of the soot cloud located in the fuel-rich region at the spray tip, where in the presence of methane the adiabatic flame temperature decreases due to the overall increased equivalence ratio. At the wake of the fuel jet a significantly slower oxidation of soot was observed when methane has been added to the air charge while in the Diesel case the soot cloud completely leaved the observable domain by the time of 2.7 ms aSOI. In dual-fuel cases generally higher temperatures have been observed. The oxidation proceeds significantly slower.

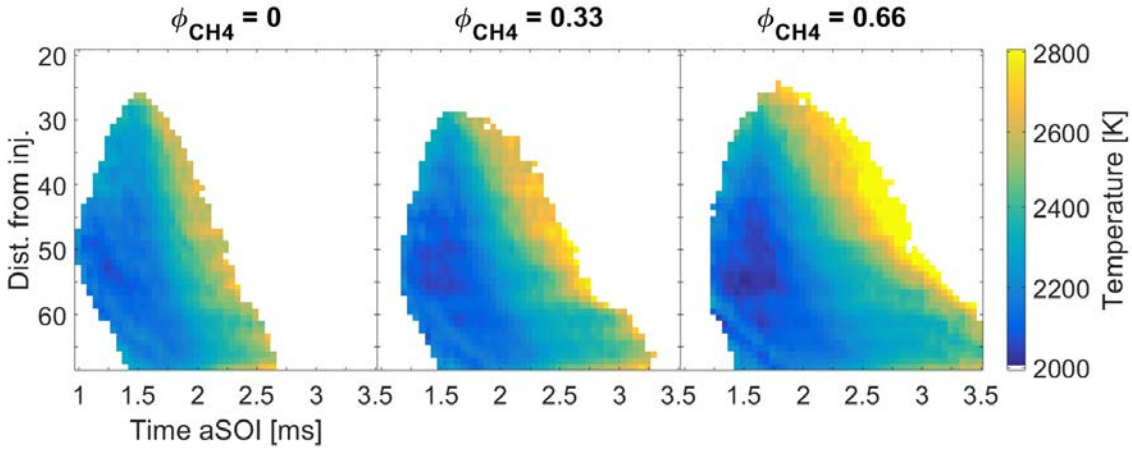

Figure 56: Evolution of the apparent line-of-sight soot temperature along the injector axis for a variation of background methane equivalence ratio. Conditions: T_{SOI} = 850 K, ET = 700 µs, P_{inj} = 600 bar.

For long injections in general an increased soot amount and slower oxidation of soot have been observed in the dual-fuel cases compared to the Diesel case. Figure 57 shows the evolution of the soot quantity for three different injection durations and a sweep of methane equivalence ratio. Please note that the soot amount for 400 µs and 500 µs injection ET is multiplied by a factor of 10 and 5, respectively. For all injection durations the soot formation is delayed in the presence of methane due to the increased ignition delay. Contrary to the trend for a long injection, the 500 µs ET injection shows the smallest soot amount for the medium equivalence ratio of methane. The shortest injection shows a detectable soot amount only in the Diesel case while both dual-fuel cases show no soot amount above the noise level of the DBI imaging. This is explained by the influence of methane on the ignition delay. In case of a short injection, an additional ignition delay leads to a further drop of the equivalence ratio of the pilot fuel, eventually falling below the threshold of soot production. The addition of methane exactly provides this increase in ignition delay. . The apparent increase of the soot amount late in the cycle is an artefact caused by water condensation on the RCEM windows.

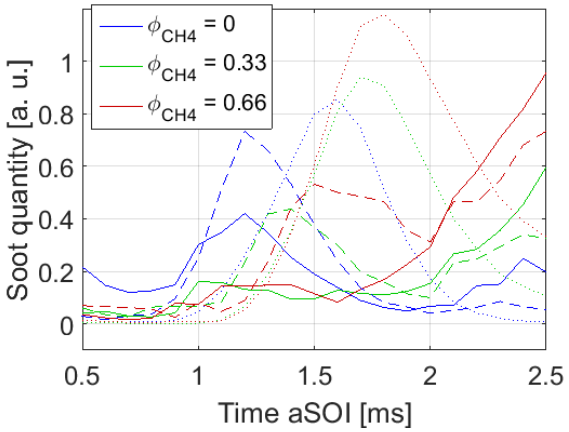

Figure 57: Temporal evolution of the soot quantity for a variation of the background equivalence ratio for three different injection durations: ET = 400 µs (full line, quantity multiplied by 10), ET = 500 µs (dashed line, quantity multiplied by 5), ET = 700 µs (dotted line).

5.7. Dual-fuel flame luminosity

The study of the dual-fuel flame luminosity has been motivated by an unusual evolution of the OH* chemiluminescence signal in dual-fuel cases. Figure 58 shows the HRR rate compared to the image-averaged OH* chemiluminescence for a sweep of background methane equivalence ratio. The introduction of methane leads to an increased peak HRR as already discussed in the Section 5.5. This has been attributed to the longer ignition delay and simultaneous pilot fuel and entrained methane burning. In the premixed flame propagation phase a higher methane concentration results in higher HRR due to an increased laminar flame speed. The OH* chemiluminescence signal appears to be decoupled from the HRR. Peak OH* chemiluminescence signals in dual-fuel cases have been detected during the premixed flame propagation stage 1-2 ms after the pilot fuel combustion. Higher OH* signals are observed for higher methane background concentrations. This behaviour has also been observed by Schlatter et. al [25] for heptane pilot fuel. It could not be determined whether this signal originates from OH*, broadband CO_2* chemiluminescence or possibly soot black-body radiation.

The aim of this study was to identify the contributions of different species to the signal detected by the OH* camera and to characterize the spectral footprint of the dual-fuel combustion in the relation to the Diesel-surrogate combustion. The 1D-spectroscopy setup described above in the Section 5.6 (Figure 48) has been used for this study as well.

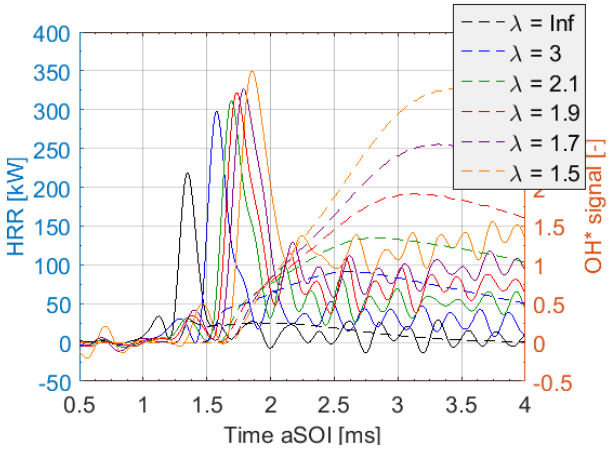

Figure 58: HRR and image-averaged OH* chemiluminescence signal evolution for a variation of the background methane equivalence ratio. Conditions: T_{SOI} = 810 K. Pilot injection: P_{inj} = 600 bar ET = 400 µs.

The spectrograph images were transformed into a series of raw spectra resolved by averaging 10 pixel bands along the injector axis. The resulting spatial resolution was approximately 1 mm along the injector axis. The spectral resolution was approximately 2-3 nm and was limited by the slit width setting of the spectrograph which was set in the range of 40-100 µm in order to collect sufficient amount of light to enable high-speed time resolved recording. Figure 59 demonstrates the spectrum processing procedure which closely follows the procedure proposed by Nafajabadi et. al. [38]. First, the raw spectra were corrected for the system spectral sensitivity (Figure 50). The corrected spectra show well distinguishable peaks at around 310 nm, 430 nm and 510 nm on a pedestal of broadband luminosity. A spline fit with a long stance has been used to approximate the spectrum of the background luminosity. In the second step the approximated broadband luminosity has been subtracted from the spectrum. The intensity of the remaining peaks in the range of 305-320 nm, 423-437 nm and 510-520 nm has been integrated and assigned as the intensity of OH*, CH* and C_2* chemiluminescence, respectively.

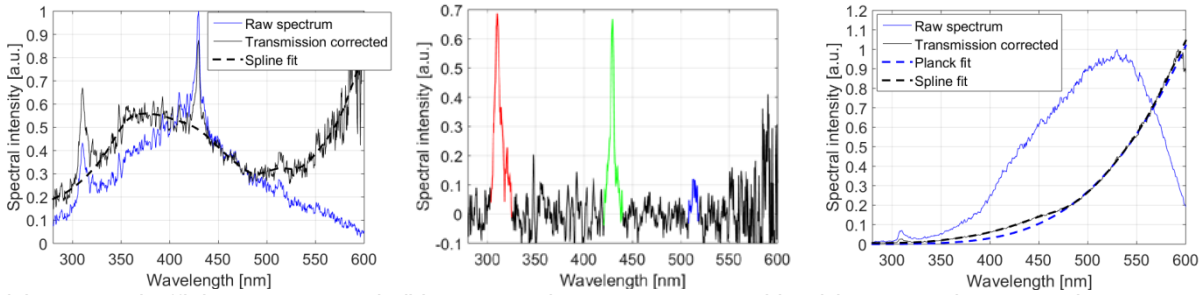

(a) Raw and efficiency corrected non-sooting flame spectrum and a spline fit

(b) Corrected spectrum with subtracted spline fit of the broadband luminosity

(c) Raw and corrected spectrum of a sooting case with the fitted Planck spectrum and broadband spline fit.

Figure 59: 1D-spectroscopy processing approach: (a) Correction of raw spectra for the system sensitivity and spline fitting of the broadband spectrum. (b) Corrected spectrum with subtracted broadband emission. Wavelength ranges for detection of OH*, CH* and C2* are marked in color. (c) Processing approach for a sooting case with Planck-law fitting.

In sooting cases an additional processing step had to be performed to separate the broadband chemiluminescence from the soot blackbody luminosity. For this purpose, first the Planck-law for the

blackbody luminosity has been fitted to the corrected spectrum in the wavelength range between 470-590 nm. The blackbody spectrum was subtracted subsequently. A spline has been fitted to the remaining signal to estimate the broadband luminescence. A criterion whether the spectrum indicates sooting or not was set based on the relative spectral intensity at 550 nm compared to the intensity at 400 nm. A threshold on the ratio of the intensities I (550 nm) / I (400 nm) > 2 has been set empirically based on the analysis of wide range of conditions. Unfortunately, this method cannot distinguish between the soot black body luminosity and the broadband luminosity in the upper wavelength range. This results in an underestimation of the broadband luminosity in the sooting cases since all light emission in the range from 470-590 nm is considered to originate from blackbody luminosity. In the wavelength range of interest (300-450 nm) this error is considerably smaller and does not change significantly the results.

The temporal evolution of the spectral emission of a non-sooting Diesel and duel-fuel combustion case is presented in Figure 60. In both cases, at the time of ignition, the first luminosity is detected across the complete spectral range of the combustion. Besides the OH* chemiluminescence emission in the range from 305 nm-320 nm also two bands of broadband luminosity are visible: A band extending from approximately 300 nm-500 nm and a band extending from 500 nm towards longer wavelengths. The first band has been attributed to the emission of electronically excited CO_2, which originates from the oxidation reaction of CO [38-42]. The emission of the second band persist longer than the emissions of CO_2*and OH*. In the literature this emission is commonly attributed to the overlapping H_2O vibration-rotation bands (500-850 nm), and the NO-O continuum (400-800 nm) [42]. Late in some of the dual-fuel cycles an additional emission at 589 nm was detected and was attributed to sodium D-line emission. The sodium is believed to originate from the lubrication agent used in the RCEM. The emission of CH* is only visible in the very early phase of combustion; it is too weak to be visible on **Fehler! Verweisquelle konnte nicht gefunden werden.**. In the following the analysis focuses on the dependence of OH*, CH*, C_2*, and broadband emission of CO_2* (350 – 400 nm range) on the background equivalence ratio, charge temperature and pilot injection duration. A very large difference in the intensity of Diesel and dual-fuel case required different color scale representation (Diesel case intensity multiplied by a factor of 10). Besides the difference in intensity no significant difference in the spectral footprint of both cases is detectable.

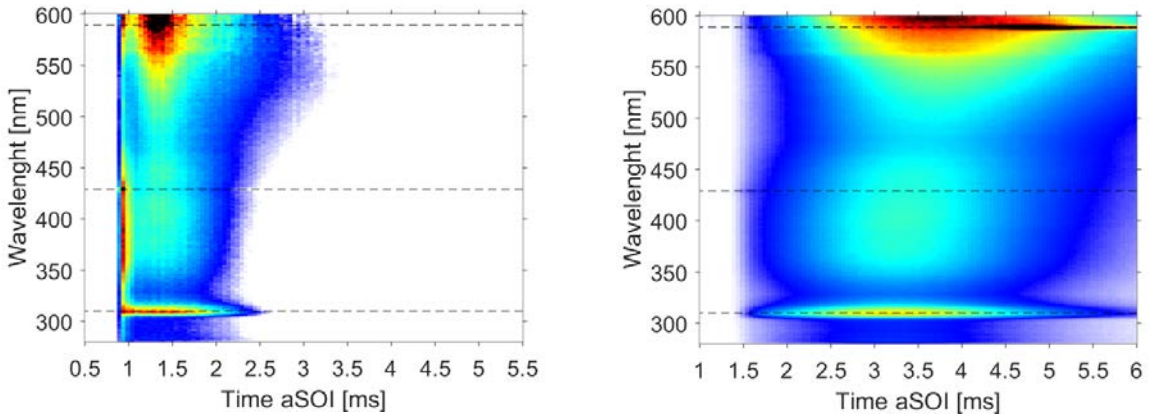

(a) Φ_{CH4} = 0 (b) Φ_{CH4} = 0.66

Figure 60: Temporal evolution of an injector-axis averaged spectrum of dual-fuel combustion. Conditions: TSOI = 810K. Pilot injection: Pinj = 600 bar ET = 400 µs. Intensity of Diesel combustion case is multiplied by a factor of 10 to utilize the complete range color representation.

A comparison of the combustion spectral footprint for a variation of methane equivalence ratio is presented in Figure 61. Temporally resolved intensity of broadband, OH*, CH* and C_2* chemiluminescence along the injector axis is presented. A comparison of the OH* and broadband chemiluminescence (CO_2*) intensity shows only minor differences between the signal distribution of both species. Only during the pilot fuel burn a broadband chemiluminescence shows higher intensity that the OH*. This confirms that the OH* chemiluminescence imaging is representative of the OH* signal under the conditions of interest regardless of the fact that 20-50% of the signal passing the bandpass filter originates from the broadband chemiluminescence emission. The temporal evolution of the OH* detected by the OH* imaging and 1D-spectroscopy is very similar, with a significantly increased signal in the dual-fuel combustion cases at late times aSOI. A CH* signal is only present during the pilot burning phase and is not detectable during the premixed flame propagation phase. The duration of the CH* signal appears to be a good indicator of the pilot fuel combustion duration and can aid the detection of the ignition delay. This might be especially useful in the dual-fuel cases where a very slow rise of the OH* signal after the ignition has been observed. This could lead to an ambiguity in the detection of the ignition delay. In such cases the CH* signal offers a better measure for the detection of the ignition delay. The signal of the C_2* is very weak and cannot be detected reliably by the present signal processing. Based on Figure 61 no conclusion on the C_2* signal evolution in dual-fuel cases could be made. A better method for subtraction of the background luminosity is needed. In the late phase of combustion also the detection of CH* might fail, leading to apparently negative values of the signal. For the evaluation in the early phase, the present evaluation works sufficiently well to extract the duration of the CH* luminosity.

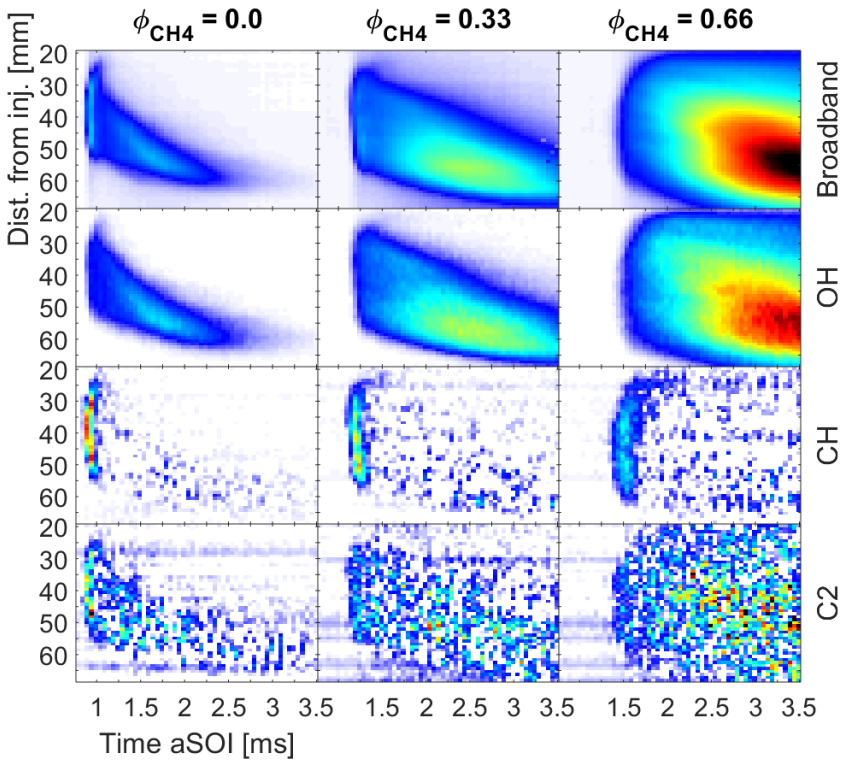

Figure 61: Temporally and spatially resolved intensity of the broadband, OH*, CH* and C_2* chemiluminescence for a variation of the background methane equivalence ratio. Conditions: T_{SOI} = 810 K. Pilot Injection: P_{inj} = 600 bar ET = 400 µs

The evolution of CH* and OH* intensity for a wide variation of background methane equivalence ratio, charge temperature, injection duration, and EGR is presented in Figure 62. The duration of the CH*

signal is a good measure for the duration of the pilot fuel burning phase which seems to increase with the addition of methane into the background mixture. Decreasing the temperature also seems to increase the duration of the pilot burning phase. The injection duration, however, does not show a significant influence. EGR cases without presence of methane do not show considerable change in the duration of the pilot fuel combustion while a combination of EGR and methane considerably increases the duration of the pilot fuel burning. The OH* signal evolution shows considerable increase of the signal with the addition of methane for all variations presented. This influence is especially strong under cold conditions and for short injections where the addition of methane prevents leaning of the pilot fuel. Therefore the regions with high temperatures take larger volumes and persist longer, leading to a higher OH* emission. An addition of EGR, here simulated by a reduction in O_2 content, reduces considerably the OH* signal due to the strongly decreased adiabatic flame temperature. The addition of methane has a moderate influence on the OH* intensity.

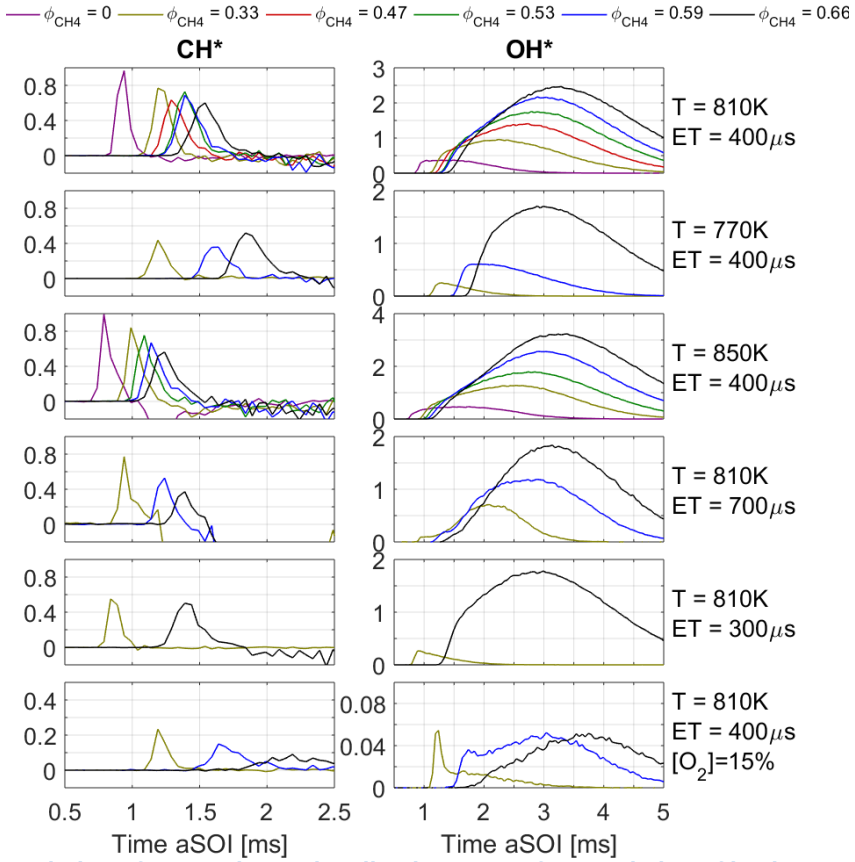

Figure 62: Evolution of CH* and CH* chemiluminescence for a variation of background methane equivalence ratios, for a range of charge temperature, injection duration, and EGR.

In summary, the study of the spectral footprint of the dual-fuel combustion revealed that 50%-80% of the contribution to the OH* imaging signal definitely originates from OH*. The remainder of the signal originates from the broadband chemiluminescence of CO_2* which shows similar temporal and spatial evolution as OH*. Therefore OH* imaging signal is a representative for the OH* emission from dual-fuel flames. The emission from the CH* radical is a good tracer for the combustion of the pilot fuel and can complement CH_2O-LIF imaging especially for cases where PLIF imaging suffers from the large interference of soot precursors like PAH.

6. Generation of reference data for CFD validation

The structure of the reference data database for CFD validation has been determined in tight cooperation with CFD collaborators from LAV ETHZ. The used combination of laser based and passive diagnostics techniques insures well time resolved data from passive techniques as well as high fidelity data from the laser based techniques. All measurement results of the project have been processed accordingly and included into the database. Besides the database also the raw information is available together with the documentation of the measurement approach if in the future further information should be extracted from the measurements.

Presently the database is available on request to the CFD partners. Based on the large interest of national and international groups from the field, activities were initiated to make the database publicly accessible and also invite other groups to provide their experimental results. Contents of the database are summarized below:

Mixture formation

The present database contains the following information:

- Quantitative pilot fuel vapor concentration
- Time resolved (80 kHz) spray penetration and spray contour
- Spray liquid length
- Cyclic variability of above parameters

The quantitative pilot fuel vapor concentration data is based on high-speed tracer-PLIF acquisitions recorded at 10 kHz frame rate. The processing methodology accounts for the temperature dependence of the tracer fluorescence yield and the evaporative cooling of the mixture charge due to fuel evaporation. The estimated absolute accuracy of the data is +/-20%. The relative precision of the fuel-distribution in the spray is estimated to be around 5% based on the noise level of the images and sensitivity of the tracer fluorescence yield on temperature.
Schlieren imaging under non-reactive and reactive conditions is used to provide highly time resolved (80 kHz frame rate) data spray penetration and spray contour. A special processing routine has been developed. The routine is able to separate the spray Schlieren signal from the squish zone related Schlieren signal, background noise, and window dirt. Based on this processing, spray contour and penetration data has been generated. This data is useful for initial tuning of CFD spray models since it offers a straightforward first estimate of model performance.

Mie scattering data provides information of the liquid spray penetration. This data will be used for validation of spray breakup models.

Ignition and flame propagation

The present database contains following information:

- High speed CH_2O PLIF data (10 kHz):
  - Total CH_2O PLIF signal
  - Low temperature ignition location and ignition delay
  - Contours of regions which have undergone low temperature ignition
- High speed OH* chemiluminescence data:
  - Ignition delay and ignition location
  - Flame area and flame penetration
  - Total OH* chemiluminescence luminosity
- Schlieren imaging data:
  - Ignition location and ignition delay
  - Flame contours

  - Flame area and flame penetration
- Thermodynamic analysis:
  - Heat release rate

High-speed CH_2O PLIF data has been used to provide information on the low temperature ignition stages, which is very important for the validation of chemical mechanism performance. It can be used also to validate model in terms of turbulence-chemistry interaction.

Simultaneously acquired passive OH* chemiluminescence imaging data was used to provide information on the high temperature ignition and flame propagation stages. The data was processed using thresholding techniques and will serve to validate chemical kinetics models used in the modeling. Furthermore, information of flame spreading through the pilot spray and transition to premixed flame propagation is available.

The thermodynamic analysis of the data has been performed using established LAV ETHZ software WEG. The value of this data is to provide validation of the overall CFD modelling performance. Additionally, this data can serve for validation of 0D phenomenological models and virtual sensors.

Soot formation and distribution

The combustion under conditions used was very mildly sooting, which is one of the advantages of the used combustion facilities. Soot and its precursors (PAH) are the main source of interferences in CH_2O PLIF acquisitions. The data from the CH_2O-PLIF acquisitions is already included in the experimental database.

The DBI and 1D-spectroscopy data of the measurement Campaign 5 has also been processed according to the procedure described in Section 5.6. The database on the formation of soot contains the following information:

- High-speed DBI images:
  - Total soot amount in the observable domain
  - 2D line-of-sight integrated soot optical thickness (kl)
- High-speed 1D-spectrometry:
  - 1D and temporally resolved apparent soot temperature

7. Publications and information dissemination

The information dissemination during the project took place mostly through oral presentations and personal discussions with the experimental, CFD and 0D-modelling partners in the framework of collaborating institutions. The methodology development and measurement results have been documented by the project reports and internal documents to serve the knowledge transfer for the future projects. In collaboration with CFD partners the structure of a database for purposes of CFD simulation validation has been established. All experimental results have been processed and are presently available upon request.

During duration of the project the following conference contributions provided the dissemination of the information:

- C. Barro, A. Srna, D. Sakellarakis, S. Pandurangi, W. Vera-Tudela, D. Farrace, Y. M. Wright, K. Boulouchos: *Dual fuel combustion for IC engines*, Verbrennungstagung Schweiz 2017, Zürich,

07.09.2017

- A. Srna, R. Bombach, G. Bruneaux, K. Herrmann, P. Jansohn, K. Boulouchos: *Experimental study of pilot-fuel ignition mechanisms under dual-fuel engine relevant conditions*, invited talk at the 39th IEA Combustion Task Leader Meeting, 19.06.2017, Baiona, Spain
- A. Srna: *Experimental investigation of Diesel surrogate pilot spray combustion in lean-premixed methane atmosphere*, invited seminar lecture at IFP New Energy, Rueil Malmaison, France, 05.12.2016
- A. Srna: *Experimental investigation of Diesel surrogate pilot spray combustion in lean-premixed methane atmosphere*, seminar lecture in the ETH Aerothermochemistry and combustion systems laboratory seminar series, 31.10.2016
- A. Srna, R. Bombach, A. Denisov, D. Wüthrich, K. Herrmann, *Two-color LIF fuel spray vapor temperature imaging,* poster contribution, Verbrennungstagung Schweiz 2015, Zürich, 09.09.2015
- A. Srna: *Laser-based optical diagnostic techniques for investigation of Diesel- and Dual-Fuel combustion processes,* seminar lecture in the PSI Combustion Research Laboratory seminar series, 24.06.2015

Following the successful completion of project the scientific highlights will be published in peer-reviewed journal and conference proceedings. In addition to the already presented information the following publications are foreseen and in preparation:

- A. Srna, R. Bombach, G. Bruneaux, K. Herrmann, K. Boulouchos: *Understanding the ignition mechanisms of dodecane pilot-spray in methane-air mixtures under engine relevant conditions,* in preparation for Combustion and Flame / Proceedings of the Combustion institute
- A. Srna, R. Bombach, G. Bruneaux, K. Herrmann, K. Boulouchos: *Experimental investigation of sooting behavior of dodecane fuel-spray under dual-fuel engine relevant conditions*, in preparation for SAE Congress 2018
- A. Srna et. al., *Transition between the pilot fuel ignition and premixed flame propagation in a dual-fuel engine combustion process,* in preparation for the International Journal of Engine Research.

8. National and international collaboration

The project is closely related to the CCEM project "SCHE-Dual" with the partners ETH-LAV, FHNW, and PSI. In the framework of this cooperation – in particular between ETH-LAV and PSI – state-of-the-art optical measurement techniques and complementing laser-based techniques will be applied at the nominally identical high pressure/high temperature cell (HDTZ) experimental test facilities at ETH and PSI.

In 2015, a new set of special injector nozzles has been acquired in cooperation of LAV and PSI, since the original set showed errors in manufacturing which rendered injector behavior outside the specifications to produce state-of-the-art relevant measurements. The new set of injectors (nozzle diameter: 0.100, 0.120, 0.180 and 0.240 mm, three independent sets) has been successfully characterized (ETH). Results show that the new injector set fulfills all specifications. The new nozzles have already been successfully applied in 2016 for delivering pilot fuel in the present project for dual-fuel combustion research.

The reference data for CFD validations, generated in cooperation of PSI and ETH-LAV, will be used at ETH-LAV with the scope to validate the numerical framework regarding the in-cylinder fuel distribution and combustion evolution. The high-fidelity of the data also permits making the database publicly available to other simulation groups worldwide. Interest from Aalto University and University of Southampton has been expressed to date.

The dual-fuel combustion setup, developed in the framework of the present project, has been used also for initial investigations of the FVV (Forschungsvereinigung Verbrennungskraftmaschinen) funded project 'Dieselverbrennung auf homogenem Gasgemisch'. The project aims at investigations of a highly flexible 'dual-fuel' combustion engine, where proportions of natural gas and Diesel fuel consumed can be varied over a broad range.

High fidelity experimental results acquired in the framework of this project attracted high interest from national (LAV ETHZ, Win G&D, Vir2Sense) and international collaborators (IFPen Paris, Cambridge University, Aalto University, University of Southampton). In 2017, the high-speed CH_2O PLIF methodology, developed in the framework of this project, is scheduled to be applied at Win G&D Spray Combustion Chamber to study the low-temperature ignition stages in two-stroke marine engine relevant sprays. Methodology is sufficiently flexible that it can be also applied to other combustion concepts. .

In the framework of the dissertation of A. Srna, Dr. G. Bruneaux from IFPen Paris will take the role of the external dissertation examiner.

9. Conclusions and outlook

Following the successful completion of project the scientific highlights will be published in high-impact peer-reviewed journals. Further impact of the work is expected trough the new possibilities of collaboration based on the experimental database which has been established in the framework of the project. It is foreseen that the database will made openly accessible to enable collaboration of all interested partners both form the experimental and CFD community.

The experimental methodology developed in the project and the experience with application of the advanced laser-based methodology to challenging engine-relevant conditions has been thoroughly documented and can be readily applied to study different combustion processed as well as to serve further investigations of the dual-fuel combustion process. In the present project the limitations of the RCEM limited the experimental conditions to moderate pressures and methane equivalence ratios. The absence of turbulence enabled us to study the ignition process more fundamentally that this would be possible under conditions with higher turbulence. On the other hand the absence of turbulence resulted in slow flame propagation in the premixed flame phase, which is not representative of the engine combustion. The newly developed Flex-Oecos test-rig of ETH Zürich will overcome these disadvantages.

As possibilities for future research on the dual-fuel combustion, investigations under turbulent, i.e. more engine-like conditions should offer further insight into this combustion process. The experimental methodology itself, as used in the present project, is readily available to be applied to turbulent conditions. Further interesting topics include investigations of alternative pilot fuels (biogenic/oxygenated) which would offer potential to further reduce the engine pollutant emissions. Feasibility and interaction of these fuels with methane have to be investigated. Furthermore a comparison of the dual-fuel operation with different premixed fuels would offer a very interesting comparison of interference of the premixed fuel with the pilot fuel autoignition.

References:

[1] Chojnacki KT, Feikema DA. Exciplex fluorescence imaging for liquid mixing studies. Applied Optics. 1998;37:4034-8.
[2] Hale SJ, Melton LA. Absolute Quantum Yields for Exciplex Fluorescence. Appl Spectrosc. 1990;44:101-5.
[3] Herfatmanesh MR, Attar MA, Zhao H. Simultaneous imaging of diesel spray atomisation and evaporation processes in a single-cylinder CR diesel engine. Exp Therm Fluid Sci. 2013;50:10-20.

[4] Kim T, Ghandhi JB. Quantitative vapor phase exciplex fluorescence measurements at high ambient temperature and pressure. KSME International Journal. 2003;17:157-67.
[5] Rogler P, Grzeszik R, Arndt S, Aigner M. 3D analysis of vapor and liquid phase of GDI injectors using laser induced exciplex fluorescence tomography in a high pressure/high temperature spray chamber. SAE Technical Papers. 2007;2007-01-1827.
[6] Rotunno AA, Winter M, Dobbs GM, Melton LA. Direct Calibration Procedures for Exciplex-Based Vapor/Liquid Visualization of Fuel Sprays. Combustion Science and Technology. 1990;71:247-61.
[7] Senda J, Kanda T, Kobayashi M, Fujimoto H. Quantitative Analysis of Fuel Vapor Concentration in Diesel Spray by Exciplex Fluorescence Method. SAE Technical Papers Series. 1997;970796.
[8] Su W, Sun T, Guo H, Mao L, Xie T. Quantitative study of concentration and temperature of a diesel spray by using planar laser induced exciplex fluorescence technique. SAE International Journal of Engines. 2010;3:717-32.
[9] Desantes JM, Pastor JV, Pastor JM, Juliá JE. Limitations on the use of the planar laser induced exciplex fluorescence technique in diesel sprays. Fuel. 2005;84:2301-15.
[10] Kim T, Beckman MS, Farrell PV, Ghandhi JB. Evaporating Spray Concentration Measurementsfrom Small and Medium Bore Diesel Injectors. SAE International; 2002.
[11] Gessenhardt C, Schulz C, Kaiser SA. Endoscopic temperature imaging in a four-cylinder IC engine via two-color toluene fluorescence. Proceedings of the Combustion Institute. 2015;35:3697-705.
[12] Peterson B, Baum E, Böhm B, Sick V, Dreizler A. High-speed PIV and LIF imaging of temperature stratification in an internal combustion engine. Proceedings of the Combustion Institute. 2013;34:3653-60.
[13] Peterson B, Baum E, Böhm B, Sick V, Dreizler A. Evaluation of toluene LIF thermometry detection strategies applied in an internal combustion engine. Applied Physics B: Lasers and Optics. 2014;117:151-75.
[14] Peterson B, Baum E, Böhm B, Sick V, Dreizler A. Spray-induced temperature stratification dynamics in a gasoline direct-injection engine. Proceedings of the Combustion Institute. 2015;35:2923-31.
[15] Trost J, Zigan L, Leipertz A, Sahoo D, Miles PC. Characterization of four potential laser-induced fluorescence tracers for diesel engine applications. Applied Optics. 2013;52:8001-7.
[16] Zegers RPC, Yu M, Bekdemir C, Dam NJ, Luijten CCM, De Goey LPH. Temperature measurements of the gas-phase during surrogate diesel injection using two-color toluene LIF. Applied Physics B: Lasers and Optics. 2013;112:7-23.
[17] Tea G, Bruneaux G, Kashdan JT, Schulz C. Unburned gas temperature measurements in a surrogate Diesel jet via two-color toluene-LIF imaging. Proceedings of the Combustion Institute. 2011;33:783-90.
[18] Donkerbroek AJ, van Vliet AP, Somers LMT, Frijters PJM, Klein-Douwel RJH, Dam NJ, et al. Time- and space-resolved quantitative LIF measurements of formaldehyde in a heavy-duty diesel engine. Combustion and Flame. 2010;157:155-66.
[19] Bakker PC, Maes N, Dam N. The potential of on- and off-resonant formaldehyde imaging combined with bootstrapping in diesel sprays. Combustion and Flame. 2017;182:20-7.
[20] Luque J, Crosley DR. LIFBASE: Database and spectral simulation (version 1.5). SRI International Report MP 99-009 (1999). 1999.
[21] Schulz C, Sick V. Tracer-LIF diagnostics: quantitative measurement of fuel concentration, temperature and fuel/air ratio in practical combustion systems. Progress in Energy and Combustion Science. 2005;31:75-121.
[22] Westlye FR, Penney K, Ivarsson A, Pickett LM, Manin J, Skeen SA. Diffuse back-illumination setup for high temporally resolved extinction imaging. Applied Optics. 2017;56:5028-38.
[23] Schlatter S, Schneider B, Wright Y, Boulouchos K. Experimental Study of Ignition and Combustion Characteristics of a Diesel Pilot Spray in a Lean Premixed Methane/Air Charge using a Rapid Compression Expansion Machine. Warrendale, PA: SAE International; 2012.
[24] Schlatter S, Schneider B, Wright YM, Boulouchos K. Comparative Study of Ignition Systems for Lean Burn Gas Engines in an Optically Accessible Rapid Compression Expansion Machine. Warrendale, PA: SAE International; 2013.
[25] Schlatter S, Schneider B, Wright YM, Boulouchos K. N-heptane micro pilot assisted methane combustion in a Rapid Compression Expansion Machine. Fuel. 2016;179:339-52.
[26] Lee D, Hochgreb S. Rapid Compression Machines: Heat Transfer and Suppression of Corner Vortex. Combustion and Flame. 1998;114:531-45.
[27] Mederer T, Wensing M, Leipertz A. GE2-2 Laser-Induced Fluorescence to Visualize Gas Mixture Formation in an Optically Accessible Hydrogen Engine(GE: Gas Engine,General Session Papers). The Proceedings of the

International symposium on diagnostics and modeling of combustion in internal combustion engines. 2012;2012.8:374-9.
[28] Bruneaux G. Mixing process in high pressure diesel jets by normalized laser induced exciplex fluorescence part I: free jet. SAE Technical Paper; 2005.
[29] Salaun E, Apeloig J, Grisch F, Yvonnet C-E, Nicolas B, Dionnet F. Optical Investigation of Ignition Timing and Equivalence Ratio in Dual-Fuel CNG/Diesel Combustion. 2016.
[30] Musculus MP, Kattke K. Entrainment waves in diesel jets. SAE International Journal of Engines. 2009;2:1170–93.
[31] Goodwin DGM, Harry K; Speth, Raymond L. Cantera: An Object-oriented Software Toolkit for Chemical Kinetics, Thermodynamics, and Transport Processes. Version 2.3.0.
[32] Westbrook CK, Pitz WJ, Herbinet O, Curran HJ, Silke EJ. A comprehensive detailed chemical kinetic reaction mechanism for combustion of n-alkane hydrocarbons from n-octane to n-hexadecane. Combustion and Flame. 2009;156:181-99.
[33] Narayanaswamy K, Pepiot P, Pitsch H. A chemical mechanism for low to high temperature oxidation of n-dodecane as a component of transportation fuel surrogates. Combustion and Flame. 2014;161:866-84.
[34] Luo Z, Som S, Sarathy SM, Plomer M, Pitz WJ, Longman DE, et al. Development and validation of an n-dodecane skeletal mechanism for spray combustion applications. Combustion Theory and Modelling. 2014;18:187-203.
[35] Dahms RN, Paczko GnA, Skeen SA, Pickett LM. Understanding the ignition mechanism of high-pressure spray flames. Proceedings of the Combustion Institute. 2017;36:2615-23.
[36] Manin J, Pickett LM, Skeen SA. Two-Color Diffused Back-Illumination Imaging as a Diagnostic for Time-Resolved Soot Measurements in Reacting Sprays. SAE International Journal of Engines. 2013;6:1908-21.
[37] Pickett LM. Engine combustion network2013.
[38] Najafabadi MI, Egelmeers L, Somers B, Deen N, Johansson B, Dam N. The influence of charge stratification on the spectral signature of partially premixed combustion in a light-duty optical engine. Applied Physics B. 2017;123.
[39] Tautschnig G, Hampel B, Hirsch C, Sattelmayer T. Experimental Investigation of OH* and CH* Chemiluminescence Under Varying Operating Conditions. American Society of Mechanical Engineers; 2013. p. V01BT4A062–V01BT04A.
[40] Desantes JM, García-Oliver JM, Vera-Tudela W, López-Pintor D, Schneider B, Boulouchos K. Study of the auto-ignition phenomenon of PRFs under HCCI conditions in a RCEM by means of spectroscopy. Applied Energy. 2016;179:389-400.
[41] Mitakos D. Experimental Investigations for Phenomenological Modelling of Two-Stage Auto-Ignition under HCCI Conditions: Eidgenösische technische Hochschule Zürich; 2014.
[42] Iijima A, Shoji H. A Study of HCCI Combustion Characteristics Using Spectroscopic Techniques. SAE International; 2007.